

A Thesis Submitted for the Degree of PhD at the University of Warwick

Permanent WRAP URL:

<http://wrap.warwick.ac.uk/175690>

Copyright and reuse:

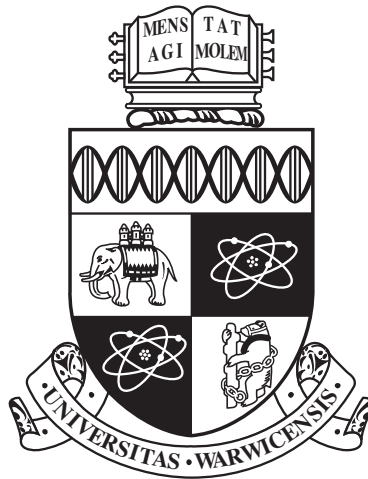
This thesis is made available online and is protected by original copyright.

Please scroll down to view the document itself.

Please refer to the repository record for this item for information to help you to cite it.

Our policy information is available from the repository home page.

For more information, please contact the WRAP Team at: wrap@warwick.ac.uk



**Evaluation of Laser Shock Peen Additive
Manufacture Inconel 718 for High Temperature
Applications**

by

Elson Yong Ching Kiat

Thesis

Submitted to the University of Warwick

for the degree of

Engineering Doctorate

Warwick Manufacturing Group

January 2022

THE UNIVERSITY OF
WARWICK

Contents

| | |
|---|------------|
| List of Tables | v |
| List of Figures | vi |
| Acknowledgments | ix |
| Declarations | xi |
| Abstract | xii |
| Abbreviations | xiv |
| Chapter 1 Introduction | 1 |
| 1.1 What is additive manufacturing | 1 |
| 1.2 Research aims & questions | 3 |
| 1.3 Structure of thesis | 4 |
| Chapter 2 Literature review | 5 |
| 2.1 AM process | 5 |
| 2.1.1 Benefits | 5 |
| 2.1.2 Industrial value | 7 |
| 2.1.3 Common alloys processed by PBF | 10 |
| 2.2 Microstructure of AM IN718 | 11 |
| 2.2.1 Grain structure | 11 |
| 2.2.2 Effects of δ phases | 12 |
| 2.2.3 Mechanical properties of AM IN718 alloy | 13 |
| 2.3 Laser Shock Peening process | 14 |
| 2.3.1 Introduction | 14 |
| 2.3.2 Effects on material properties | 16 |
| 2.3.3 Performance of LSP wrought IN718 | 22 |

| | | |
|--|---|-----------|
| 2.3.4 | Suitability of LSP on AM IN718 | 23 |
| 2.4 | Summary and gaps in literature | 24 |
| Chapter 3 Experimental methods | | 25 |
| 3.1 | Powder Bed Fusion | 25 |
| 3.1.1 | Material specifications | 25 |
| 3.1.2 | Processing parameters | 26 |
| 3.1.3 | Geometry | 26 |
| 3.1.4 | Heat treatment | 27 |
| 3.1.5 | Milling | 27 |
| 3.1.6 | Wrought | 27 |
| 3.2 | Laser Shock Peening | 27 |
| 3.2.1 | Processing parameters | 27 |
| 3.3 | Surface roughness measurements | 28 |
| 3.4 | Stress measurement | 29 |
| 3.4.1 | Synchrotron X-ray Diffraction (SXRD) processing parameters & setup | 29 |
| 3.4.2 | Data processing | 29 |
| 3.4.3 | Strain free reference | 32 |
| 3.4.4 | Propagation of errors | 32 |
| 3.5 | Phase identification using Powder Cell | 32 |
| 3.6 | Cold work measurements | 33 |
| 3.6.1 | Preparation | 33 |
| 3.6.2 | Microhardness | 33 |
| 3.6.3 | Full width half maximum | 35 |
| 3.7 | Microstructure characterisation | 35 |
| 3.8 | Mechanical test | 36 |
| 3.8.1 | Uniaxial tensile test | 36 |
| 3.8.2 | Thermal and mechanical loading | 36 |
| 3.8.3 | Three point flexural fatigue | 38 |
| 3.8.4 | Fractography analysis | 39 |
| Chapter 4 Results & discussions | | 40 |
| 4.1 | Surface roughness | 40 |
| 4.2 | Phase identifications | 41 |
| 4.2.1 | Summary | 42 |
| 4.3 | Effect of LSP on grain size | 43 |
| 4.4 | Cold work | 45 |

| | | |
|---|---|------------|
| 4.4.1 | Vicker's hardness result | 45 |
| 4.4.2 | FWHM data from SXRD | 46 |
| 4.4.3 | Mapping and measuring plastic deformation using EBSD | 47 |
| 4.4.4 | Analysis and summary | 50 |
| 4.5 | Residual stress measurements due to LSP | 50 |
| 4.6 | Residual stress relaxation | 51 |
| 4.6.1 | Residual stress with thermal load | 51 |
| 4.6.2 | Residual stress with mechanical load | 52 |
| 4.6.3 | Stress relaxation due to thermomechanical load | 54 |
| 4.6.4 | Summary | 55 |
| 4.7 | Uniaxial tensile stress | 55 |
| 4.8 | Bending fatigue | 57 |
| 4.8.1 | Room temperature bending fatigue | 57 |
| 4.8.2 | 550°C bending fatigue | 61 |
| 4.8.3 | Summary | 65 |
| Chapter 5 Conclusion & future work | | 67 |
| 5.1 | Summary and innovative contributions | 67 |
| 5.1.1 | Development of laser shock peening process for additive manufactured Inconel 718 material | 67 |
| 5.1.2 | Effect of laser shock peening on the mechanical properties on additive manufactured Inconel 718 | 68 |
| 5.1.3 | Residual stress relaxation of AM.LSP in various loading conditions | 69 |
| 5.1.4 | Three point flexural bending performance in both room temperature and heated environment | 70 |
| 5.2 | Limitations of the research and recommendations for future work | 71 |
| 5.2.1 | Material optimisation | 72 |
| 5.2.2 | Polishing specimen surface to a lower surface roughness value | 72 |
| 5.2.3 | Temperature data collection during the LSP process | 72 |
| 5.2.4 | Damage analysis on fractured specimens | 72 |
| Appendix A EOS IN718 material specifications | | 102 |
| Appendix B Powder composition | | 110 |
| Appendix C Python codes for lmfit | | 113 |
| Appendix D Publication 1 | | 116 |

| | |
|---------------------------------|------------|
| Appendix E Publication 2 | 126 |
| Appendix F Publication 3 | 149 |

List of Tables

| | | |
|-----|--|----|
| 2.1 | Advantages of AM over traditional manufacturing | 9 |
| 2.2 | Metal alloys commonly used for PBF process | 10 |
| 2.3 | Comparison of cold work provided by shot peening and LSP | 18 |
| 3.1 | AM IN718 initial powder chemical composition w.t % | 25 |
| 3.2 | Experiment setup of thermomechanical test | 37 |
| 4.1 | Surface roughness Ra values of pristine AM and AM_LSP in both directions | 40 |
| 4.2 | Grain size estimation of pristine AM and AM_LSP specimen using the mean line intercept method | 43 |

List of Figures

| | | |
|-----|--|----|
| 1.1 | Material design chart that showcase the process-structure-properties-performance relationship for AM metal alloy retrieved from [8] | 2 |
| 1.2 | Block diagram showcasing the research input and outputs | 3 |
| 2.1 | AM industry activity map of selected aerospace companies, retrieved from [36] | 8 |
| 2.2 | An electron microscopic image showing the columnar grains of AM IN718, retrieved from [11] | 11 |
| 2.3 | Mechanism of shock wave creation in the LSP process, retrieved from [135] | 15 |
| 2.4 | Schematic illustration of grain refined through multiple LSP impacts, retrieved from [142] | 16 |
| 2.5 | Optical microscope on the surface of AZ31B Mg alloy at 0.8 mm below the surface (a) before LSP; (b) with one impact; (c) with two impacts; and (d) with four impacts, retrieved from [134] | 17 |
| 2.6 | Near-surface microstructure of LSP AISI 304 after thermal exposure between 25 to 900°C, retrieved from [143] | 19 |
| 2.7 | Residual stress distribution and cold work developed by in IN718 coupons using various surface enhancement process, retrieved from [148] | 20 |
| 2.8 | Effect of thermal relaxation of IN718 at 670°C that has been subjected to both shot peening and laser shock peening, retrieved from [148] | 21 |
| 2.9 | Residual stress curve measured for 316L stainless steel for as-built (AB), LSP after AM (2D LSP) and ex-situ LSP on AM (3D LSP), retrieved from [154] | 23 |
| 3.1 | Schematics of a dog-boned geometry specimen showing the build and powder layering direction | 26 |

| | | |
|------|---|----|
| 3.2 | (a) Experimental setup of the laser shock peening process using a robotic arm and (b) the four step peening strategy | 28 |
| 3.3 | Surface roughness measurements segregated into three regions | 28 |
| 3.4 | (a) Samples stacked together with the beam line scanning it vertically and (b) photo of the experiment setup in DIAMOND I12 facility | 29 |
| 3.5 | Raw diffraction images with the selected Azimuthal slice which correspond to the in-plane stress | 30 |
| 3.6 | Example of a fitted Gaussian peak profile with a flat background using the LMfit library | 31 |
| 3.7 | Photograph of (a) Innovatest Falson 510 indenter and (b) schematics of how the hardness measurement were collected on a cross-sectional LSP AM IN718 specimen | 34 |
| 3.8 | Photograph of the experimental setup of the thermomechanical test of 25 kN load cell Instron dynamic fatigue machine with oven attached to it | 37 |
| 3.9 | Photograph of the experimental setup of the three point flexure test | 38 |
| 3.10 | Schematics of the three point flexure test with the specimen | 39 |
| 4.1 | Phase identification using SXRD data | 41 |
| 4.2 | Elemental analysis of AM_LSP using EDS-SEM | 42 |
| 4.3 | SEM image of (a) pristine AM and (b) AM_LSP IN718 | 43 |
| 4.4 | Cumulative area-weighted fraction of AM_LSP equivalent circle diameter | 44 |
| 4.5 | 2D heatmap of hardness value of a cross-sectional area of AM_LSP specimen | 45 |
| 4.6 | FWHM data of both pristine AM and AM_LSP specimen across the entire thickness | 46 |
| 4.7 | KAM of the cross sectional surface of (a) pristine AM and (b) AM_LSP | 49 |
| 4.8 | Through thickness stress measurement of AM and AM_LSP specimens | 51 |
| 4.9 | Through thickness residual stress measurement of AM_LSP specimen in a 550°C setting for 1 hour and 15 hours respectively | 52 |
| 4.10 | Through thickness residual stress measurement of AM_LSP specimen under cyclic loading in a room temperature setting | 53 |
| 4.11 | Through thickness residual stress measurements under cyclic loading in a 550°C setting | 54 |
| 4.12 | Comparison of tensile strength of pristine AM, AM_LSP, Wrought and LSP Wrought specimens | 56 |

| | | |
|------|---|----|
| 4.13 | S-N curve of bending flexure test of pristine AM and AM.LSP specimens under room temperature setting | 57 |
| 4.14 | Picture of (a) fractured pristine AM specimen and (b) closeup photograph of fractured surface | 59 |
| 4.15 | SEM image of pristine AM (a) crack initiation point, (b) fatigue propagation area, (c) high magnification showing striation marks and (d) high magnification showing dimple feature | 59 |
| 4.16 | Picture of (a) fractured AM.LSP specimen and (b) closeup photograph of fractured surface | 60 |
| 4.17 | SEM image of AM.LSP (a) crack initiation point, (b) fatigue propagation area, (c) high magnification showing striation marks and (d) high magnification showing dimple feature | 60 |
| 4.18 | S-N curve of bending flexure test under 550°C setting | 61 |
| 4.19 | Picture of (a) fractured pristine AM specimen and (b) closeup photograph of fractured surface in 550°C setting | 62 |
| 4.20 | SEM image of pristine AM (a) crack initiation point, (b) fatigue propagation area, (c) high magnification showing striation marks and (d) high magnification showing dimple feature | 63 |
| 4.21 | Picture of (a) fractured AM.LSP specimen and (b) closeup photograph of fractured surface in 550°C setting | 63 |
| 4.22 | SEM image of AM.LSP (a) crack initiation point, (b) fatigue propagation area, (c) high magnification showing striation marks and (d) high magnification showing dimple feature | 64 |
| 4.23 | S-N curve of bending flexure test under both room temperature environment and 550°C setting | 65 |

Acknowledgments

The research work for this thesis was carried out at the research environment Warwick Manufacturing Group (WMG) of University of Warwick, United Kingdom. The project has been funded by Agency of Science, Technology and Research (A*STAR) through the A*STAR-Warwick Partnership scholarship.

I would like to thank everyone who has made success in this project possible. As with anything of this scale, there are countless people involved at various points, all of whom have had an effect on the process and outcome of the work. However, I feel that it is necessary to thank the following people specifically for their significant contributions and support:

It has been a privilege to have Dr Gregory Gibbons, Dr Geoff West and Dr Wong Chow Cher as my supervisors for the doctoral studies. Thank you for all your guidance and support so far. You trusted me, provided me with the scientific freedom I hoped for and offered an excellent environment for me to grow as a professional. I look forward to continuing working with you in my future endeavours.

I received a ton of technical advice and training from Dr Ampara Aramcharoen, Dr Kum Chun Wai, Dr Dennise Tanoko Ardi, Dr Henry Cheng, Dr Niroj Maharjan, Dr Wei Yuefan, Dr Sho Itoh, Kunal Ahluwalia, Aldrich Chua, Augustine Teo, Muhammad Azrul, Luei Kah Han, Lim Guowei, Cheng Wei Shin, Thivyaa Ramesh, Roger Chan, Chan Shi Ying and Fong Sai Leong. Thank you for helping me in this journey despite there being no personal incentives. I would also like to thank Paul Hadlum, Mick Green, Luke Millage and Zac Parkinson for their selfless commitment in the WMG workshops towards helping researchers such as myself.

The industrial collaboration with DIAMOND made this project, in this ex-

citing field of metal additive manufacturing, even more fascinating. I sincerely thank Dr Thomas Connolly for the material support and technical services, critical feedback, inspiring discussions and sharing valuable knowledge throughout.

To all my friends, here in U.K, back in Singapore and spread across the rest of the world, thank you for all the love, care and advice all along. Without you people, the journey would not have been the same!

Perhaps the greatest thanks goes to my family, without the support, encouragement and love from them, I would have struggled to get through the difficult periods of the last four years.

Finally my beautiful wife, Alvina Tan, thank you for the love, support and encouragement you have given me. Without you I would never have the strength to finish the doctorate studies, and therefore I would have never have found myself in the position that I am in now. From long before this project began, throughout its duration and every day after, you have been my constant, my rock, and my best friend. I could not have done this without you.

Declarations

This thesis is submitted in partial fulfilment of the requirements for the degree of Engineering Doctorate. The presented research was carried out from October 2018 to December 2021. The research described is my own and not the product of collaboration. The contents of this thesis have been used to produce the following journal publications:

- Yong, C.K., G.D. West, G.J. Gibbons, and C.C. Wong. Influence of Laser Shock Peening (LSP) on the Material Properties of Additive Manufactured IN718. *Advanced Surface Enhancement*, 2020. Singapore: Springer Singapore. Accepted in publication
- Yong, C.K., G.D. West, G.J. Gibbons, and C.C. Wong. A Critical Review of the Material Characteristics of Additive Manufactured IN718 for High-Temperature Application. *Metals*, 2020. 10(12). Accepted in publication
- Yong, C.K., Darren J Hughes, Elspeth M Keating, Thomas Conolly, G.D. West, G.J. Gibbons and C.C. Wong. Evaluation of Mechanical Properties of Laser Shock Peened Additive Manufactured Inconel 718 using Synchrotron X-ray Diffraction. In manuscript

Abstract

Nickel superalloys find several applications in the aerospace and automotive industry, notably as safety-critical components such as turbine blades and turbine discs. A new kind of manufacturing technique termed Additive Manufacturing (AM) has gained significant interest due to its capabilities of fabricating components that could minimise material wastage and/or components that possess complex geometries, possibly unmanufacturable using conventional technologies. Among the various AM processes for metallic components, powder bed fusion (PBF) has shown great potential for manufacturing Inconel 718 (IN718) components. The future of PBF is undoubtedly promising but there are still some gaps to fill before AM components materials are ready for widespread industrial application.

Laser shock peening (LSP) is an effective surface enhancement process that is used in an aeroengine manufacturing line to strengthen components resistance to surface-related failures. Pioneering work in the late 1990s employed synchrotron radiation for residual stress assessment to enable the adoption of LSP in aeroengine components. The technology is now used in engines worth tens of billions of pounds. Back to the present time, there is a push to adopt AM technology as a step-change in production and integrating LSP into AM IN718 seems to be an obvious way forward.

The work presented in this thesis aims to better understand the effects that LSP has brought to AM IN718, which have not been systematically investigated. Microstructures of AM IN718 have been characterised with scanning electron microscopy (SEM) using the electron backscattered diffraction (EBSD) technique and transmission electron microscopy (TEM) to correlate microstructural changes with

the process conditions. Mechanical properties (e.g. microhardness and tensile properties) have also been measured and rationalised with regards to the LSP treatments. Specimens were put under various thermal and mechanical loading to simulate the aeroengine setting. Synchrotron X-ray diffraction (SXRD) was utilised to assess the residual stress relaxation of these specimens and the phases present in AM IN718. Full width half maximum (FWHM) data from the SXRD experiment were used to characterise the cold work present in the specimens that were LSP-ed. Three point flexure test was selected as the appropriate test scenario to evaluate the mechanical performance of the LSP AM IN718 at a structural level.

Comparison of the observed mechanical performance indicates that there is potential for LSP to be integrated with the AM process of IN718. Within a 550°C environment, the LSP-ed specimens hold up to 50% of its initial residual stress after going through about a million flexural cycles. Surface roughness and cold work were found to be key factors controlling the fatigue performance. Microstructure analysis suggests that LSP bring minimal cold work to AM IN718 which is the contributing factor to its excellent containment of residual stress. Results from this licentiate thesis provide the basis for the further industrial research on the cyclic mechanical properties of AM IN718.

Abbreviations

AE Acoustic emission

AM Additive manufacturing

AMS Aerospace material specifications

A Ageing

ASTM American society for testing and materials

BCT Body-centered tetragonal

BS British standard

DOE Design of experiment

DA Direct ageing

DED Direct energy deposition

EDM Electrical discharge machine

EBSD Electron backscatter diffraction

EDS Energy dispersive X-ray spectroscopy

FCC Face-centered-cubic

FWHM Full width half maximum

GE General electric

GEAE General electric aircraft engines

HIP Hot isostatic pressing

IN718 Inconel 718

LSP Laser shock peening

LCF Low cycle fatigue

MT Mechanical twins

CT Micro-computed tomography

PBF Powder bed fusion

RTP Room temperature

SA Solution annealed

SHT Solution heat treated

SXRD Synchrotron X-ray diffraction

TCP Topologically close pack

TEM Transmission electron microscope

UTS Ultimate tensile strength

VHCF Very-high-cycle fatigue

W Wrought IN718

YS Yield strength

θ Bragg angle

b Breadth of the specimen

El Elongation

- γ'' Gamma double prime
- γ' Gamma prime
- h Height of the specimen
- d Lattice spacing
- d_{hkl} Lattice spacing of a relevant hkl plane
- L_i Length of the cantilever
- F Load
- q Momentum transfer in reciprocal-space
- ν Poisson ratio
- q_0 Strain free reciprocal-space
- q_{0hkl} Strain free reciprocal-space of a relevant hkl plane
- σ Stress
- σ_x Stress state in the X direction
- R Stress to number of cycles graph
- λ X-ray wavelength
- E Young's elastic modulus of the material

Chapter 1

Introduction

1.1 What is additive manufacturing

Additive Manufacturing (AM), also known as 3D printing, is a manufacturing process that utilises 3D model data to deposit successive layers of material, one layer on top of another to form the component. The first AM technology was stereolithography, utilising a ultraviolet laser to selectively solidify a liquid resin, and has evolved over the years into many formats, processing a wide range of materials. Currently, it is readily accepted as a manufacturing option in the aerospace industry for many products [1, 2, 3], and particularly for turbine components [4]. The technique has garnered much attention in the industry as it can build products with more geometric flexibility in a much shorter time than conventional manufacturing processes.

Alloys that operate at high temperatures are critical for these industries as fuel conversion efficiency is closely related to the operating temperature. The effective temperature rise in the aeroengine provides the energy required to propel the vehicle. Essentially, the higher the temperature, the greater the exhaust velocity and the limiting factor is usually the turbine material melting point [5]. Generally, these alloys are nickel, iron or cobalt-based. The high strength of these alloys can pose a challenge, as machining them can be very difficult and expensive due to their natural tendency for work hardening. The shift to AM technology has allowed manufacturers to produce complex geometries such as lattice structures [6, 7], whereas traditional manufacturing such as casting or forging is more time-consuming or incapable of achieving these geometries. Researchers [8, 9] have made great efforts to understand the process-structure-property-performance relationships for AM materials. Figure 1.1 illustrates a general metal alloy design chart with the

intent to produce the most optimised mechanical properties suited for its intended application.

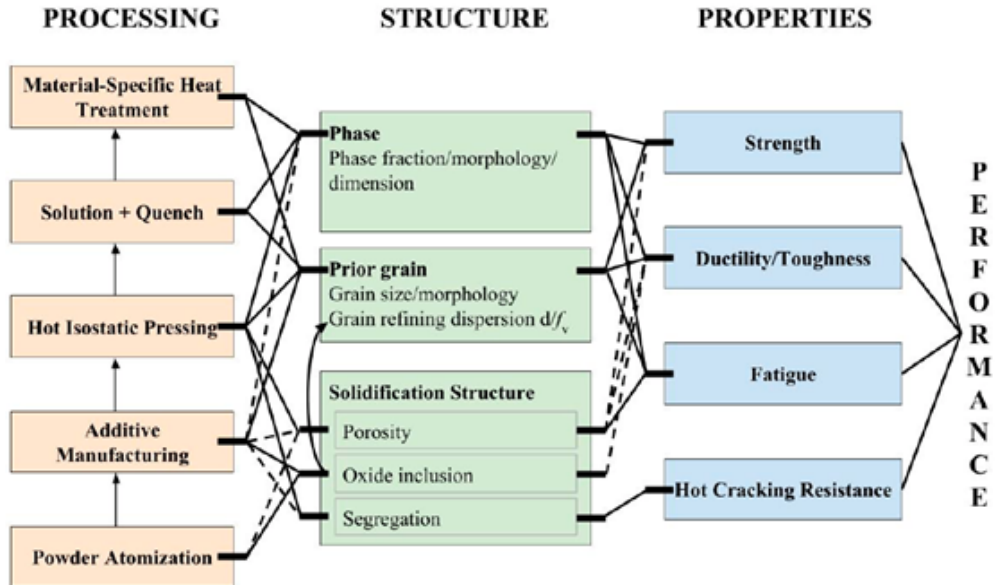


Figure 1.1: Material design chart that showcase the process-structure-properties-performance relationship for AM metal alloy retrieved from [8]

The outbreak of COVID19 has prompted companies to look towards a “just in case” production framework rather than “just in time” [10], specifically benefiting from the advanced production capability of AM processes. However, the AM printing process has been plagued by many defects such as micro-porosity and detrimental tensile stress [11, 12, 13] and the scientific community have been looking at many ways to optimise the process-structure-property-performance. Substandard AM processing parameters can caused the lack of fusion and keyhole pores to form. These pores create local stress concentration which indirectly trigger crack to initiate [14]. High temperature gradient cause by the fast solidification during the AM processes cause tensile residual stresses in AM parts to form. These stresses are detrimental to fatigue behavior and can result in distortion of the manufactured parts [15]. Nonetheless, the future of AM is promising, and this thesis covers the current research gap and introduces a novel post-processing technique to further its applications in high temperature environments.

1.2 Research aims & questions

This chapter introduces the drivers for utilising AM in the aerospace industry and the role that AM material can play realising high-performance critical aeroengine parts. The current research on AM aims to overcome some of the inherent defects present in the technique itself. Inconel 718 (IN718) is a widely used nickel-based superalloy as it can withstand loading at an operating temperature close to its melting point [16]. Among all the viable metal alloys that can be manufactured through the AM process, IN718 has excellent fatigue resistance in high temperature environment. It is heavily utilised by aeroengine manufacturers [17] and therefore, it is worthwhile to explore the options of complementing AM into current manufacturing process of IN718.

Researchers worldwide have tried to deal with the defects present through AM processing, and the results have been lacklustre [18, 19, 20]. Surface enhancement processes such as laser shock peening (LSP) have shown to be effective in increasing the material fatigue limit on wrought material [21, 22]. There are also interest in the aerospace industry to incorporate LSP on AM material [23]. This thesis presents a body of research targeting the development of LSP technique on AM IN718 material and the beneficial effects it can bring to increase its useability in high temperature environments.

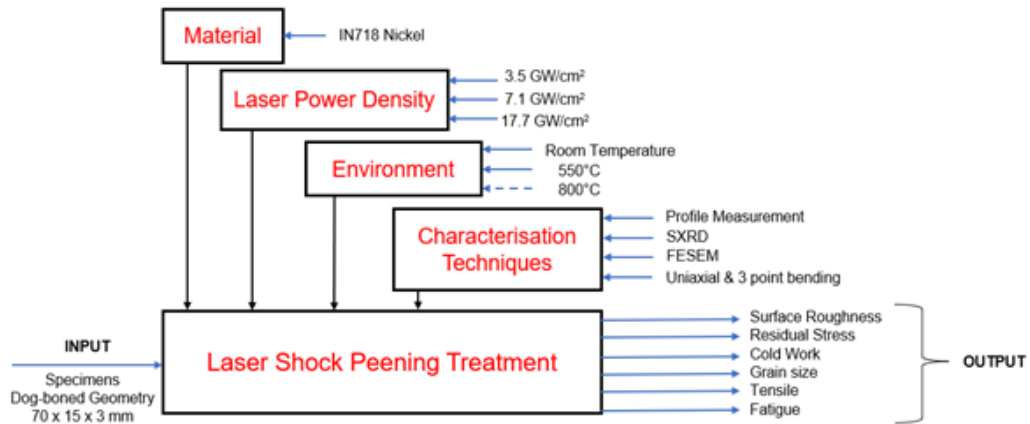


Figure 1.2: Block diagram showcasing the research input and outputs

The general aims of the present research are to investigate the effect of LSP on the mechanical and microstructure properties of AM IN718. This will form a basis for understanding its performance in both room temperature and high temperature environment. More specifically, the main focus is placed on correlating the

mechanical properties (e.g. cold work and residual stress) with the fatigue life. In summary, the thesis addresses the following research questions:

1. How does AM IN718 perform in the room temperature environment?
 - What are the mechanical and microstructure properties?
 - How does it compare to wrought IN718?
2. How receptive is AM IN718 towards LSP? environment
 - What does LSP provide to the material?
 - Does it bring beneficial or harmful effects to the material?
 - If it's beneficial, does it increase the useability in a high temperature environment?

The research is pictorially summarised in Figure 1.2.

1.3 Structure of thesis

Chapter 1 provides a brief introduction to AM and established the context of multiple topics that justify the work undertaken in this thesis.

Chapter 2 presents a thorough review of the literature corresponding to the AM process, material characteristics and the laser shock peening process.

Chapter 3 describes the manufacturing process and methodologies used in this research. It includes the AM process, laser shock peening process, and various mechanical tests used to characterise the processed samples. The chapter also discusses the techniques used to analyse the samples' residual stress state and the setup for both the uniaxial tensile test and three-point flexure fatigue bending test.

Chapter 4 describes the material and mechanical characteristics of both the pristine (i.e. as-built) and laser shock peened specimens. Surface roughness, phase identification and evaluation of cold work are presented in the chapter to highlight the effects laser shock peening has on the specimens. This is followed by a thorough residual stress evaluation of the specimens and the stress relaxation that they go through at various temperatures. The chapter concludes with a comparison of the mechanical performance of the pristine and laser shock peened AM specimens and explore the feasibility of the technique.

Chapter 5 summarises the results in this thesis and provides recommendations for future research work in this area. It also discusses the wider implications of the work and where laser shock peened AM samples can be applied effectively.

Chapter 2

Literature review

This chapter provides a review of the previously conducted research in the fields relevant to this thesis. The chapter begins with a general overview of the AM process and its benefits to the aerospace industry. Following this, the material properties of AM IN718 are discussed and the mechanical properties of the material are provided. Thereafter, a brief introduction of the LSP process is discussed and the effect it brings on metal alloy is discussed. The chapter close by assessing LSP suitability on AM IN718 alloy.

2.1 AM process

2.1.1 Benefits

Reviews on the AM build process have been covered by various authors [24, 25, 26, 27, 28, 29] but the mechanical properties and performance of AM materials have not been thoroughly review. This section will start off by giving an introduction of the standards that is established by the ASTM F2792-12a followed by the commercial value AM material brings into the aerospace industry.

Out of the seven main AM processes, powder bed fusion (PBF) and direct energy deposition (DED) are generally used to produce high quality metal parts. Lewandowski et al. [25] categorized these two mainstream processes into their respective energy source for fusion and the companies specialising in them.

PBF has a unique position because of its potential to manufacture metal components in a range of alloys using fine metal powders (typically 15 - 45 μm) at high resolution of up to 100 μm [30], which has broadened the application to various industries. The process consists of depositing thin layers of fine powder on a platform which is then fused together with a laser or electron beam. Many metallic

materials such as stainless and tool steels, aluminium alloys, titanium and its alloys, and nickel-based alloys can be manufactured by this process. Spierings et al. [31] studied the relationship between the particle size distribution (PSD) and the powder layer thickness. The authors concluded that effective powder layer thickness should be larger than the 90th percentile of the particle size [32]. It was also concluded in Nguyen et al. study that the ideal PSD for PBF is typically in the range from 15 μm to 63 μm [33]. This is largely due to working forces such as the presence of gravity and inter-particle forces. Although smaller size particles that result in highly packed powder beds are desirable as it minimises void volume fraction, it can pose other challenges as well. When the particle size is smaller than a threshold value, van der Waals and electrostatic forces becomes dominant, causing formation of aggregates that result in poor part quality [34]. In this research, PBF is solely used to fabricate the specimens using the recommended PSD parameters because of the various advantage it brings to the manufacturing process.

2.1.2 Industrial value

In the past 10 years, many companies have embraced AM technologies and are beginning to enjoy the real business benefits. In a report by Statista, the global 3D printer market size reached US\$7.3 billion in 2017 and the aerospace and defence sectors account for 17.8% of the market distribution in 2016 [35]. The global AM market is expected to see double digit growth into 2022 with market analysis projecting a growth of up to 35% per annum [36]. Recent developments such as cheaper metal powder [37] and the influx of new vendors [38] have significantly reduced the cost of the printers and AM has worked its way into the biomedical [39] and build construction [40] industry. The growing consensus of adopting AM into its production floor is attributed to several advantages over traditional manufacturing, as shown in Table 2.1

A wide variety of materials can be utilised in PBF, but metals are generally popular due to their extensive use in industrial and consumer appliances, including aerospace components. Figure 2.1 illustrates the activity map of selected aerospace companies, with many players focusing their research and development work on AM technology. General Electric (GE) leads the industry in terms of both the volume and machine capacity and have printed more than 100,000 parts by 2020 [41]. Rolls Royce, MTU Aero Engines, Pratt & Whitney and GKN Aerospace have established their own competencies centres to upskill their AM capabilities [36]. GE Aviation has been particularly successful in implementing AM technology into its product. In 2015, GE announced that the next LEAP engine will have nearly twenty AM fuel nozzles, simplifying parts by combining multiple components. Traditionally, the aerospace industry used advanced and costly materials like titanium and nickel alloys to manufacture some of its safety critical aeroengine parts, which are difficult to manufacture due to its high strength, and unavoidably creates a large amount of waste when fabricating them. For example, Wilson et al. [42] has shown that through the use of AM technology, his team was able to achieve a 45% carbon footprint improvement and a 36% savings in total energy over replacing it with an entirely new blade. In 2019, Rolls Royce produced its first AM low-pressure turbine for the Trent XWB-84 which is expected to result in a component weight reduction of up to 40% as well as generate significant cost savings for the company [4].

In a separate report made by Deloitte, it highlighted that conventional way of machining the raw material into components can entail a scrap rate as high as 80–90 percent of the original billet whereas AM technology utilises around 10-20% of the raw material instead [43]. Moreover, AM has the potential to lower overall cost as it is able to manufacture spare parts on demand, reducing maintenance time and

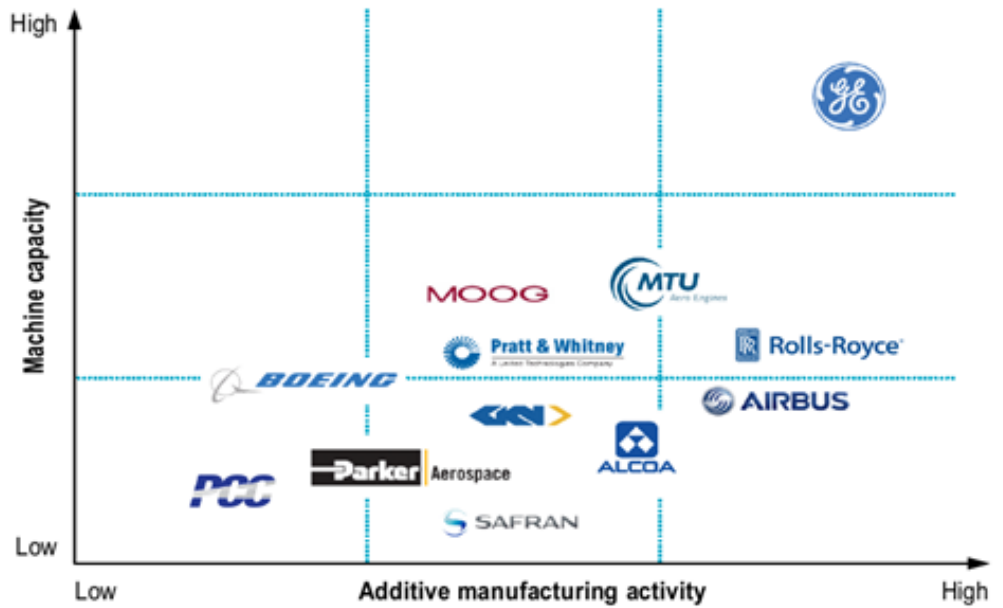


Figure 2.1: AM industry activity map of selected aerospace companies, retrieved from [36]

the need for inventory management [44]. Boeing and Airbus typically sourced their 4 million spare parts globally, and airlines usually maintain an inventory of spares to avoid their planes from becoming grounded. AM technology is an enabler for these companies to embark on a supply chain transformation, making on-demand manufacturing possible.

Table 2.1: Advantages of AM over traditional manufacturing

| Areas of application | Advantages |
|--|--|
| Rapid Prototyping | Reduce time to market by accelerating prototyping, reduce the cost involved in product development and making companies more efficient and competitive at innovation |
| Production of Spare Parts | Reduce repair times, labor cost and avoid costly warehousing |
| Small Volume Manufacturing | Small batches can be produced cost-efficiently and eliminate the investment in tooling |
| Customized Unique Items | Low cost, quick production of exact and customized replacement parts on site and reduce cost for redesign |
| Complex Work Pieces | Produce complex work pieces at reduced cost |
| Machine Tool Manufacturing | Reduce labour cost, avoid costly warehousing and enables mass customization at low cost |
| Rapid Manufacturing | Directly manufacturing finished components and relatively inexpensive production of small number of parts |
| Component Manufacturing | Enable customization at low cost, improve quality, shorten supply chain, reduce the cost involved in development and help eliminate excess parts |
| On-site and On-demand Manufacturing of Replacement Parts | Eliminate storage and transportation cost, reduce downtime, shorten supply chain and allow product lifecycle leverage |
| 10. Rapid Repair | Reduction in repair time and opportunity to modify repaired components to the latest design |

2.1.3 Common alloys processed by PBF

Table 2.2: Metal alloys commonly used for PBF process

| Alloy | Examples | Reference |
|----------------|--|---|
| Titanium | Ti-6Al-4V, Ti-6.5Al-1Mo-1V-2Zr, Ti-6.5Al-3.5Mo-1.5Zr-0.3Si, Ti-5Al-4Mo-2Zr-2Sn-4Cr, Ti-3Al-10V-2Fe, Ti6242 | [18, 45, 46, 47, 48, 49, 50, 51, 52, 53, 54, 55, 56, 57] |
| Intermetallics | NiTi | [58, 59, 60, 61] |
| Steel | 316L, 17-4PH, AISI 420 | [62, 63, 64, 65, 66, 67] |
| Nickel | ABD900, IN718, IN625, IN939, C263, Hastelloy X, Haynes 282, K418 | [68, 69, 70, 71, 72, 73, 74, 75, 76, 77, 78, 79, 80, 81, 82, 83, 84, 85, 86, 87, 88, 89, 90, 12, 91, 92, 93, 94, 95, 96, 97, 98, 99, 100, 101, 102, 103, 104] |
| Aluminium | Al-Si10-Mg, Al-Si12-Mg, 6061 | [51, 105, 106] |

IN718 is the most commonly used nickel-based alloy in the aerospace industry due to its superior mechanical properties at elevated temperatures and has been widely used in the turbine section of the aeroengine [107, 16, 108]. Nickel alloys such as IN718 is suitable for AM as it has a relative high density due to their good weldability [109] and the ability to operate up to around 650°C for applications under load. It has a high phase stability of face-centered-cubic (FCC) nickel matrix and the capability to be strengthened by other elements such as chromium and/or aluminium [17]. The microstructure of IN718 is referred to by γ (gamma), a continuous matrix phase where cobalt and chromium prefers to reside; γ' (gamma prime), an intermetallic phase based on Ni₃(Al,Ti) with a L12 crystal structure; γ'' (gamma double prime), a metastable phase that is the primary strengthening precipitate with a body-centered tetragonal (BCT) ordered compound with a D022 crystal structure; δ (delta), an equilibrium phase with an orthorhombic D0a structure that forms at prolonged exposure at intermediate temperatures from γ'' [110]; Laves phase with an embrittling topologically close pack (TCP) phase; carbides and borides that prefer to reside on the grain boundaries [111, 112, 113]. However, the usage of PBF IN718 (AM IN718) in aeroengines has been limited owing to the presence of undesirable phases [11] and its unconventional microstructure [11, 12, 13]. Efforts have been made to limit these defects through the use of heat treatment

[11, 102] and hot isostatic pressing (HIP-ing) [96], but the results have been mixed and no significant improvements have been made on PBF IN718.

2.2 Microstructure of AM IN718

2.2.1 Grain structure

Grain structure constitutes both grain size and grain texture of the material. Unlike its wrought counterpart, AM IN718 displays a mixture of columnar and equiaxed grains when no additional heat treatment is applied. This is due to its uneven cooling rate as the material is being built up layer by layer. Factors such as heat flux and thermal gradients greatly affect the growth of the grains, and this important area is discussed in detail in the literature [71, 114, 115, 116]. Ahmad et al. [11] showed that AM IN718 has columnar grains growing parallel to the building direction. An electron microscopic image of the microstructure of AM IN718 without any additional treatment is shown in Figure 2.2.

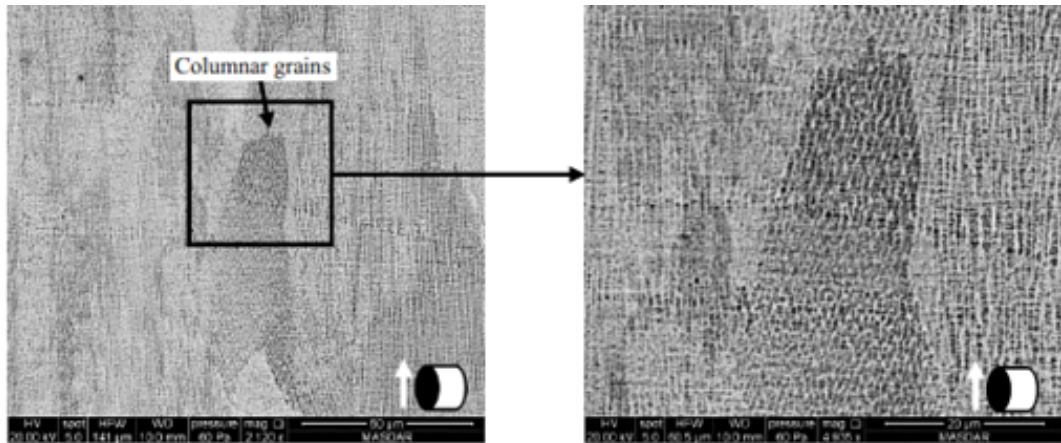


Figure 2.2: An electron microscopic image showing the columnar grains of AM IN718, retrieved from [11]

Gribbin et al. [19] took one step further and utilized EBSD to investigate the crystallographic structure of the material. As-built AM IN718 exhibits columnar dendrites structure with a moderate $\{100\}$ fibre texture formed along the build direction. These varying structure were correlated to the multiple heating and cooling cycle induced by the laser process [117]. Studies on various laser process in IN718 concluded that higher ordered columnar dendrites are established due to the increase of base cooling effect during the deposition [118]. The elongated grain growth is along the Z-direction as this is the primary direction of thermal flow which is align

with the $\{100\}$ direction [119]. Fatigue strength of the wrought alloy outperforms the AM alloy at room temperature (RTP), suggesting the grain texture is likely the main competing microstructural feature affecting the fatigue performances at RTP. The microstructural study findings were comparable to other studies [112, 83, 12, 100], although fatigue life of wrought alloys is known to be generally dominated by key characteristics such as surface roughness [120, 121, 37, 53], porosity [91, 122], coarse precipitates [83] and residual stress distribution [123]. Thus, the conclusion made by Gribbin et al. [19] might be incomplete and further investigation has to be made. The fatigue response of the as-built AM material had a similar response to the wrought material at an elevated temperature of 500°C. Both materials had a fatigue limit of approximately 600 MPa [19] despite AM IN718's inherent weakness of high content of coarse δ precipitates, which is known to deteriorate the fatigue behaviour at high temperature. This suggests that the difference in microstructural features is not as pronounced in high temperature environments as compared to the RTP condition.

Another interesting finding on wrought IN718 at elevated temperature has shown that the coarse-grain alloy has a fatigue strength significantly lower than fine-grain alloy when it is beyond 10^5 cycles [111]. It is likely that in order to maximize the AM IN718 capability in high temperature applications, controlling the grain size of the alloy will be vital, and any grain size refinement technique for AM metal alloys will be welcome.

2.2.2 Effects of δ phases

IN718 is a precipitation-strengthened nickel-based superalloy with γ'' as the main phase contributing to its excellent high temperature strength [124]. However, the metastable γ'' phase easily transforms to a stable δ phase under certain thermal conditions, decreasing the volume fraction of γ'' , which indirectly affects the mechanical properties of the alloy [125]. It is generally undesirable as it is known to decrease the fracture toughness and ductility of the material. δ precipitates are usually formed during the heat treatment process or during service, and mainly resides at grain boundaries. However, there are cases where δ precipitates have shown to display beneficial effects such as grain stabilization [44] and increasing stress rupture resistance [126]. An et al. [127] investigated the role of the δ phase for fatigue crack propagation behaviour in wrought IN718 and showed that the growth rate increases with increasing δ phase volume fractions. There were both long needle-like and granular shaped δ precipitates present in the alloy which have very different effects on the fatigue crack growth. When γ'' transforms into long needle-like δ precipitates, precipitates free zone formed around the δ phase, inhibiting micro cracks

that are detrimental to the fatigue performance of the alloy. While the granular shaped δ precipitates, with low length-diameter ratio, act as a pin between the grain boundaries, increasing the strength of the alloy.

AM IN718 usually has a slight variation on the volume fraction of its respective phases. In Gribbin's study, the δ phase content in wrought IN718 was $1.6 \pm 0.5\%$ while the as-built AM IN718 contained $3.8 \pm 0.4\%$ [19], which is rather unusual for the IN718 alloy. The increase of the δ phase content could be due to the heat treatment used to solution treat the alloy, leaving the precipitates undissolved. Yang et al. [11] compared the microstructure and mechanical performances of PBF-fabricated IN 718 alloy in various heat treatment conditions. The results show that the morphology and distributions of the δ phase are key factors determining their high temperature performance. Too much coarse δ phase along the grain boundaries could cause dislocation to pile up [83], causing local stress concentrations and premature failure. Whereas the lack of the δ phase will reduce the strength of the alloy at elevated temperature as it will have limited influence of the pinning effect on grain boundaries.

Formation of intragranular δ precipitates was also observed in AM IN718, which is a common observation for IN718 alloy when the parameters of the heat treatment are not optimized [125]. Presence of high concentrations of niobium in the feedstock [19], combined with the inconsistent heat flux caused by heating and melting of the powder, is the reason why intragranular δ precipitates are formed. Maximizing the volume fraction of intergranular δ precipitates gives the alloy better ductility while a high amount of intragranular δ precipitates hardens the material [125]. The ratio between intragranular and intergranular precipitates could be a critical parameter in optimizing the mechanical properties at elevated temperature of AM IN718 based on the past studies.

2.2.3 Mechanical properties of AM IN718 alloy

Most of the data derived from the literature (refer to Publication 2 Table 4 for the full details) focuses on the static performance of the AM material with slight difference on the geometry or the direction of the test piece. Generally, a post-processing step such as heat treatment or HIP-ing gives a better tensile strength but with a slight dip in its ductility. There were some instances where the tensile properties were superior to the wrought ones, giving end users the extra confidence in employing AM IN718 on its production line. Researchers such as Strößner et al. [13] and Gallmeyer et al. [128] have attempted to optimize the heat treatment process by increasing its homogenization or ageing temperature and thereby controlling the

growth of the γ'' phase, and minimizing the impact of either the δ or Laves phases, resulting in an increase in the strength and hardness of the material.

Data showing the fatigue strength of PBF IN718 alloy is limited in the literature, as these tests are more costly. Fatigue tests are typically conducted on servo hydraulic test machines which are capable of applying large amplitude cycles over a long period of time [21]. It is heavily used in high-value industries such as the aerospace and oil and gas sectors [129] where safety standards are much stringent than in other sectors. For AM IN718 alloy to be used in a safety-critical application, it is vital to understand the process-structure-property relationship, and the availability of fatigue data gives extra confidence for manufacturers to utilize this technology. At the same time, several problems such as weak grain texture in a certain direction and detrimental residual stresses [20, 18, 19] have to be dealt with in order to widen the adoption of AM IN718 alloy. This drives a need to introduce novel post-processing methods to improve the quality of AM products, which will be discussed in the next section. Interested readers could refer to Appendix G for the compiled fatigue data by the author and literature on the effect of defects in AM parts pertaining fatigue performance [130, 131].

2.3 Laser Shock Peening process

2.3.1 Introduction

Laser peening or laser shock peening (LSP) is a surface enhancement process used to impart beneficial residual stresses in materials which could trace its roots back to Battelle laboratories from Ohio. It is mainly used to enhance resistance to fatigue [132], fretting [133] and stress corrosion cracking [134]. General Electric Aircraft Engines (GEAE) adopted this technique in its production line of F101 fan blades in 1998 [135].

Despite the long presence in the aerospace industry, the LSP process is a niche technique where only a handful of companies are providing the technology. This is due to the multi-disciplinary specialisation needed to understand the technique and the high investment cost [136] needed to set up the process. Currently, the Q-switched laser system with neodymium-doped glass or yttrium aluminium garnet (YAG) crystal lasing rod has the capability to fulfil the requirements needed for the LSP process. It can produce beams of 80 – 100J output energy that are less than 30 ns in duration [137]. When the targeted area is irradiated with such high energy short pulse width laser, instantaneous vaporisation of the surface layer generates a high-pressure high temperature plasma. Laser spot diameters used in the industrial

settings are typically in the range of 2 – 7 mm.

The pressure shock wave that is created by the plasma propagates into the substrate, inducing beneficial compressive residual stress. Plastic deformation occurs when the shock wave pressure exceeds the dynamic yield strength of the metal, which results in high dislocation multiplication and movements which affect the microstructure and properties of the material. The maximum pressure induced by a short pulse laser in a transparent confined layer is proportional to the square root of the laser power density and is independent of the laser pulse duration or wavelength [138]

In order to reduce the amount of heat generated during the plasma generation, a sacrificial coating such as black paint or adhesive tape, is applied over the targeted area. This is to prevent heating/melting on the target, resulting in an unintended tensile residual stress introduced [139].

A transparent overlay such as water or glass are used over the aforementioned sacrificial layer to increase the shock wave [140], as shown in Figure 2.3. The use of transparent overlay has been found to increase the shock wave intensity propagating into the metal by up to two orders of magnitude, as compared to plasmas generated in a vacuum [141]. The water acts as an amplifier and a container of the heated plasma in the target region as it creates the high amplitude-short duration pressure shock wave required.

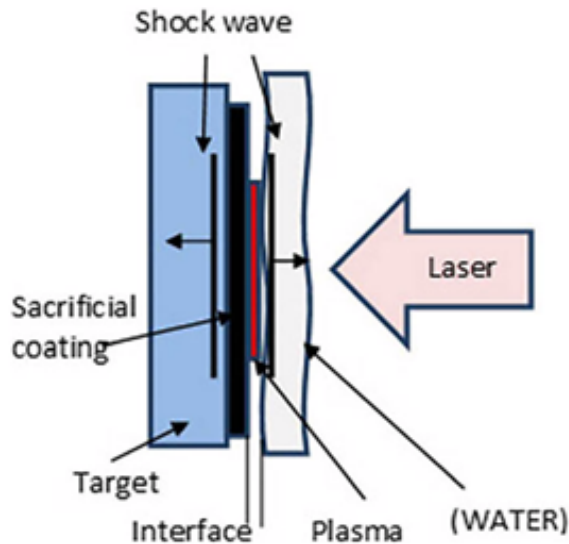


Figure 2.3: Mechanism of shock wave creation in the LSP process, retrieved from [135]

2.3.2 Effects on material properties

Microstructure

LSP treated materials undergo high strain rates up to 10^6 s^{-1} , resulting in microstructural changes that can be seen on the surface. Grain refinement was seen in ANSI 304 stainless steel that was subjected to multiple laser shocks [142]. With the first LSP impact, mechanical twins (MT) subdivide the coarse grain into a thin twin matrix. Subsequent impacts further subdivide the blocks to become subgrain boundaries, which eventually forms equiaxed refined grains. A schematic illustration by Lu et al. [142] showed the microstructural evolution on the top surface induced by multiple laser shocks, as shown in Figure 2.4

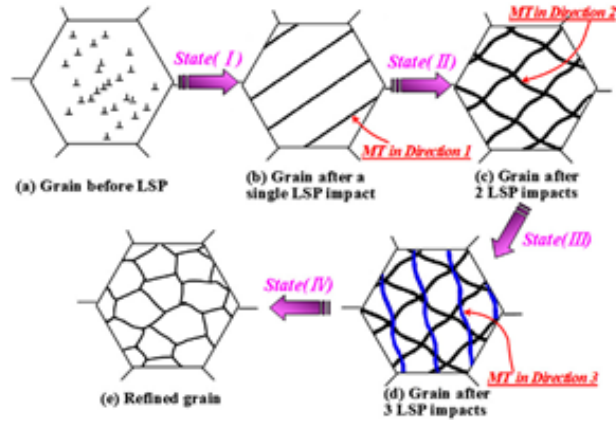


Figure 2.4: Schematic illustration of grain refined through multiple LSP impacts, retrieved from [142]

Similarly, Zhang et al. [134] observed that LSP on AZ31B Mg alloy, which has a coarse grain size in the range of 5 - 20 μm , created a relatively homogeneous fine-grained microstructure with an average grain size of 5.8 μm after four laser impacts, as shown in Figure 2.5. In addition, the depth of the compressive residual stress after LSP could reach up to about 0.8 mm from the surface by increasing the number of laser impacts. The effective region remained at 0.8 mm from the surface even after four laser impacts, suggesting that the effect of LSP has saturated. The grain size changes are attributed to the high strain plastic deformations which were induced by LSP, similar to what Lu et al.[142] has reported.

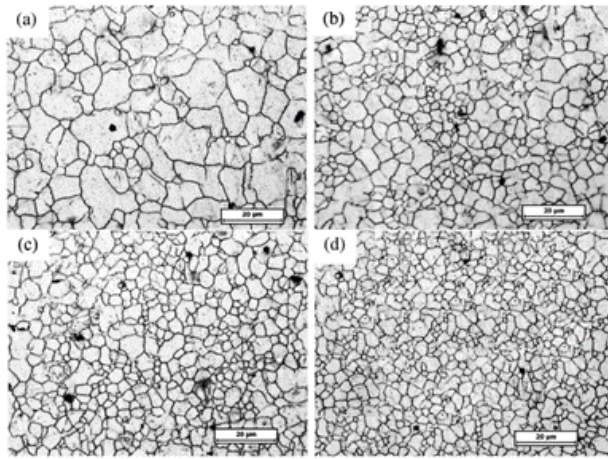


Figure 2.5: Optical microscope on the surface of AZ31B Mg alloy at 0.8 mm below the surface (a) before LSP; (b) with one impact; (c) with two impacts; and (d) with four impacts, retrieved from [134]

Plastic deformation

Plastic deformation or cold work arises from the distribution of dislocations or with other defects such as second-phase particles. A number of papers have reported that the improvement in mechanical properties of metal alloys that were LSP-ed was due to the generation of dislocations near the surface layer [143, 144, 145]. To understand the high strain process such as LSP, TEM is often used to visualise and understand the deformation at lower length scales. For example, it was used to investigate the dislocation movement in 6061-T6 aluminium alloy that was subjected to LSP [145]. 6061-T6 aluminium alloy has needle-shape precipitates that contribute to strengthening and hardening of the material by hindering dislocation mobility [146]. By studying both the dislocation's movement and the precipitates present in the alloy, Binol et al.[145] hypothesized that the precipitates could be formed through the thermally activated high strain deformation caused by LSP, which generates temperatures equivalent to the ageing temperature of this alloy [145]. Altenberger et al.[143] observed that the highly tangled and dense dislocation substructure formed at the near surface layer were stable up to 800°C after LSP was performed on AISI 304 alloy through the use of bright field images, as illustrated in Figure 2.6. These high dislocation densities were believed to act as obstacles to stable dislocation slip, improving resistance to fatigue crack initiation and thus increasing fatigue life.

Kattoura et al.[147] concluded that the increase in dislocation density caused by LSP on the near surface layer of ATI 718Plus alloy gave better fatigue resistance at high temperature. The authors preliminary concluded that the LSP material is much more capable of withstanding plastic strain prior to failure due to its formation of dislocation entanglements and slip bands that created a barrier that hinders the nucleation and propagation of fatigue cracks. However, no comparison were made between the LSP-ed and pristine material. The dislocations that were present in the LSP ATI 718Plus alloy may already be there in its pristine state due to other processes.

Table 2.3: Comparison of cold work provided by shot peening and LSP

| | Strain rate (s^{-1}) | Cold work (Depth (mm)) | Typical roughness Ra(μm) | |
|--------------|------------------------------------|-------------------------------------|---|------------------|
| Shot Peening | $10^3 - 10^4$ | 15 – 50 | 0.2 | 4.52 (X20 Steel) |
| LSP | $10^6 - 10^7$ | 5 – 7 | 1.2 | 0.98 |

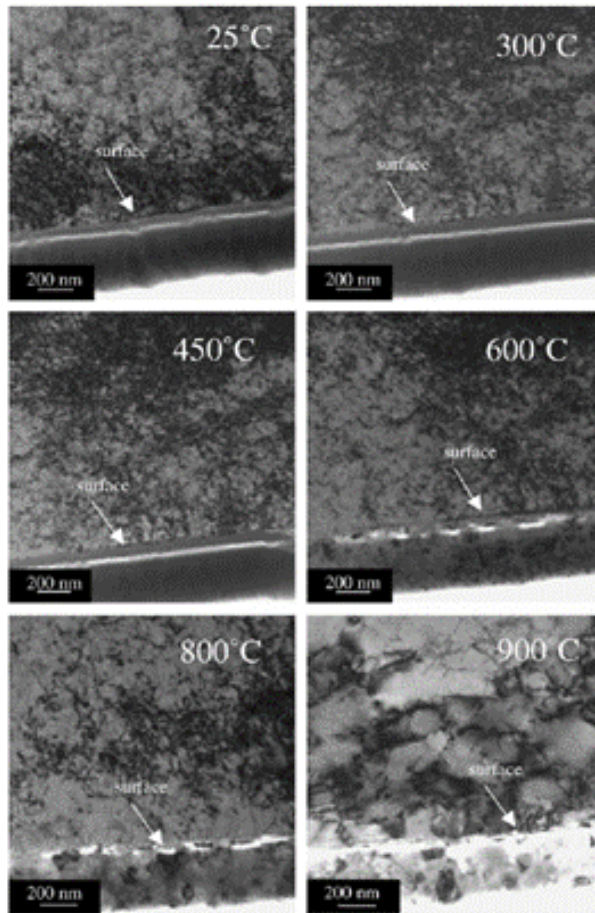


Figure 2.6: Near-surface microstructure of LSP AISI 304 after thermal exposure between 25 to 900°C, retrieved from [143]

Table 2.3 compares the effects of shot peening and LSP on X20 steel [135]. LSP brings about a significant lower cold work as compared to shot peening. It was also observed in Ti-6Al-4V alloy [148] and IN718 coupons where the cold work was approximately 2% [135]. The difference between the X20 Steel and IN718 alloy is mainly due to the material's deformation capability. Although it is beyond the scope of this work to discuss shot peening, it is useful to bring it up as a comparison to LSP as it is a widely adopted technique in the aerospace industry. Shot peening involves multiple steel or ceramic shots projected at a high velocity through a nozzle, to strike the surface of the work-piece with force sufficient to create plastic deformation. Due to the continuous shots, most of the energy is expended in inducing plastic deformation, resulting in a highly cold worked surface layer [148]. On the other hand, LSP produced remarkably little cold work on the surface [149], as shown in Figure

2.7. A high degree of cold work has been found to relax rapidly at high temperature [147, 149, 148] which is detrimental for high temperature application in the nuclear and aerospace industry. Figure 2.8 illustrates the difference in performance of IN718 coupons under high temperature that has been subjected to both shot peening and LSP. At the surface, the cold work produced by shot peening is completely lost after thermal exposure of 670°C for 10 minutes. The thermal relaxation occurred in shot peened IN718 alloy appears to follow the Avrami diffusion model described by Eigenmann et al. [150] which states that it progress in two stages – a fast and rapid first stage and a steady transient secondary stage. Whereas IN718 coupons that were LSP-ed show no indication of thermal stress relaxation at any depth or exposure time at the same temperature. Consequently, LSP technology is a more suitable technology as it has a significantly lower cold work that gives better performance in a thermomechanical loading environment.

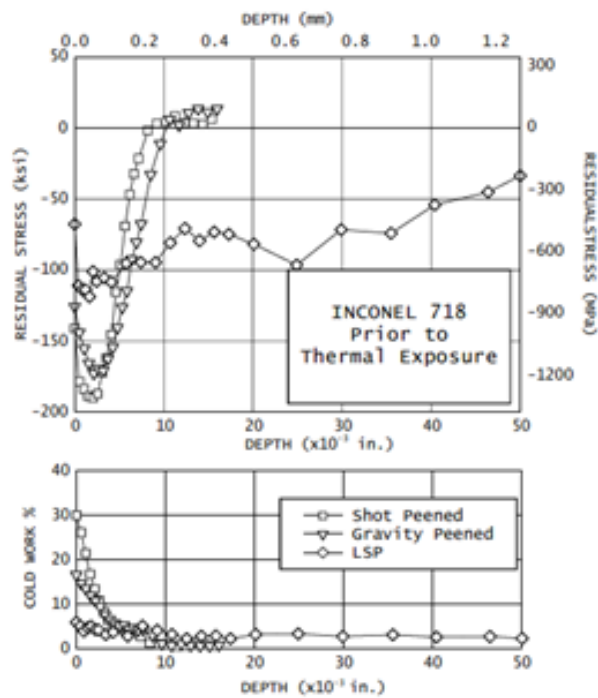


Figure 2.7: Residual stress distribution and cold work developed by in IN718 coupons using various surface enhancement process, retrieved from [148]

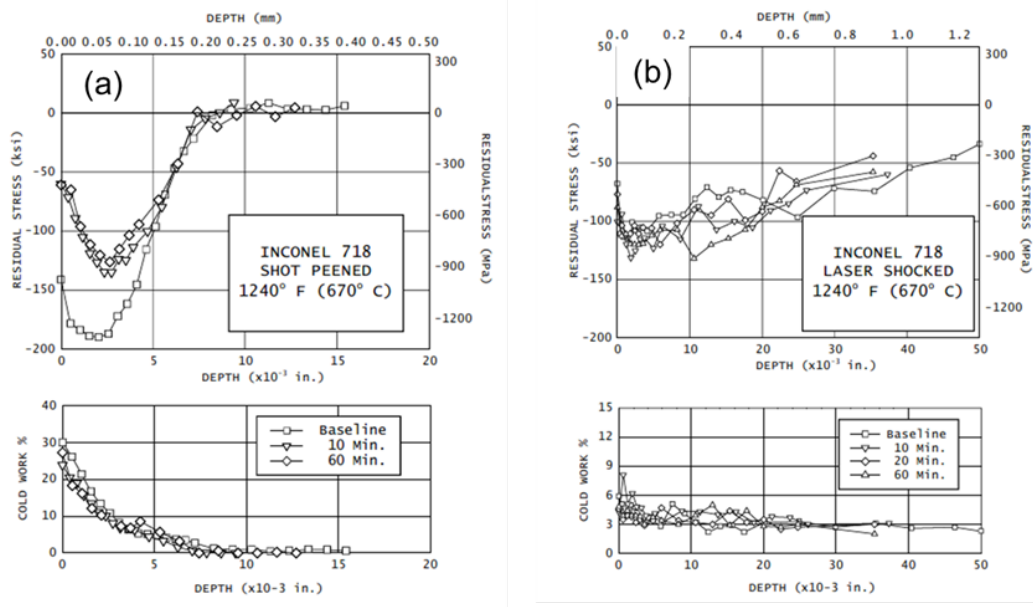


Figure 2.8: Effect of thermal relaxation of IN718 at 670°C that has been subjected to both shot peening and laser shock peening, retrieved from [148]

2.3.3 Performance of LSP wrought IN718

In general, LSP imparts deep compressive residual stress, generates dislocations near the surface layer [143, 144, 145] and refines the grain size to improve the material's mechanical properties. To the best of the authors' knowledge, data regarding the performance of LSP wrought IN718 remains elusive. First known set of LSP IN718 data came from Prevey et al. [148] when the technique was still in its infancy stage. Gill et al. [151] took a step forward by making a detailed comparison of LSP technique on IN718 with other surface enhancement processes. LSP treated IN718 showed a small increase in surface roughness and no grain size modification was observed. LSP showed a 20% increase in hardness at the surface with a maximum residual stress of 750 MPa. Residual stress fields were bi-axial in nature and a moderate density of dislocations were found on the samples. Kattoura et al. went on to evaluate LSP treated IN718 in both RTP [152] and heated environment [147]. Results have shown that the fatigue life of LSP IN718 in RTP and 650 °C were significantly higher than the pristine specimen. The combined effects of high magnitude retained compressive residual stress and the presence of high dislocation density delayed the specimen crack initiation and propagation efforts. Overall, LSP has demonstrated its benefit of low cold work and deep compressive stress on IN718 specimens and further proved that it's a suitable technique to utilise in a high temperature environment.

2.3.4 Suitability of LSP on AM IN718

LSP is also being used as a post-processing method for AM metal components such as aluminium [153], stainless steel [154] and titanium alloy [155]. Kalentic et al. [156, 154] have proposed to use LSP to tailor the residual stresses of stainless steel samples by moving the baseplate back and forth between a printing machine and a LSP station. Dubbed it 3D LSP, an ex-situ LSP combined with the AM process has shown to increase both magnitude and depth of compressive residual stress. This is an effect that is highly sought after for AM components with detrimental residual stress [20, 18, 19]. The depth of compressive residual stress can reach up to a depth of 1 mm for AM 316L stainless steel component subjected to the 3D LSP principle, as shown in Figure 2.9.

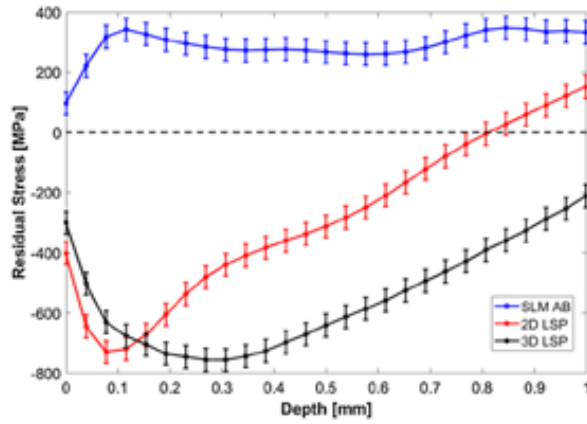


Figure 2.9: Residual stress curve measured for 316L stainless steel for as-built (AB), LSP after AM (2D LSP) and ex-situ LSP on AM (3D LSP), retrieved from [154]

AM IN718 has shown to exhibit favourable strength in low-cycle fatigue (LCF) environment comparable to conventional IN718 in RTP environment, especially in low strain amplitudes [157]. In addition, very-high-cycle fatigue (VHCF) behaviour of AM IN718 at 650 °C was seen to be comparable to the wrought counterpart [158]. There is mounting evidence that AM IN718 can have comparable mechanical properties to its wrought counterpart. The integration of LSP with AM IN718 will further enhance the effectiveness of the material in high temperature environments. The main aim of this thesis is to provide a better understanding of the fatigue behaviour of LSP treated AM IN718 used in high-temperature applications.

2.4 Summary and gaps in literature

The sections covered in this chapter span across multiple topics. Each section provides a brief background as well as the current status of the relevant research. There are specific gaps in the literature that haven't been identified so far:

- There exists a shortage of studies investigating the fatigue properties of AM IN718 alloys. Among the seven processes, the PBF technique was identified as the most viable method for high quality parts. However, current state-of-the-art lacks the required industrial research to put it in use for a critical component
- LSP process was identified as a suitable surface enhancement process for high temperature fatigue environment as it could maintain low cold work and at the same time induce deep compressive stress to the material
- LSP was shown to give enhanced mechanical performance in other AM materials such as stainless steels and aluminium alloys. There was a knowledge gap for surface enhanced AM IN718 alloys. Thus, it is crucial to assess the suitability of the LSP process of AM IN718 alloys in various conditions that represents a real aeroengine environment

Chapter 3

Experimental methods

This chapter presents the materials and the experimental methodologies employed in this work. Firstly, the PBF system utilised for fabrication of the specimens is introduced and the following manufacturing processes were explained. The steps taken to process the synchrotron X-ray diffraction data to produce residual stress measurements were included. Finally, the equipment and methods utilised for mechanical testing of the AM specimens are presented in this chapter.

3.1 Powder Bed Fusion

3.1.1 Material specifications

Samples used were prepared by the PBF using an EOS M280 (EOS GmbH, Germany) machine with a 400W fibre laser. The chemical composition of the specimens was sent to IMR test lab and prepared using the inert gas fusion techniques to analyse the chemical composition. It was tumble at 15 RPM for 30 minutes and dried at 80°C for more than 12 hours as prescribed by ASTM E1019-18 standards. The chemical composition of the specimens used in this experiment is given in Table 3.1 (refer to Appendix B for more details)

Table 3.1: AM IN718 initial powder chemical composition w.t %

| Ni | Cr | Nb | Mo | Ti | Al | Co | Cu | C | Si | Mn | Fe |
|-----------|-----------|-----------|-----------|-----------|-----------|-----------|-----------|----------|-----------|-----------|-----------|
| Bal | 18.98 | 5.22 | 3.07 | 1.01 | 0.50 | 0.08 | 0.02 | 0.04 | 0.02 | 0.02 | 17.89 |

3.1.2 Processing parameters

The specimens were built using a laser power of 285 W, scan speed of 960 mm/s and a layer thickness of 40 μm and a beam spacing of 110 μm , as suggested by the machine manufacturer. They were built vertically upwards along the Z axis with the specimen build orientation along 67° on the XY plane in an Argon environment.

3.1.3 Geometry

Specimens were designed to facilitate easy access to both the LSP machine and the SXRD measurements. Flat dog-boned tensile geometry was used and adhere to the prescript recommendation given in BS EN 3987:2009. Details of the specimen is specified in Figure 3.1.

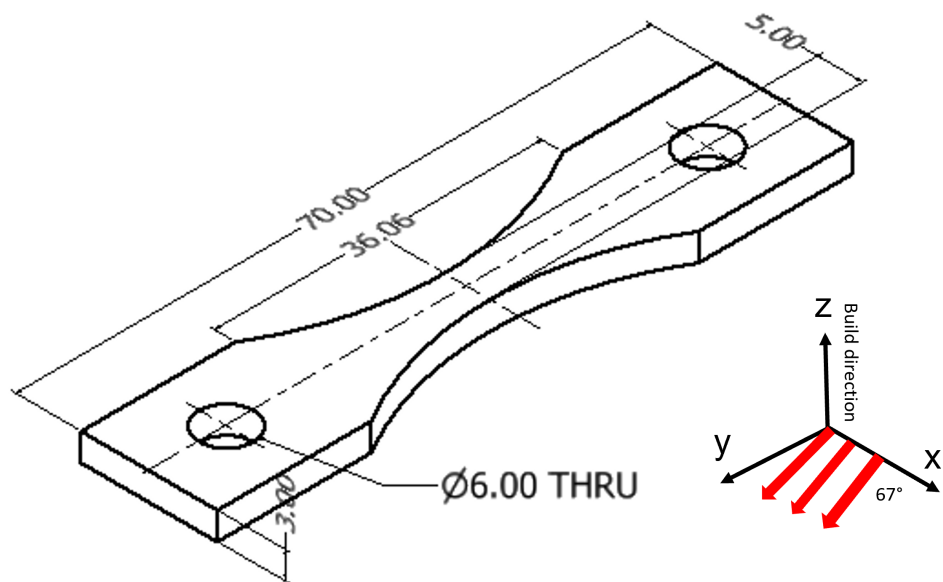


Figure 3.1: Schematics of a dog-boned geometry specimen showing the build and powder layering direction

3.1.4 Heat treatment

The specimens were heat treated according to Aerospace Material Specification (AMS) 5663, where it was solution annealed at 980°C for 1 hour and aged at 720°C for 8 hours in an argon environment and later air cooled. It was then wire cut from the base plate after the heat treatment through an in-house Electrical Discharge Machine (EDM) CUT 300 Sp (GF Machining Solutions, Switzerland) to prevent any unnecessary cold work from being introduced.

3.1.5 Milling

Lastly, the specimens were sent to a local machinist workshop (Whits Technologies, Singapore) to mill the surface of the specimens to a Ra value of 0.2 μm .

3.1.6 Wrought

Conventional wrought IN718 were purchased and machined into the desired geometry from a local machinist workshop (Whits Technologies, Singapore). The specimens were also heat treated according to Aerospace Material Specifications (AMS) 5663.

3.2 Laser Shock Peening

3.2.1 Processing parameters

An industrial laser shock peening system YS120-R200A (Tyrida International Pte Ltd, Singapore) was used for the experiment. It was conducted at room temperature using a Q-switched Nd:YAG laser that operated at a wavelength of 1064 nm, a pulse repetition rate of 5 Hz and a pulse duration of 18 ns. The specimen was held with a fixture mounted on a six-axis robot arm and placed precisely normal to the incident laser beam at a focal plane position for peening, as shown in Figure 3.2a. A protective black tape overlay was utilized to protect the surface from the thermal effects of the laser beam. LSP was performed with single pulse impact and deionised water with a thickness of 2 mm flowing onto the targeted area as a transparent confining media. Figure 3.2b shows the peening strategy. The laser peen pattern was designed to be applied in four steps to achieve a complete coverage on the area. The spots were peened one by one following the robot movement sequence. With step 1 as reference, laser spots for steps 2, 3 and 4 were translated in x, y and diagonal directions respectively by 1.5 mm to achieve complete coverage of the peened surface. For the selected geometry, applying the LSP process on the

opposite sides of the section is recommended to balance the generated force. Two-sided peening is used to avoid harmful effects such as spalling and fracture. A laser peak power density of 7.1 GW/cm^2 was selected as it was deemed to be the lowest cost option. Interested readers could refer to the Appendix F on the paper written by the author.

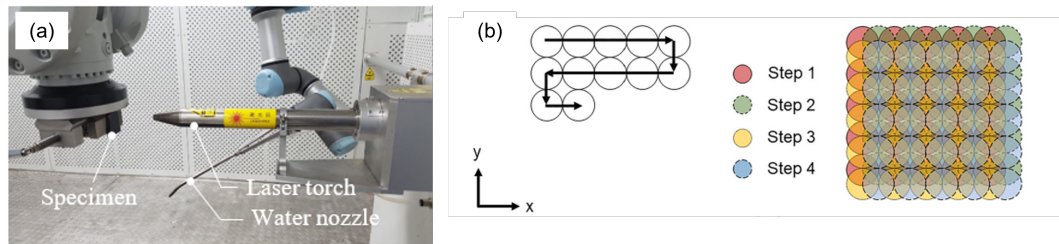


Figure 3.2: (a) Experimental setup of the laser shock peening process using a robotic arm and (b) the four step peening strategy

3.3 Surface roughness measurements

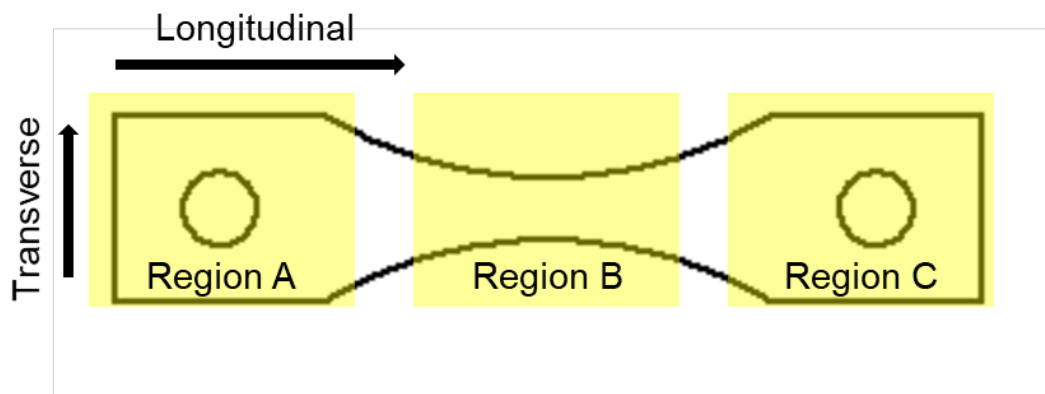


Figure 3.3: Surface roughness measurements segregated into three regions

A stylus profilometer (PGI 800; Taylor Hobson) was used to determine the R_a in the longitudinal and transverse directions for the surface roughness measurement, as seen in Figure 3.3. Three regions were identified on the specimen. Measurements for each direction in each region were performed three times with a sampling length of 0.8 mm and the average of these measurements was reported as surface roughness for each direction of the regions. Transverse readings on Region B were not taken as there was not enough runway to take a statistically accurate measurement.

3.4 Stress measurement

3.4.1 Synchrotron X-ray Diffraction (SXRD) processing parameters & setup

SXRD was employed to measure the strain induced by the LSP process and the experiment was conducted using the I12 beamline at Diamond Light Source (Oxford, UK). In order to capture the highest resolution required in the shortest possible time, a beam energy of 123 keV and a wavelength of 0.1 Å were utilised. At this wavelength, the beam can penetrate hard metals such as IN718 and provide a unique insight into these type of polycrystalline material. An automatic XYZ translator was fitted onto the stage and the beam was scanned vertically from top to bottom. The gauge volume was fixed in space and the specimen was translated with a step size of 10 µm to make measurements through the depth, with each stepping point taking approximately 10 seconds of exposure time. Figure 3.4 shows the experimental setup at the DIAMOND facility.

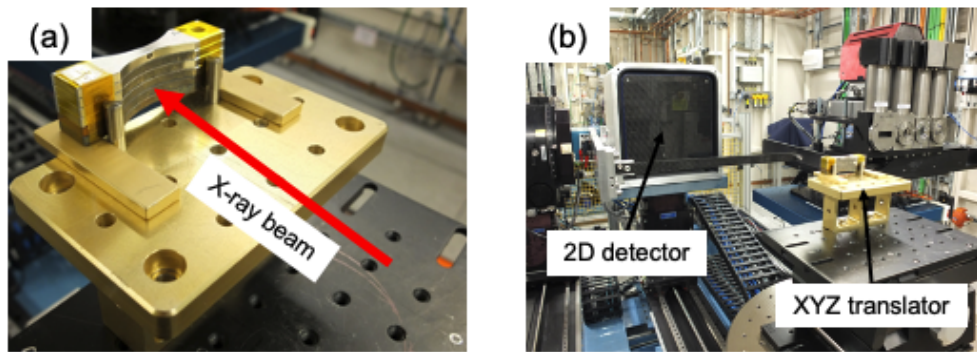


Figure 3.4: (a) Samples stacked together with the beam line scanning it vertically and (b) photo of the experiment setup in DIAMOND I12 facility

3.4.2 Data processing

Raw 2D diffraction images were captured by the large area 2D detector and processed using proprietary DAWN software developed by DIAMOND developers [159, 160]. First, masking was initialised to phase out the lower and upper limits. Subsequently, an entire cake remapping was performed on the diffraction images with 36 Azimuthal bins, accounting for 10° for each bin. In this setup, the horizontal position is defined as the starting point, 0° and rotating clockwise is positive. In particular, the bin, which account from -5° to 5° from the diffraction image has

been used to measure the in-plane stress, as shown in Figure 3.5. Reflections from

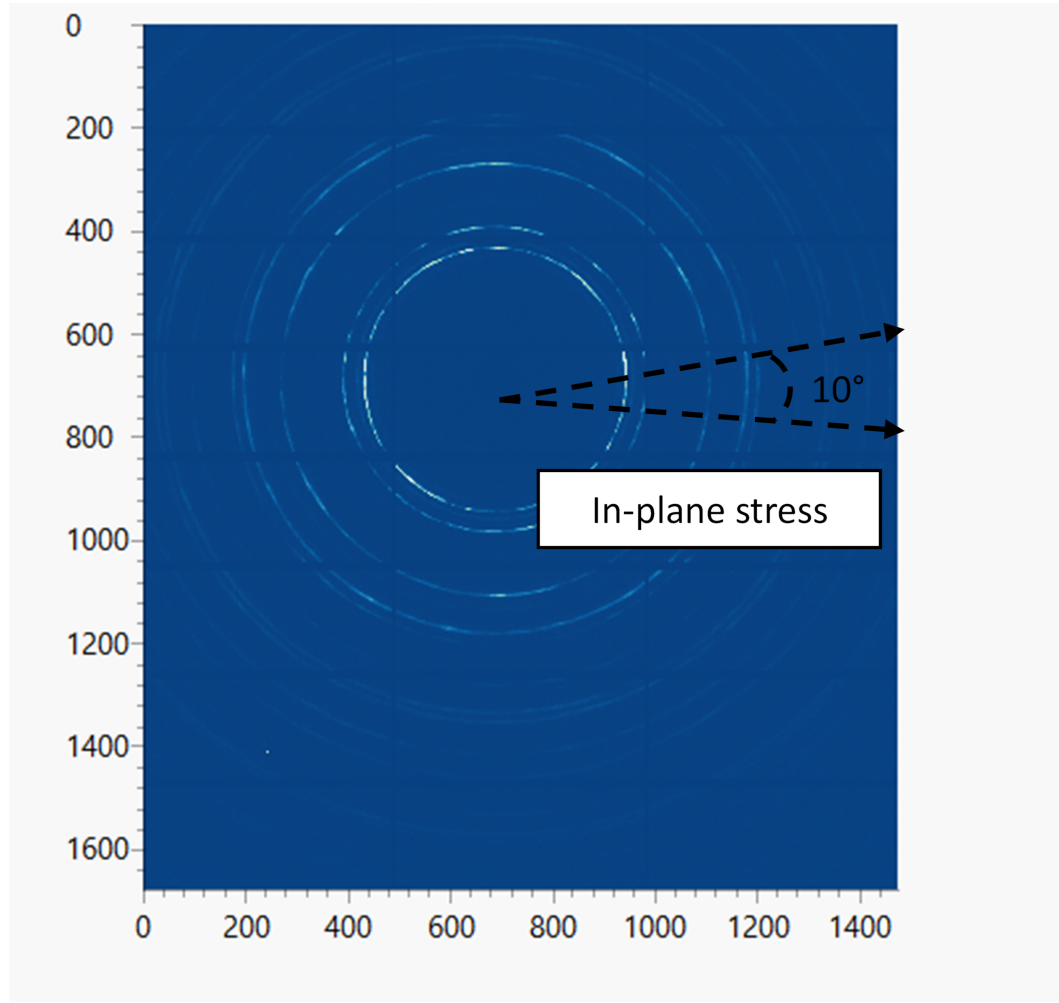


Figure 3.5: Raw diffraction images with the selected Azimuthal slice which correspond to the in-plane stress

the $\{311\}$ planes represent a reasonable average strain in the crystallographic unit cell of lattice strain applied in both wrought [161] or AM IN718 alloy [162]. $\{311\}$ peaks are considered to be representative of the bulk behaviour as it is insensitive to intergranular strain development in Nickel-based superalloys [161]. The choice of $\{311\}$ was made recommended to be used as the diffraction reflections as prescribed by the ISO 21432:2019 standard [163]. The diffracted intensity was determined by fitting a Gaussian function peak profile by least square regression after correction for a flat background, as directed by BS EN ISO 21432. The processing was built using the LMfit library that is based on the Python language. The peak positions,

full width half maximum (FWHM) and their respective standard errors were computed by the processing pipeline. An example of the fitting function is showcased in Figure 3.6 (refer to Appendix E for the Python code). Data for the peak position

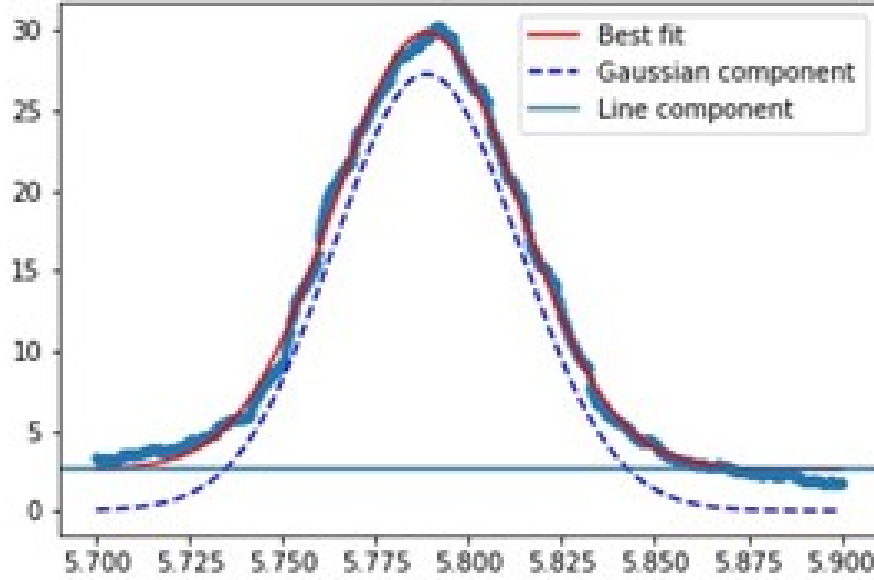


Figure 3.6: Example of a fitted Gaussian peak profile with a flat background using the LMfit library

can be converted via the Bragg diffraction equation [164];

$$2d_{\{hkl\}} \sin(\theta) = n\lambda \quad (3.1)$$

where λ is the X-ray wavelength, d is the lattice spacing and θ is the Bragg angle of the relevant hkl planes. For the sake of simplicity, the momentum transfer in reciprocal-space (q) is used where

$$q = \frac{2\pi}{d} \quad (3.2)$$

Strain can be obtained simply from [165]

$$\epsilon_{\{hkl\}} = \frac{q_{0\{hkl\}}}{q_{\{hkl\}}} - 1 \quad (3.3)$$

where $q_{0\{hkl\}}$ is the strain free reciprocal-space reflection used for the specified set of lattice planes and is referred to q_0 hereafter. Elastic strains measured can be then converted to stresses via standard mechanics of solid [165];

$$\sigma_x = \frac{E}{(1-v)(1-2v)}[(1-v)\epsilon_x + v(\epsilon_y + \epsilon_z)] \quad (3.4)$$

where ϵ is the stress state for the corresponding x, y and z directions, elastic modulus $E = 170$ MPa and was gathered from various literature sources [166, 167], and Poisson's ratio $v = 0.29$ [166, 167]. In this experiment, the stress component in the through-thickness direction (y-axis) is assumed to be zero and the in-plane stress (x and z-axis) is isotropic [168]. In this case, it is possible to calculate the in-plane stress (usually of most interest) from a single strain data;

$$\sigma = E \frac{(\epsilon + v\epsilon)}{(1-v^2)} \quad (3.5)$$

3.4.3 Strain free reference

Determination of q_0 is not trivial and can be formulated either by choosing a point where the strain-free point is most likely to be observed [169] (i.e. far away from the LSP area) or an average of values over the strain-free specimen. In this experiment, an average value of q was used over the pristine AM specimen as it has been part of the stack and acts as a means of control over the quality of the data.

3.4.4 Propagation of errors

$$\frac{\sigma_{\epsilon\{hkl\}}}{\epsilon_{\{hkl\}}} = \sqrt{\left(\frac{\sigma_{q_0}}{q_0}\right)^2 + \left(\frac{\sigma_{q_{hkl}}}{q_{hkl}}\right)^2} \quad (3.6)$$

The estimated standard error of q_{hkl} is determined by inverting the Hessian matrix which represents the second derivative of fit quality. ϵ_{hkl} is derived from the division of q_{hkl} and as a result its respective standard error is propagated by the two variables [170]. Derived standard error were insignificant for each strain component and the cause for the difference lies in the varying grain size throughout the depth of the samples.

3.5 Phase identification using Powder Cell

Phases were determined by the full-profile analysis using the PowderCell software [171] that matches with the raw SXRD data. The compositions of individual phases

in the alloys were then simulated and determined from the crystallographic data in the literature source [172].

3.6 Cold work measurements

3.6.1 Preparation

Microhardness measurements to accompany the topographic data was used as a means to characterise surface hardening by the LSP. Specimens were sectioned using IsoMet 4000 linear precision saw (Buehler, U.S) and then compression mounted with conductive resin using SimpliMet XPS1 mounting system (Buehler, U.S). Subsequent polishing was performed using a MetaServe 250 grinder-polisher (Buehler, U.S) to obtain the desired surface quality. The top surface was mechanically polished with P240 grit SiC and subsequently with a series of cloths using 9, 3 and 1 μm diamond suspension. The final polishing was performed with 0.02 μm colloidal silica suspension.

3.6.2 Microhardness

Vickers hardness testing using 500 gF and a dwell time of 10 seconds was performed on the LSPed AM sample using Falcon 510 (Innovatest, Netherlands) , as shown in Figure 3.7a. Indentations were made on the sample edge vertically downwards towards the centre up to a depth of 1000 μm and horizontally up to a length of 1000 μm as well. A total of 100 indents were made on one specimen with no repeats. According to ASTM E9217, the distance between two indents or an indent and the edge of the test piece shall be at least two and a half times the diagonal of the indentation. In this particular setup, the diagonal of the indentation were between 42 to 45 μm giving a spacing of 100 μm sufficient enough to avoid interactions between the stress fields[173]. The experimental setup is illustrated in Figure 3.7b.

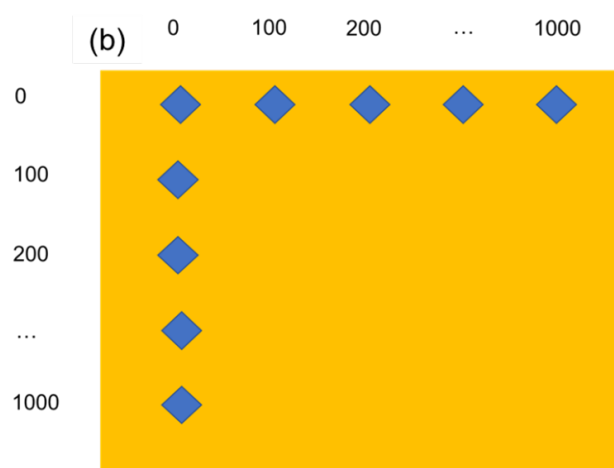
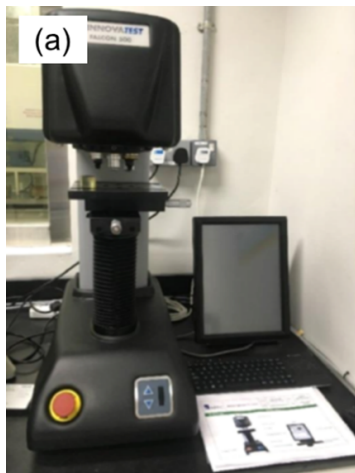


Figure 3.7: Photograph of (a) Innovatest Falson 510 indenter and (b) schematics of how the hardness measurement were collected on a cross-sectional LSP AM IN718 specimen

3.6.3 Full width half maximum

Profiles obtained from the synchrotron X-ray diffraction were fitted with a Gaussian function to obtain the characteristics of the peak. FWHM was used as an estimation of the level of plastic deformation. Generally, peak broadening can be affected by low-angle boundaries, very small grain size, plastic deformation as well as variations in macro or micro lattice strain.

3.7 Microstructure characterisation

The samples cross-sections were prepared to a finish suitable for use for electron backscattered diffraction (EBSD) analysis as described in Section 3.6.1. EBSD maps were collected from JSM 7800F SEM (JEOL, Japan) at 3000 Hz with a horizontal field of view (HFW) of 750 μm and a step size of 0.29 μm . One such scans were performed for the pristine AM and LSP AM IN718 specimens.

3.8 Mechanical test

3.8.1 Uniaxial tensile test

Three different mechanical tests were employed in this research and workpieces were first ground and polished to $0.2 \mu\text{m Ra}$ as per EN 3987:2009 standard. The specimens that were used has the same geometry as specified in Figure 3.1. The first mechanical test was an universal uniaxial tensile test to derive the static strength of the AM IN718 material. It was performed using a 30 kN load cell servo-hydraulic machine (Instron, U.S) at a cross-head speed of 0.166 mm s^{-1} with the longitudinal axis in line with the test load direction. It was carried out at room temperature with three repeated measurements. The extensometer was attached directly to the specimen gauge length during the test. Load, extension and stress were determined by Instron material testing software Bluehill version 2. Through the data collected, it was possible to determine the material yield strength (YS) and ultimate tensile strength (UTS). A stress ratio (R) of 0.1 was used in all three of the mechanical tests.

3.8.2 Thermal and mechanical loading

The stress relaxation of LSP specimens under various loading conditions was explored. A total of eight samples were chosen randomly from one build to avoid the influence of manufacturing defects. These samples were then divided into three conditions, with specimens going through a pure thermal load, pure mechanical load and a combination of thermal and mechanical loading. Testing was performed using a 25 kN load cell servo-hydraulic machine (Instron, U.S) with the longitudinal axis in line with the test load direction. The experimental matrix is listed in Table 3.2 and the loading setup is shown in Figure 3.8. The practical thermal limits of these alloys is in the range of 500°C to 650°C [174]. 550°C was selected as the middle ground and thus was used in all temperature-related experiments. The oven (Instron, U.S) was pre-heated to 550°C before the specimens were put into it. An exposure time of 1 hour was chosen as a large proportion of the total relaxation occurs in the initial exposure period [175, 176]. A 15 hour exposure time coincides with the time needed to run approximately 1,000,000 fatigue cycles in a 20 Hz setting. Similarly, a mechanical load of 30% yield strength [177] was used to replicate as close as possible the loading experienced in an aeroengine turbine section.

Table 3.2: Experiment setup of thermomechanical test

| Sample number | Loading condition |
|---------------|--|
| 1 | Pristine AM IN718 |
| 2 | LSP AM IN718 |
| 3 | LSP AM IN718 and thermal exposure for 1 hour with no mechanical load |
| 4 | LSP AM IN718 and thermal exposure for 15 hours with no mechanical load |
| 5 | LSP AM IN718 at mechanical load at 30% yield strength to 10,000 cycles at room temperature with $R = 0.1$ |
| 6 | LSP AM IN718 at mechanical load at 30% yield strength to 1,000,000 cycles at room temperature with $R = 0.1$ |
| 7 | LSP AM IN718 at mechanical load at 30% yield strength to 10,000 cycles at 550°C with $R = 0.1$ |
| 8 | LSP AM IN718 at mechanical load at 30% yield strength to 1,000,000 cycles at 550°C with $R = 0.1$ |

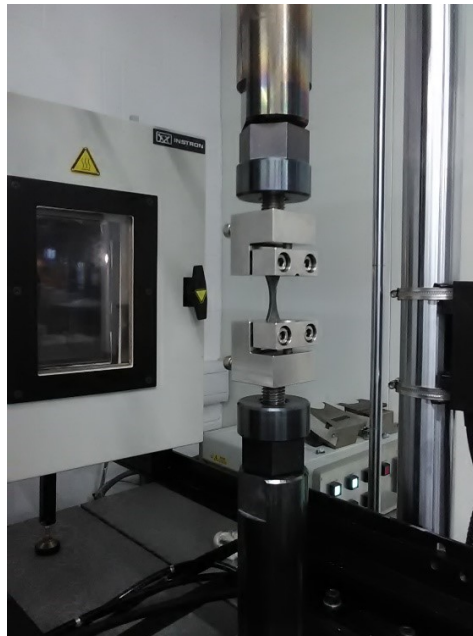


Figure 3.8: Photograph of the experimental setup of the thermomechanical test of 25 kN load cell Instron dynamic fatigue machine with oven attached to it

3.8.3 Three point flexural fatigue

A total of 29 samples were used to conduct the test and the number of cycles was recorded accordingly at both RTP and at 550°C. It was conducted according to the ASTM E739 standard. The three point flexural fatigue test was carried out on the same servo-hydraulic machine used in the previous section, as seen in Figure 3.9. All coupons were tested until failure or until runout of 1.5×10^6 cycles. The frequency of the fatigue test was set to 7 Hz with 10 N preload and step up to the desired testing force ranging from 700 N to 1500 N.

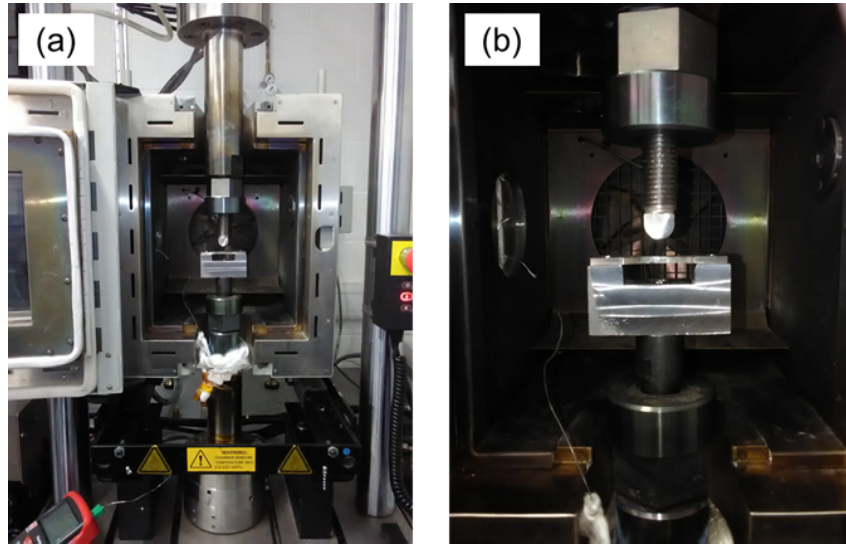


Figure 3.9: Photograph of the experimental setup of the three point flexure test

The calculation of the maximum bending stress was simplified as a cantilever

$$\sigma_{max} = \frac{3FL_i}{2bh^2} \quad (3.7)$$

where F is the load being applied, L_i is the distance between the two pin holes, b is the breadth of the specimen and h is the height of the specimen. Figure 3.10 describes the experiment setup with the specimen geometry as described in Figure 3.1. The peak stress produced in the three point flexure test is at the specimen mid-point with reduced stress elsewhere. Hence, this analysis (stress localization) is ideal to test for specific isolation of stress on the specimen and the effectiveness of LSP process.

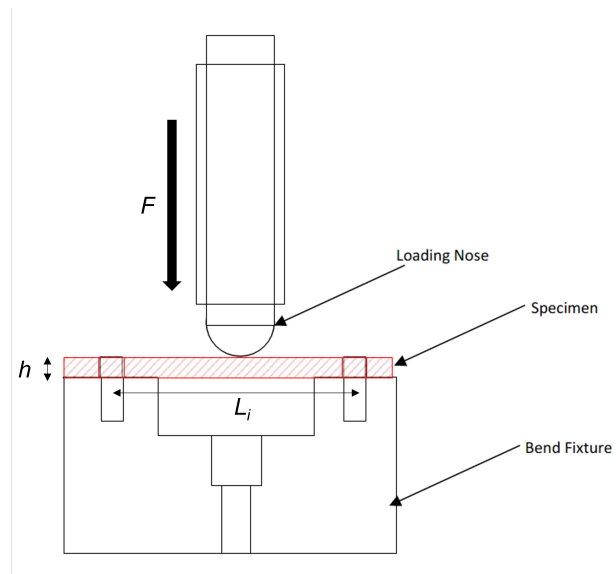


Figure 3.10: Schematics of the three point flexure test with the specimen

3.8.4 Fractography analysis

Fractography analysis of broken fatigue test specimens were outsourced to IMR Test Lab Singapore. It was performed on a VEGA3 TESCAN SEM at 20kV. Detailed reporting of the analysis can be found in the Appendix D .

Chapter 4

Results & discussions

4.1 Surface roughness

Table 4.1: Surface roughness Ra values of pristine AM and AM.LSP in both directions

| | Pristine AM | | AM.LSP | |
|----------|--|--|--|--|
| | Longitudinal (μm) | Transverse (μm) | Longitudinal (μm) | Transverse (μm) |
| Region A | 0.120 ± 0.005 | 0.556 ± 0.005 | 1.463 ± 0.005 | 1.520 ± 0.005 |
| Region B | 0.163 ± 0.005 | - | 1.342 ± 0.005 | - |
| Region C | 0.166 ± 0.005 | 0.547 ± 0.005 | 1.308 ± 0.005 | 1.400 ± 0.005 |

For the rest of thesis, AM IN718 specimens that were LSP will be abbreviated as AM.LSP. Two key observations can be seen in the measurement taken. Firstly, transverse measurements in pristine AM specimens are shown to be higher than that of the longitudinal direction, as shown in Table 4.1. This is due to the directional effect caused by the milling process to smooth the surface. Secondly, the use of LSP gave an approximately 10x increase of its Ra value, reaching up to a value of $1.52 \mu\text{m}$. In all three regions, the Ra values of both the longitudinal and transverse directions were very close as it has been shown that LSP is a bi-axial process [10] where the topography effect on both directions is uniform. The peening strategy that was employed in this experiment kept the Ra value low in the $1.3 \mu\text{m} - 1.5 \mu\text{m}$ range.

4.2 Phase identifications

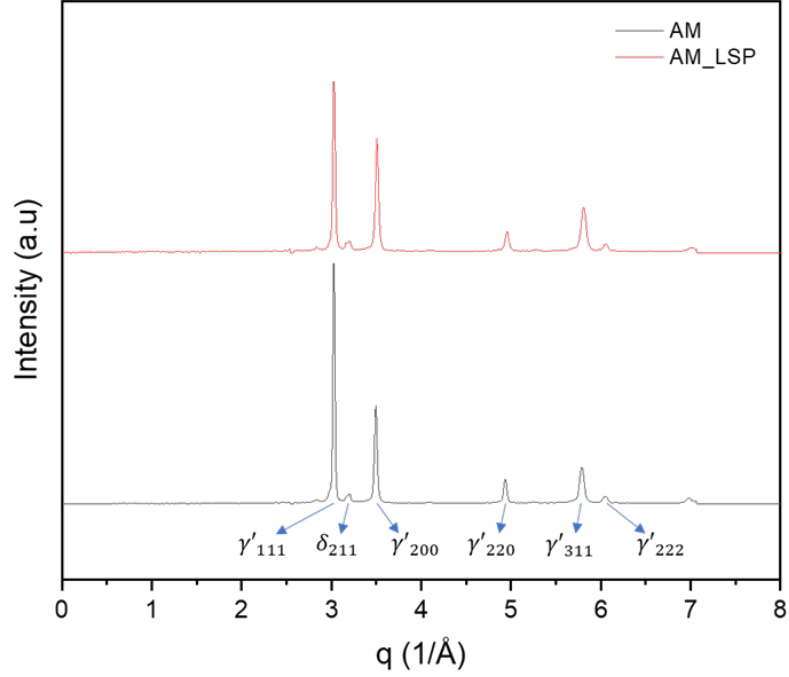


Figure 4.1: Phase identification using SXR data

Figure 4.1 displays the indexed and fitted AM and AM_LSP diffraction patterns using the raw SXR data on the PowderCell software where q is the momentum transfer in reciprocal-space that was defined in Chapter 3. The identified phases are γ' which correspond to (1 1 1), (2 0 0), (2 2 0), (3 1 1) and (2 2 2) planes respectively. The lapping of γ , γ' and γ'' makes it difficult to distinguish the distinct phases in the material [178, 179]. Both pristine AM and AM_LSP show no significant differences in their phase composition. There has not been any observations that the thermal or mechanical induced energy of LSP is capable of altering the phases of nickel alloy [180]. Chemical analysis and phase identification with SEM-EDS of AM_LSP are shown in Figure 4.2. Spherical and needle-like δ precipitates were observed in this region, area 1 and 2 respectively. EDS maps reveal that both the needle-like (area 2) and spherical (area 1) δ precipitates are enriched with Ni, Nb, Ti and depleted with Cr.

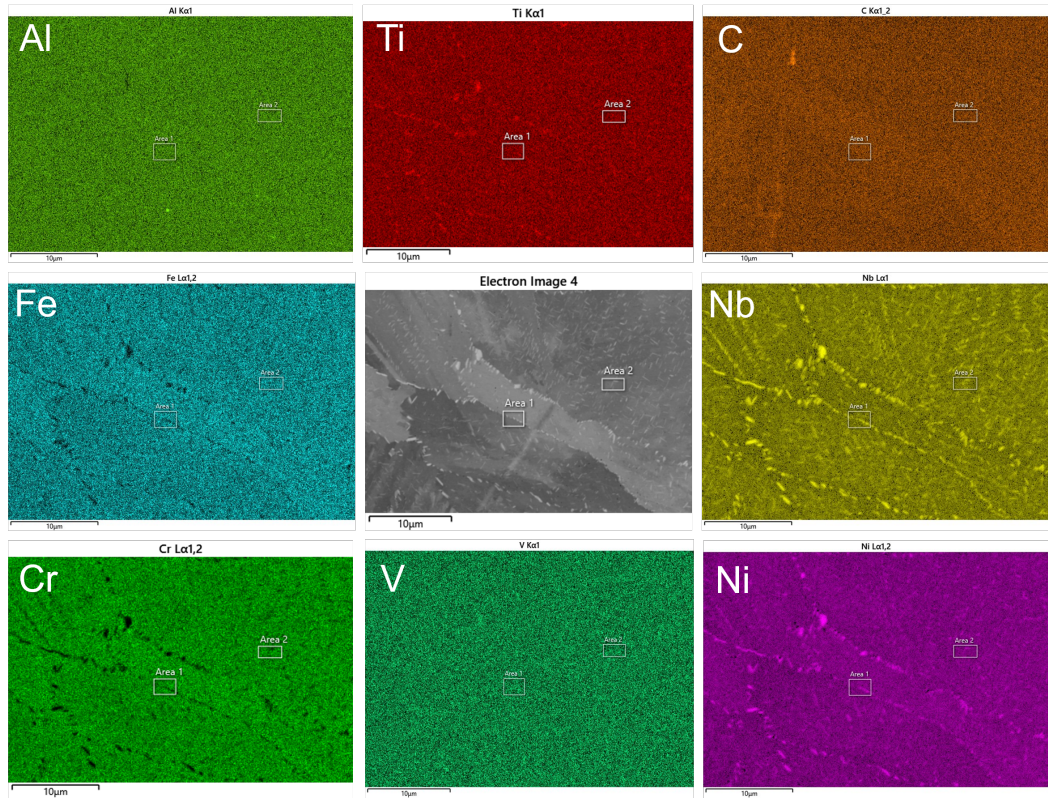


Figure 4.2: Elemental analysis of AM_LSP using EDS-SEM

4.2.1 Summary

IN718 is a precipitation-strengthened nickel-based superalloy with γ'' as the main phase contributing to its excellent high-temperature strength [124]. δ precipitates derived from metastable γ'' can be detrimental to the overall mechanical properties of the alloy [125]. The highest level of δ precipitation is commonly found to form at 900°C [125] and the presence of these precipitates can degrade the material performance, being shown to trigger intergranular cracking. Given the heat treatment profile used, δ phase is expected to develop in the grains and the grain boundaries itself, as shown in the EDS result. The volume fraction and aspect ratio of these precipitates is crucial to determine the load-bearing effect on the material [127]. As discussed in the literature review section, the ratio between intragranular (spherical) and intergranular (needle-like) precipitates could be a critical parameter in optimizing the mechanical properties at elevated temperature of AM IN718 [125]. Due to the limitation in the scope of the work, the volume fraction and aspect ratio of the precipitates were not investigated.

4.3 Effect of LSP on grain size

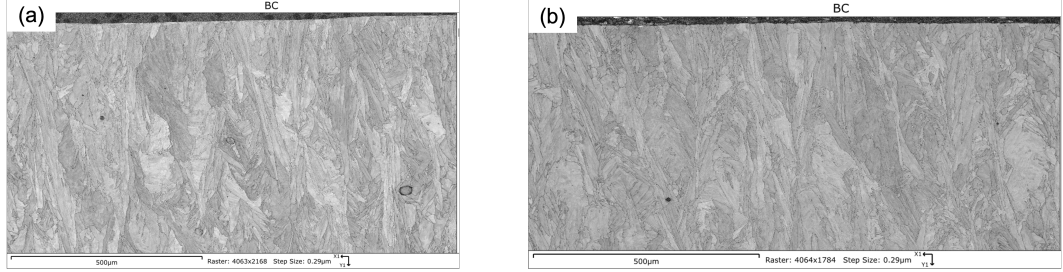


Figure 4.3: SEM image of (a) pristine AM and (b) AM_LSP IN718

SEM images of the surface of pristine AM and AM_LSP samples are shown in Figure 4.3. Both specimens exhibited columnar grains and showed no significant difference between them. Table 4.2 shows the calculated grain size of AM and AM_LSP specimen using the mean line intercept method. The average grain size of pristine AM and AM_LSP was measured to be around $29.77 \pm 12.24 \mu\text{m}$ and $32.52 \pm 11.34\mu\text{m}$ respectively.

Figure 4.4 illustrates equivalent circle diameter distribution of AM_LSP. It displays a bimodal distribution that is skewed to the left with grain size ranging from $3.57 \mu\text{m}$ to $129 \mu\text{m}$. The grain size has an average major axis of $17.9 \mu\text{m}$ and an average minor axis of $8.88 \mu\text{m}$, indicating that it is elongated in nature. As we have discussed in the previous section, LSP does not alter the grain structure of the specimen and the only valid reason these grains are elongated in nature is due to the way in which these specimens were manufactured. The rapid heating and cooling effect of the PBF process gives rise to this observation where elongated grains were promoted [27].

Evidently, the use of LSP did not introduce any grain refinement in the near surface region for AM IN718. It would be expected that shock waves generated in wrought and AM IN718 samples would attenuate similarly and produce the same effect on the grain size.

Table 4.2: Grain size estimation of pristine AM and AM_LSP specimen using the mean line intercept method

| | Average | Standard Deviation |
|--------|---------------------|---------------------|
| AM | $29.77 \mu\text{m}$ | $12.24 \mu\text{m}$ |
| AM_LSP | $32.52\mu\text{m}$ | $11.34\mu\text{m}$ |

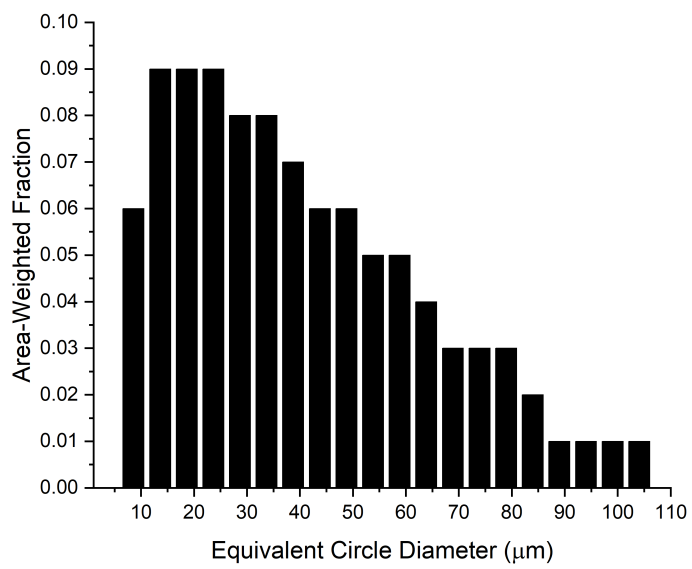


Figure 4.4: Cumulative area-weighted fraction of AM_LSP equivalent circle diameter

4.4 Cold work

4.4.1 Vicker's hardness result

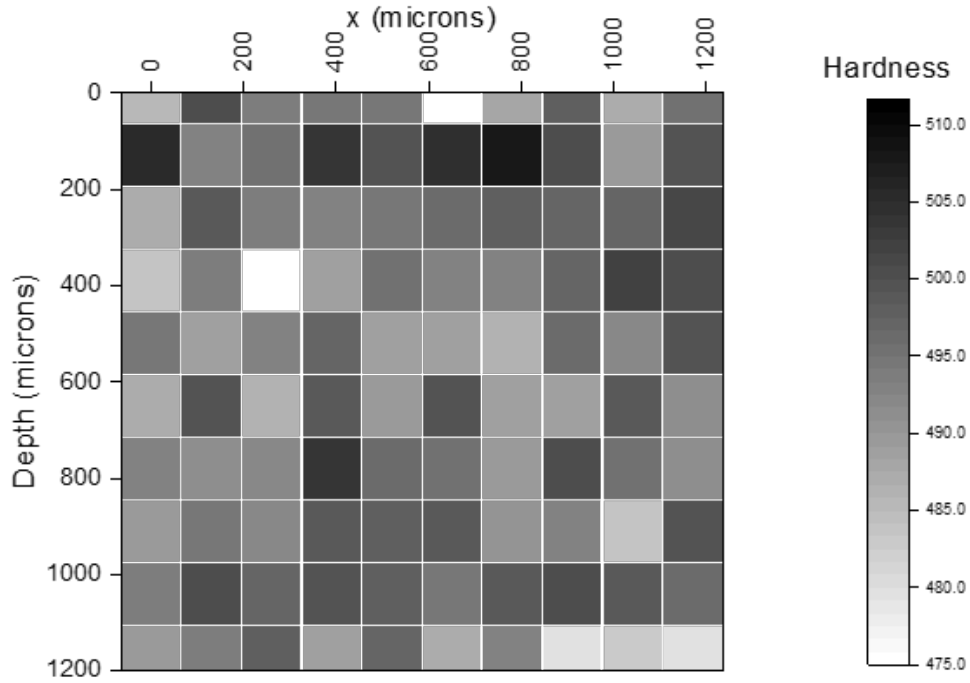


Figure 4.5: 2D heatmap of hardness value of a cross-sectional area of AM_LSP specimen

A heat map of the hardness of AM_LSP samples is illustrated in Figure 4.5. It ranged between $475 \pm 1 HV/0.5$ to $510 \pm 1 HV/0.5$ and were relatively homogeneous in the area that was tested. On the surface of the AM_LSP specimens (top layer) where the LSP effect is the most prominent, hardness value across the horizontal direction were at an average of $496 \pm 1 HV/0.5$. Similarly, the hardness value across the horizontal direction at $1200 \mu\text{m}$ deep was at an average of $488 \pm 1 HV/0.5$. There is no significant difference between the peened area from the bulk of the specimen. A low degree of cold work helps to stabilise its high-temperature fatigue performance [181], an important characteristic needed for aerospace applications [182].

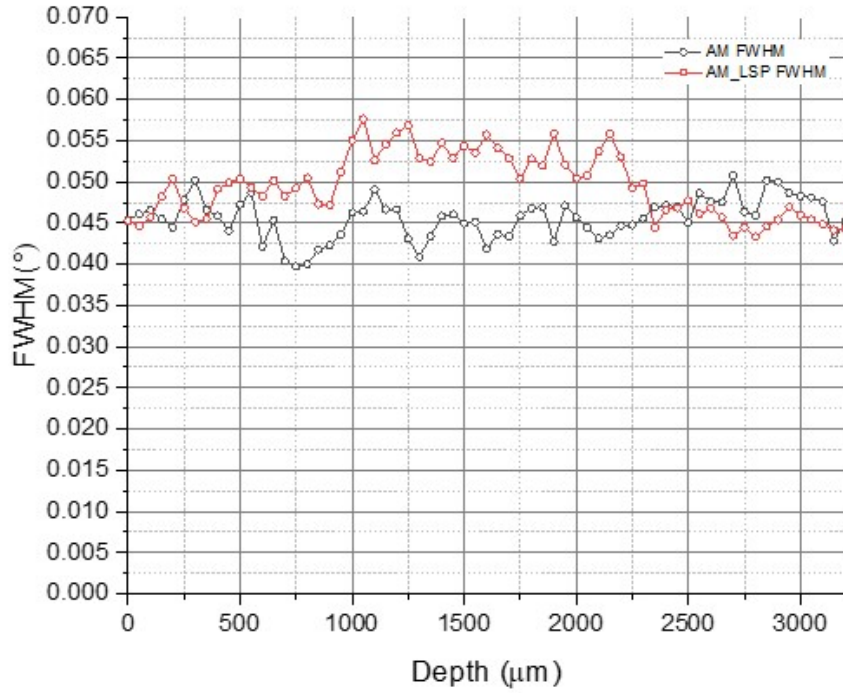


Figure 4.6: FWHM data of both pristine AM and AM.LSP specimen across the entire thickness

4.4.2 FWHM data from SXRD

FWHM values from the Bragg diffraction $\{311\}$ peaks were used to measure the relative dislocation density or cold work induced by the LSP process. It can be seen from Figure 4.6 that the FWHM value of AM_LSP has a similar profile to the pristine AM specimen on the surface level and is in agreement with the work done using the Vickers hardness technique. The sinusoidal shape of the curve were also observed in other AM Inconel alloys. It was postulate that due to the nature of the grain size of the material that was built during the AM process, it causes the FWHM value to fluctuate as the grains were not coherent. In the SEM images, grains were columnar in every depth of the material and FWHM is largely affected by grain size. Also, the FWHM has a nearly constant value of $0.0450^\circ \pm 0.0003$ on the surface level, which indicates that the LSP process induced little or no cold work. This will be further discussed in the next section with the available data of the EBSD maps.

The AM.LSP FWHM profile see a jump in the middle region after $700 \mu\text{m}$

deep, where the balancing tensile stress is present coincidentally. From a microstructural point of view, the increase in FWHM may indicate that the dual side LSP process induces an extreme increase in dislocation density in the region where the shock waves move deeper into the material. Vashista and Paul [183] observed a nonlinear correlation between FWHM and residual stress generated by grinding AISI 1060 carbon steel. The study concluded that other surface integrity factors such as the presence of tensile stress, an increase in grain size, or other microstructural factors could affect the FWHM measurements. Therefore, further studies are recommended to investigate this phenomenon.

4.4.3 Mapping and measuring plastic deformation using EBSD

Twinning is a common sight in FCC metals and alloys with low stacking fault energy when plastic deformation is exerted onto the material. The presence of twins allows the material to restructure its grain boundaries and improve its material properties [184, 185]. EBSD is one of those techniques that is sensitive to the collective effects of dislocations such as twinning[186] or low angle misorientation[187].

Despite its advantages, EBSD technique can still face difficulties detecting dislocation boundaries with very low misorientation angles with potentially very narrow spacing. It is restricted by its operational capabilities of having limited spatial and angular resolution, leading the detection of boundaries with misorientations angles below 2° [188, 189]. Kamaya et al. [189] used deformed Type 316 stainless steel specimens as a control specimen to measure the efficiency of EBSD technique between 11 different organisations. Specimens were induced with plastic strain between 0.25% to 10.28% and was found that EBSD could detect the plastic strain of accuracy up to 0.5% with the application of the smoothing filter on the background noise.

Laine et al. [190] conducted a detail analysis of Ti-6Al-4V processed by metallic shot peening and laser shock peening using both EBSD and TEM techniques. The study pointed out that LSP induced limited nanoscale deformation twinning in the first $10\mu\text{m}$ of Ti-6Al-4V despite the high strain rate LSP produces and was supported by the other authors who used high speed shot peening ballistic testing [191].

The Kernel Average Misorientation (KAM) map of the cross sectional surface of pristine AM and AM_LSP is shown in Figure 4.7. KAM is used to represent the average misorientation between a given point and its nearest neighbours which belongs to the same grain. The analysis helps to understand local lattice distortion and could suggest stored strain energy in the grain. In this analysis, 5° KAM was

the cut-off point and labelled with a rainbow scale; where blue and red represent the minimum and maximum misorientation ($0-5^\circ$), respectively. The examined area displays a low KAM value (blue) in the pristine AM matrix with a small amount of the misorientation mainly found on the grain boundaries. AM IN718 that has undergone appropriate heat treatment process tend to release the high dislocation density resulting in a significant decrease of misorientation. It is not the interest of this EngD to discuss the effect of heat treatment on the KAM value in AM IN718 specimens. Interested reader may refer to the various journal papers[192, 109]. On the other hand, AM_LSP specimens show a general increase in the dislocations all around the matrix, signifying the presence of deformation generated by the LSP process [187]. Meyers et al. [109] studied shock deformed nickel and concluded that plastic deformation in the case shock waves is the result of dislocations generation at the rapidly moving shock front. In a process like LSP where time scales interaction between the laser pulse and the targeted material are short, dislocation generation, not dislocation motion, is responsible for deformation. These dislocations are responsible for introducing the misorientations in the material which is reflected in the KAM analysis.

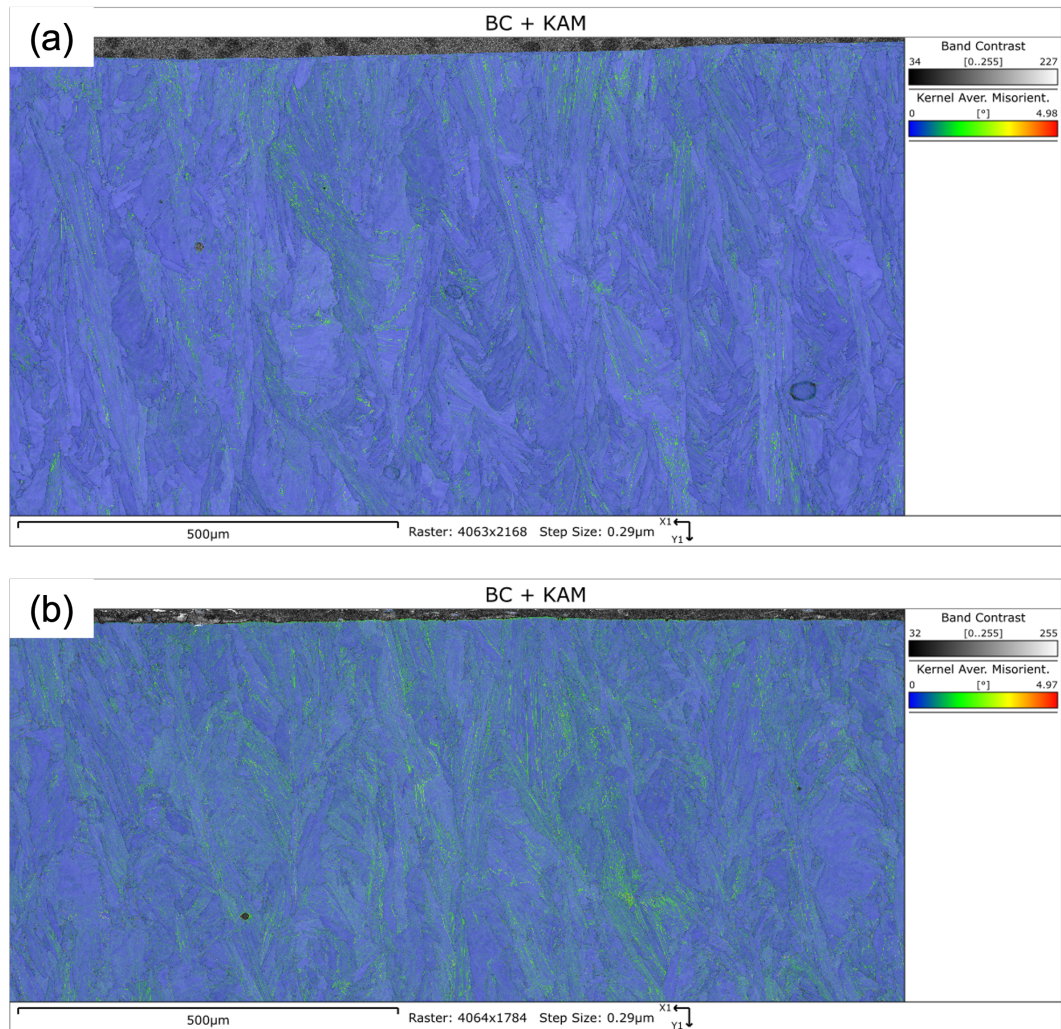


Figure 4.7: KAM of the cross sectional surface of (a) pristine AM and (b) AM_{LSP}

4.4.4 Analysis and summary

The current LSP process on AM IN718 specimen bring minimum cold work where it could be identified with EBSD maps. There was no grain size refinement found and FWHM profile was similar to its pristine state. The EBSD maps show signs of dislocations in the microstructure due to the LSP process. Gill et al. [193] also reported that no grain refinement was found in wrought IN718 that undergone the a different kind of LSP process defined as LSP without coating (LSPwC) process where no protective layer was applied on the material surface. The LSP condition used in Gill's research was in the range of 3 - 8 GW/cm^2 , which is close to the processing condition used in this thesis. Gill et al. hypothesised that it was the high temperature and pressure brought by the plasma generation that caused the grain structure to remain as it was. The absence of the black tape in Gill's experiment may have led to plasma transmitting thermal energy onto the surface of the specimen, diffusing the initial dislocation that was generated by the LSP. At this point, the discrepancy seen in this experiment as compared to the conventional LSP process is not known as there were no temperature data taken during the LSP process itself.

4.5 Residual stress measurements due to LSP

The through-thickness stress measurements of AM and AM.LSP are illustrated in Figure 4.8. Stress values were derived from Equation 3.5 where the strain data was collected from the SXRD experiment. Calculated fit uncertainties were insignificant and are thus not shown in the rest of the plotted Figures. For the baseline AM samples, not subjected to LSP, the overall level of residual stress is low and globally consistent across the sample thickness. A small difference is observed between in-plane and out-of-plane stress which is likely to arise due to the assumption of a single reference q_0 value for all data. AM.LSP stresses became less compressive along the depth but its effect could still reach up to $-650 \pm 25 \mu\text{m}$ from the surface. The highest compressive residual stress of AM LSP is observed at the surface with a value of -606 MPa . LSP treated materials undergo high strain rates up to $10^6/\text{s}$ [194] and have been shown to provide deep compressive stress of up to 1 mm in depth [195]. The sum of forces must be equal to zero as no external forces are present in the samples. The balancing tensile stresses are found between the depth region of $650 \pm 25 \mu\text{m}$ to $2650 \pm 25 \mu\text{m}$ and could go up to $+427 \text{ MPa}$. Wagner [196] reported that high-cycle fatigue cracks often nucleate in the subsurface level of where the balancing tensile stress resides. This detrimental effect can reduce the overall effect of the surface enhancement process, making the enhanced material

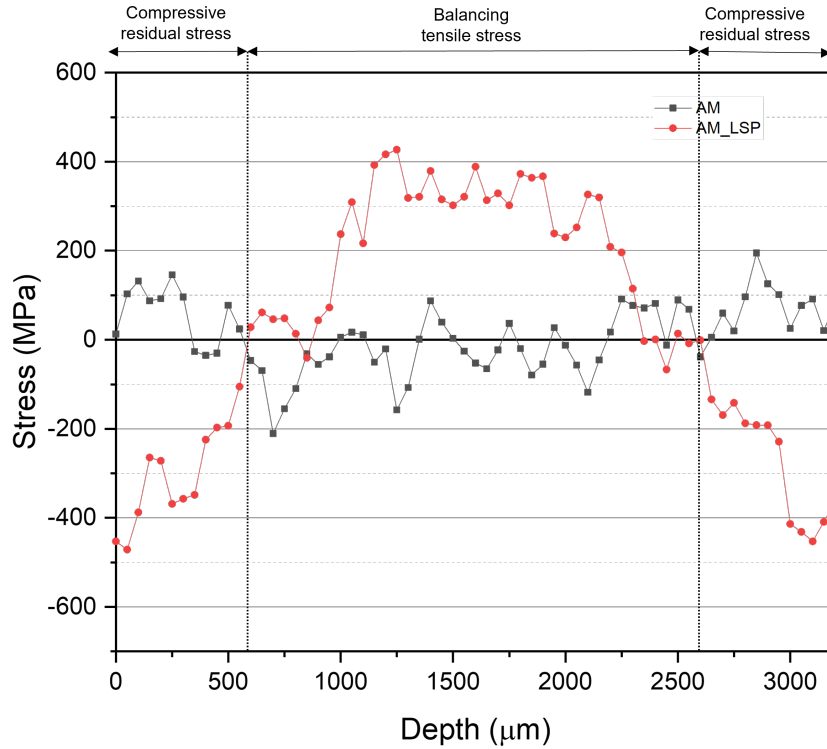


Figure 4.8: Through thickness stress measurement of AM and AM_LSP specimens

weaker than its pristine state. More observations and discussions will be made on the bending fatigue and fractography experiments with regards to the observations made about the residual stress present in the material.

4.6 Residual stress relaxation

4.6.1 Residual stress with thermal load

The through-thickness stress measurements of AM_LSP, AM_LSP exposed for 1 hour at 550°C (AM_LSP_1h) and AM_LSP exposed to 15 hours at 550°C (AM_LSP_15h) are illustrated in Figure 4.9. AM_LSP_1h shows no signs of stress relaxation on both sides of the specimen at the compressive stress region (circled in grey). On the other hand, the compressive region on both sides of AM_LSP_15h reduces from the initial $650 \pm 25 \mu\text{m}$ from the surface to $425 \pm 25 \mu\text{m}$. Interestingly, both samples show a significant decrease in the tensile stress region and a slight shift of the profile towards the right of the sample. This could be due to an experimental setup where one side of the specimen is closer to the heating coil, causing the stress

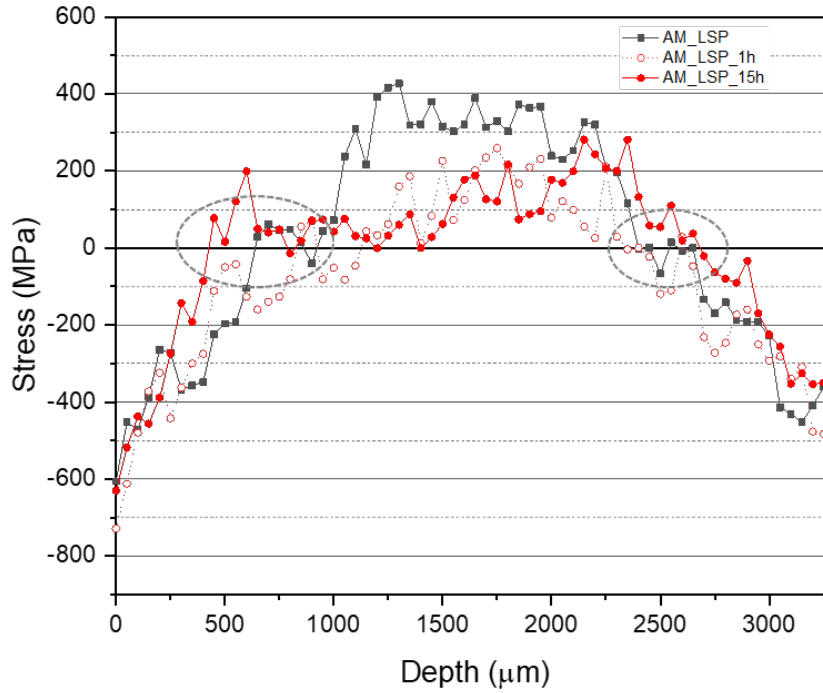


Figure 4.9: Through thickness residual stress measurement of AM_LSP specimen in a 550°C setting for 1 hour and 15 hours respectively

relaxation to be more notable. Zhou et al. [197] reported that the simulation work on residual stress relaxation for LSP IN718 reveals that nearly no relaxation occurred at temperatures lower than 700°C, which aligns with the result obtained in this project. Stress relaxation is more significant and increases with temperature and time. When exposure time increases to 15 hours, the stress relaxation was more obvious in AM_LSP_15h as dislocations try to recover and reduce the misfit between the bulk and deformed layer [198]. Rate of relaxation were found to depend primarily on the degree of cold working [175, 148, 199] and in the previous experiments, minimal cold work was found on the surface.

4.6.2 Residual stress with mechanical load

The through-thickness stress measurements of AM_LSP, AM_LSP expose to mechanical loading of 30% yield strength to 10,000 cycles at room temperature (AM_LSP_10k.RTP) and AM_LSP expose to mechanical loading of 30% yield strength to 1,000,000 cycles at room temperature (AM_LSP_1m.RTP) are illustrated in Figure 4.10. The

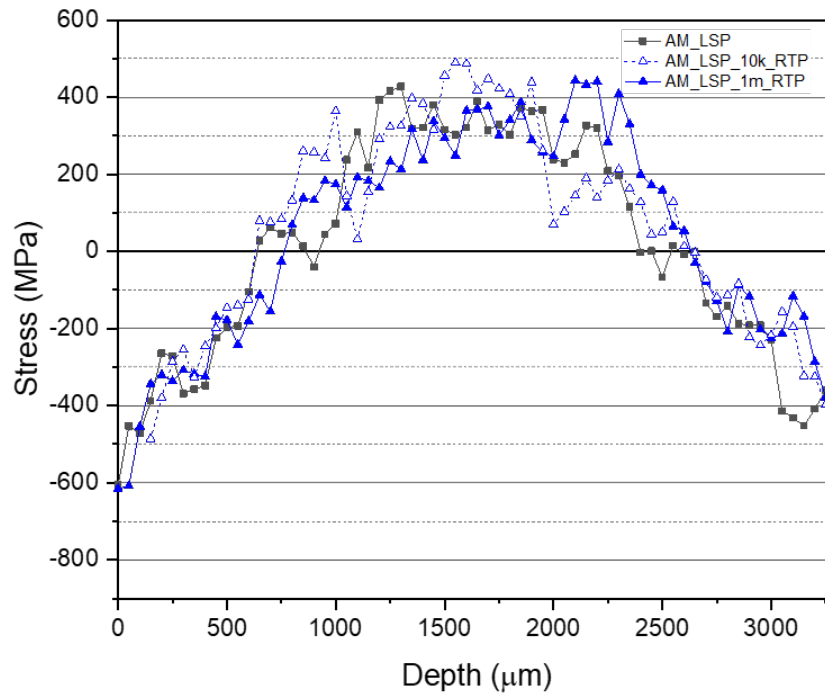


Figure 4.10: Through thickness residual stress measurement of AM_LSP specimen under cyclic loading in a room temperature setting

compressive and tensile regions stayed very much alike across all LSP conditions. Relaxation due to cyclic loading is mainly dependent on these five factors: (1) initial magnitude of the compressive stress, (2) gradient of the stress field, (3) amount of cold work generated, (4) stress amplitude applied onto the specimen and (5) material cyclic stress-strain response [200]. In the literature, stress relaxation on LSP IN718 due to cyclic loading is mainly determined by the amount of cold work introduced into the specimen [201, 202, 200] and studies regarding the other four factors are limited. Thus, it is prudent to attribute most of the mechanical relaxation to the amount of cold work generated by the LSP process. Furthermore, stress relaxation with the greatest reduction in residual stress values were observed in the first cycle [201, 203]. In this particular case, stress relaxation were kept to the minimum as minimal cold work has been observed on the specimen through previous experiments.

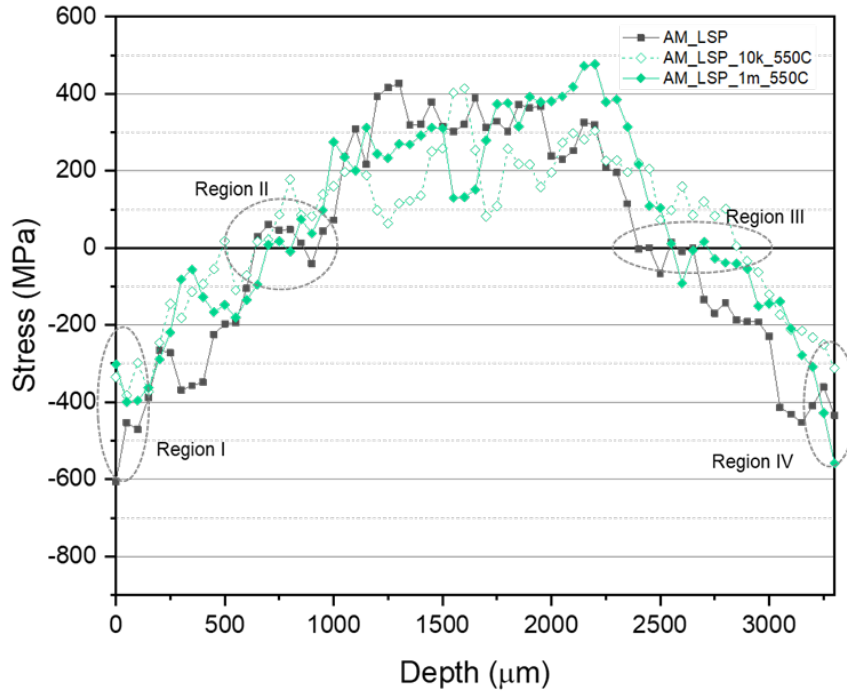


Figure 4.11: Through thickness residual stress measurements under cyclic loading in a 550°C setting

4.6.3 Stress relaxation due to thermomechanical load

The through-thickness stress measurements of AM_LSP, AM_LSP exposed to thermomechanical loading of 30% yield strength to 10,000 cycles at (AM_LSP_10k.550C) at 550°C and AM_LSP expose to mechanical loading of 30% yield strength to 1,000,000 cycles at 550°C (AM_LSP_1m.550C) are illustrated in Figure 4.11. Surface stress decreases from -606 MPa to -334 MPa and -301 MPa (Region I), respectively. The compressive stress region on the left side (Region II) is largely unaffected and remains at 650 μm below the surface. However, the compression region on the opposite side of the specimen (Region III) was reduced to $450 \pm 25 \mu\text{m}$ for AM_LSP_10k.550C and $600 \pm 25 \mu\text{m}$ for AM_LSP_1m.550C respectively below the surface. Interestingly, the compressive region for AM_LSP_10k.550C has reduced more than the AM_LSP_1m.550C. Literature has shown that specimens that undergo more cyclic loading lead to an increase of dislocation densities and it is refer to mechanical annealing [204, 205]. Mobile dislocations rearrange itself, causing them to multiply and interact with other dislocations during the cyclic process

however at the expense of change in shape or dimension.

In the pure mechanical loading test, there were no significant differences between the two conditions. When exposed to a heated environment, AM_LSP_1m_550C were able to contain the residual stress better than AM_LSP_10k_550C. The surface stress on the opposite side of the specimen (Region IV) for AM_LSP_1m_550C (-558 MPa) was much higher than AM_LSP_10k_550C (-312 MPa). This phenomenon was also observed in the pure thermal load environment where both AM_LSP_1h and AM_LSP_15h show a slight shift of the residual stress profile to the right.

In this particular setting, the thermal exposure of the specimen has caused the dislocations to be more mobile and with the effect of mechanical annealing, the residual stress of AM_LSP_1m_550C see a shift to the right due to one side of the specimen closer to the heating coil of the oven and able to hold on to residual stress better than AM_LSP_10k_550C respectively.

4.6.4 Summary

The results of these three different testing conditions highlighted the effects of LSP on AM IN718 specimens. When the AM_LSP specimens were subjected to pure mechanical loading at room temperature, AM_LSP_1m_RTP can retain the beneficial compressive stress up to a million cycles at 30% yield strength loading condition. This is a vital observation as it gives aeroengine manufacturers confidence that LSP AM IN718 is a viable material for structural parts. Likewise, specimens that were exposed to thermal loading showed promising results. Surface compressive stress remains largely unaffected but when it's exposed to a longer heating time i.e. 15 hours, the compressive region decreases from the initial $650 \pm 25 \mu\text{m}$ from the surface to $425 \pm 25 \mu\text{m}$, as seen in Figure 4.9. On the other hand, specimens that was tested in a thermomechanical environment only saw a 50% decrease on both the surface stress and compressive region. Finally, it is worthwhile to point out that LSP brought very little cold work onto AM IN718 samples which is a contributing factor on the performance of these mechanical test.

4.7 Uniaxial tensile stress

Wrought specimens (W) were used to do a benchmark of AM static performance and the values were taken from various literature papers. These also act as a control of the effectiveness of the LSP process. In general, AM is slightly stronger than W with an ultimate tensile strength of $1592 \pm 31 \text{ MPa}$ compared to $1493 \pm 8 \text{ MPa}$. Also, the YS of AM samples were 23% higher than W despite having similar UTS, as

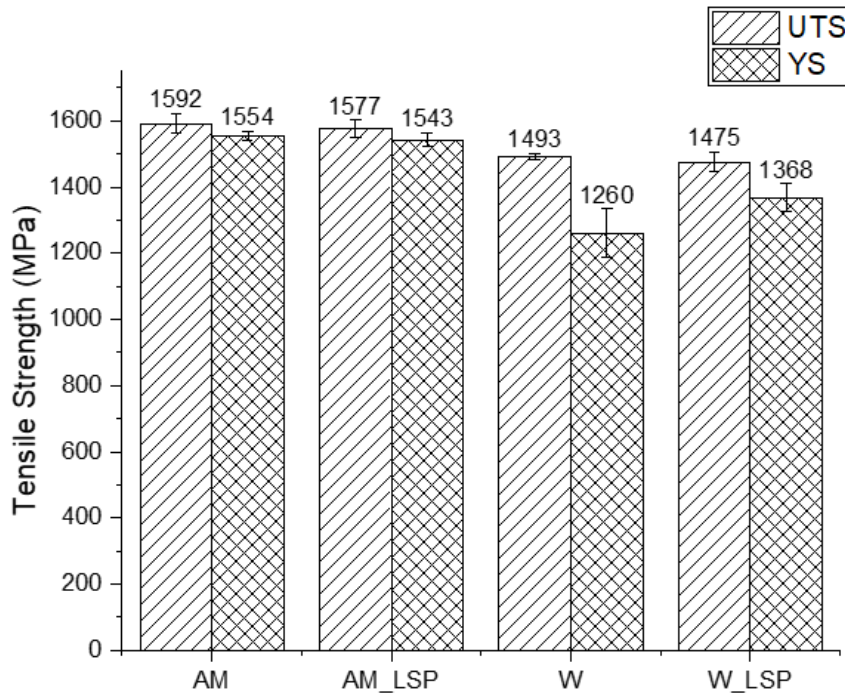


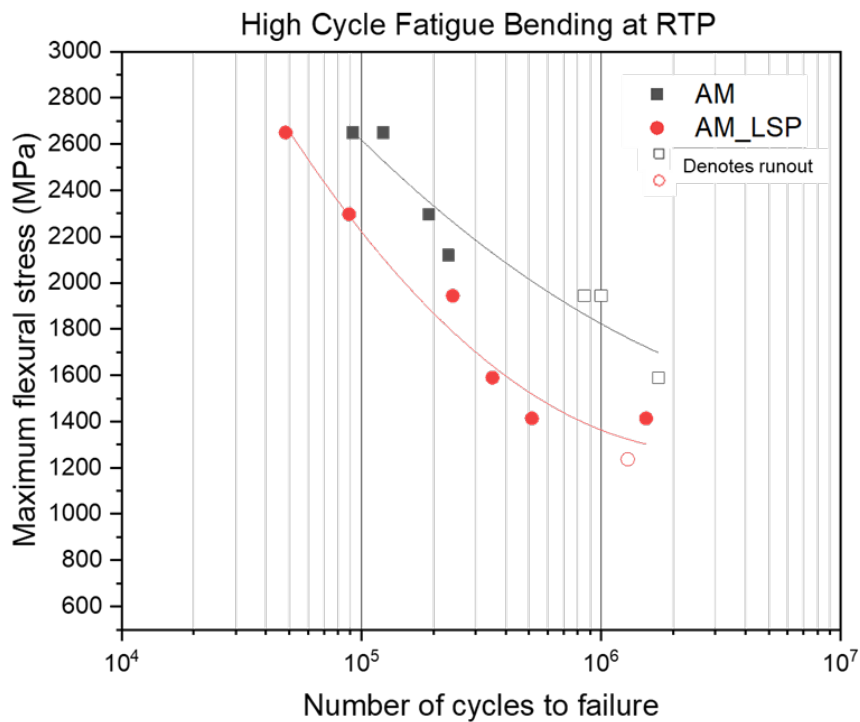
Figure 4.12: Comparison of tensile strength of pristine AM, AM.LSP, Wrought and LSP Wrought specimens

shown in Figure 4.12. This is mainly attributed to the generation of small grain size diameter and minimum alloying element segregation of the AM material [206, 207], resulting in an increase in strength. AM.LSP was found to have a yield strength of 1543 ± 21 MPa, which is approximately equal to its pristine state which has a yield strength of 1592 ± 30 MPa. Similarly, the introduction of LSP has little or no effect on the tensile properties of the W specimens and this was also verified on other materials in the literature [208]. Pavlina and Van Tyne [209] correlate hardness with YS and UTS, which have been crucial to the scientific community. The team have established a linear correlation with the hardness over the entire range of strength values for steels and this finding have been extended to other metal alloys as well [210, 211, 212]. In the previous section, the hardness value of AM.LSP specimens remained relatively constant thus the strength of the specimens see no change in their YS and UTS.

4.8 Bending fatigue

Cyclic three point bend testing was performed to evaluate the fatigue performance of the alloys before and after LSP in both room temperature and heated environment. This section is divided into two parts to individually analyse the effect of LSP on the two different environments.

4.8.1 Room temperature bending fatigue



This is an interesting phenomenon because many prior research works had found that LSP treatment increases the fatigue life of the treated material, and a lot of literature also agrees with this view [154, 213, 214, 195, 215]. The lacklustre fatigue performance in AM.LSP has three possible causes. Firstly, the increase in surface roughness from 0.3 μm Ra to 1.5 μm Ra have caused the material to deteriorate in performance. When materials with rougher surface go through cyclic loading, it creates unnecessary local stress concentration and trigger fatigue crack initiation. Numerous studies highlighted the influence of higher surface roughness as the cause for the premature fatigue failure of PBF parts for IN718 material [216, 217] and other metal alloys [218, 219]. Secondly, the residual stress state on the entire specimen is currently unverified due to the time restriction on the synchrotron beam line. Therefore, it is possible that there are regions where tensile stress is present on the surface that promotes crack propagation, further weakening the specimen. Lastly, the presence of balancing tensile stress in the middle region of the specimen coincides with the δ precipitates in the grain boundaries which accelerate the crack initiation [179]. Fractography analysis will be able to determine the location of crack initiation sites, which is discussed in the next section.

Fractography

Fractography images of AM and AM.LSP specimens are shown in Figures 4.14-4.17. As seen in Figure 4.15a, AM specimens showed crack initiation from the near-surface region, in particular on the corner of the cross-sectional area. The crack propagates towards the bulk region (Figure 4.15b) and striations were also found on the surface (Figure 4.15c). Upon closer examination, there were also signs of ductile overload at the final fracture area (Figure 4.15d) . Similar fracture surfaces are observed in AM.LSP specimens (Figure 4.16 and Figure 4.17) [192]. Comparable fractography characteristics were also seen in the specimen despite having a lower bending fatigue strength. Crack initiation also starts at the corner and propagates towards the bulk region. In Figure 4.15b, AM.LSP final fracture region seems to be rougher than AM and it was the case for the other six fractured specimens also. The introduction of LSP have caused a rougher surface on the peened specimens as seen in Table 4.1, causing it to fail earlier than the pristine AM condition.

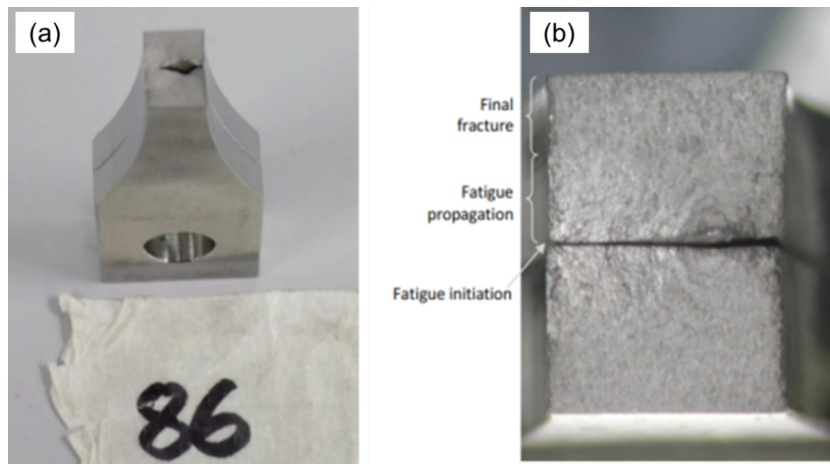


Figure 4.14: Picture of (a) fractured pristine AM specimen and (b) closeup photograph of fractured surface

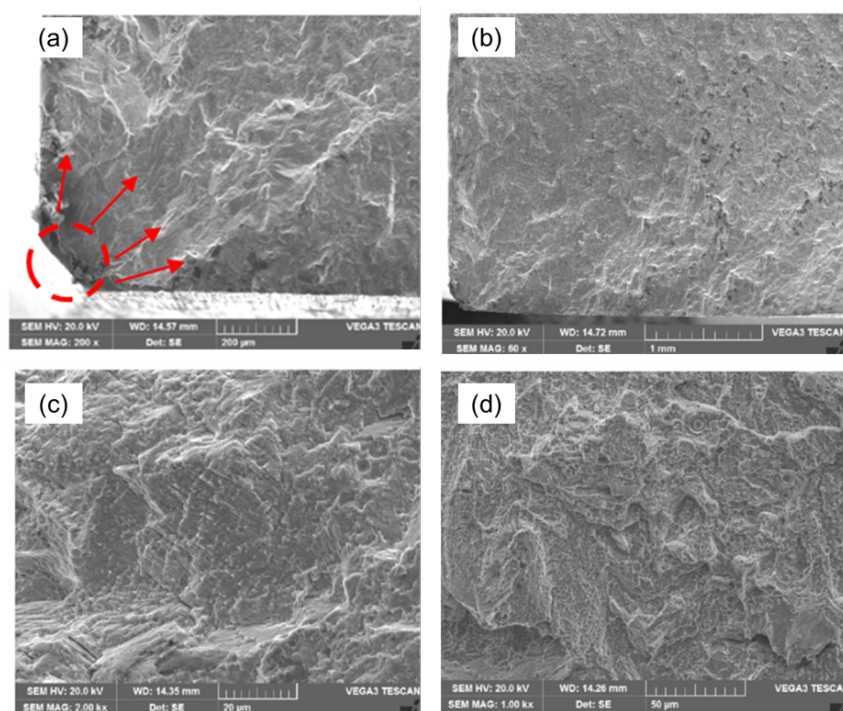


Figure 4.15: SEM image of pristine AM (a) crack initiation point, (b) fatigue propagation area, (c) high magnification showing striation marks and (d) high magnification showing dimple feature

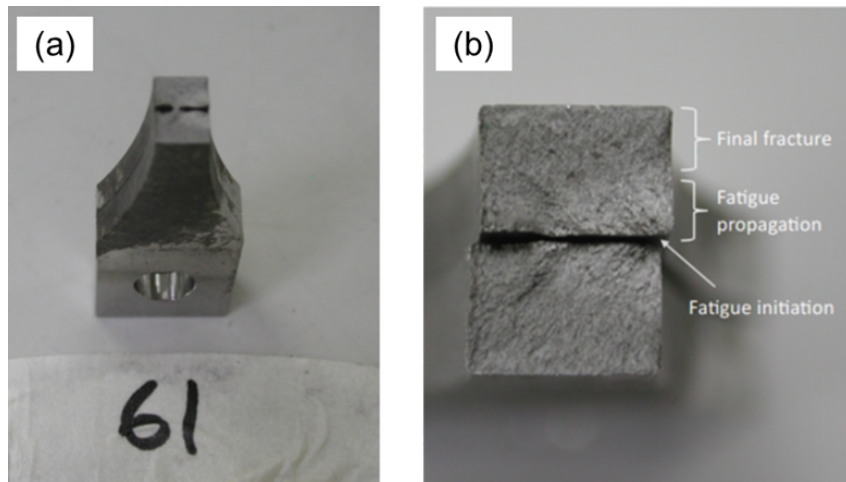


Figure 4.16: Picture of (a) fractured AM.LSP specimen and (b) closeup photograph of fractured surface

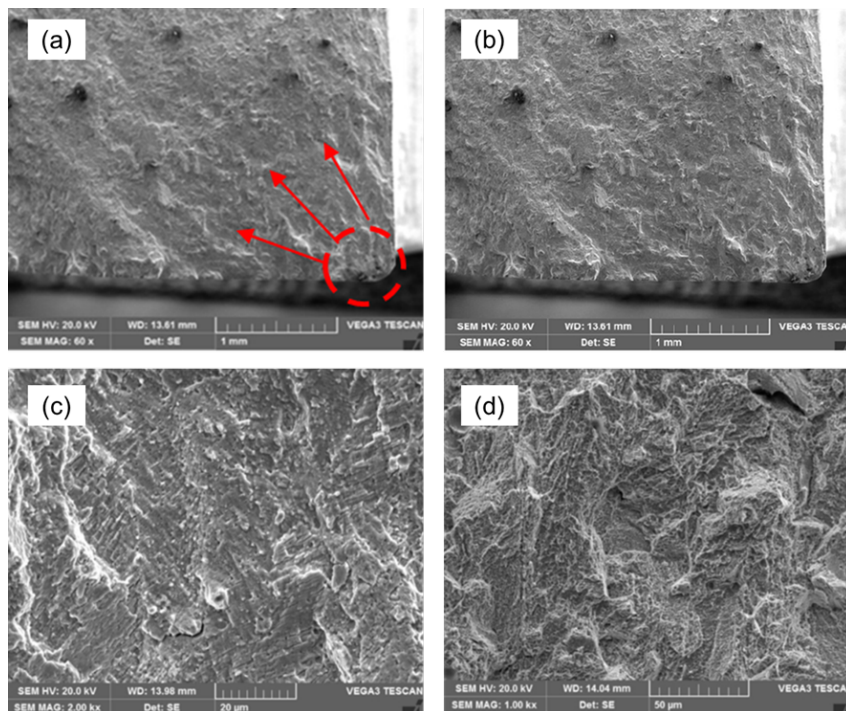


Figure 4.17: SEM image of AM.LSP (a) crack initiation point, (b) fatigue propagation area, (c) high magnification showing striation marks and (d) high magnification showing dimple feature

4.8.2 550°C bending fatigue

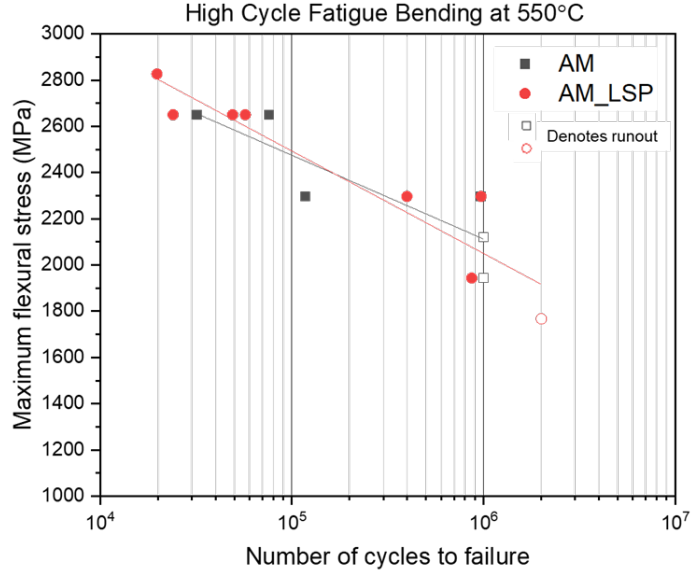


Figure 4.18: S-N curve of bending flexure test under 550°C setting

Figure 4.18 shows the $S - N$ curves for both alloys when exposed to 550°C. The $S - N$ curve for the peened coupons (AM_LSP) performed comparable as the unpeened coupons (AM). At stress level of 2650 MPa, AM fails at 32,898 cycles, whereas AM_LSP fails at 44,292 cycles, achieving a slightly better result. Bending fatigue strength above 10^6 cycles for AM and AM_LSP are 2112 ± 181 MPa and 2049 ± 174 MPa respectively. Given the wide confidence interval that $S - N$ curve typically has, it is reasonable to conclude that both alloys are behaving in the same way in a heated environment.

Fractography

Fractography images of AM and AM_LSP specimens that were exposed to 550°C are shown in Figures 4.19-4.22. As seen in Figure 4.19a, AM specimens showed crack initiation from the near-surface region. Crack propagates towards the bulk region (Figure 4.19b) and striations were also found on the surface (Figure 4.19c). Similar fracture surfaces were observed in AM_LSP specimens (Figure 4.21 and Figure 4.22). Crack initiation starts at the corner and propagates towards the bulk region. One notable difference was that the fatigue propagation (Figure 4.21b) was much larger than the pristine AM sample (Figure 4.18b). This observation is in line with the

bending fatigue result where AM_LSP saw a great jump in performance when it is placed in a heated environment.

The larger area showed that LSP was effective in delaying the final fracture point [220]. However, crack propagation speed is a better predictor feature in predicting the effect of LSP on overall fatigue life improvement [221, 222]. LSP-induced compressive residual stress have been shown to vastly increases initiation time, but this also depends on the applied stress range. The higher the applied stress range, the less effective LSP-induced compressive residual stress are at delaying crack initiation. In addition, the LSP-induced residual stress field and depth profile, as well as the shape and depth of defects appear to be important variables influencing fatigue crack initiation mechanisms and thus changes in fatigue regime [220].

Further work is required to accurately the entire crack cycle especially the crack propagation data such as short crack shape, growth rate and stress intensity factor range. One option is to use X-ray tomography in combination with other characterisation techniques such as SEM has been shown to produce high resolution data of fatigue cracks and surrounding microstructure [223].

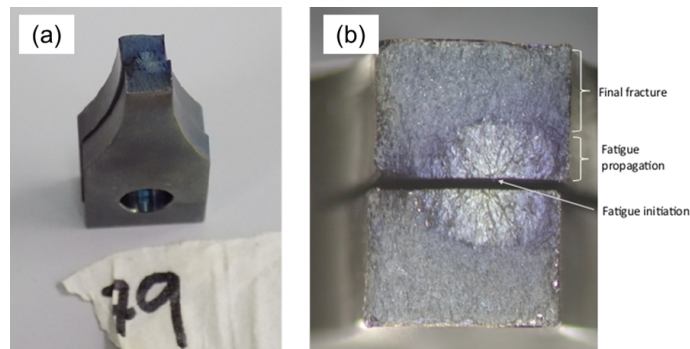


Figure 4.19: Picture of (a) fractured pristine AM specimen and (b) closeup photograph of fractured surface in 550°C setting

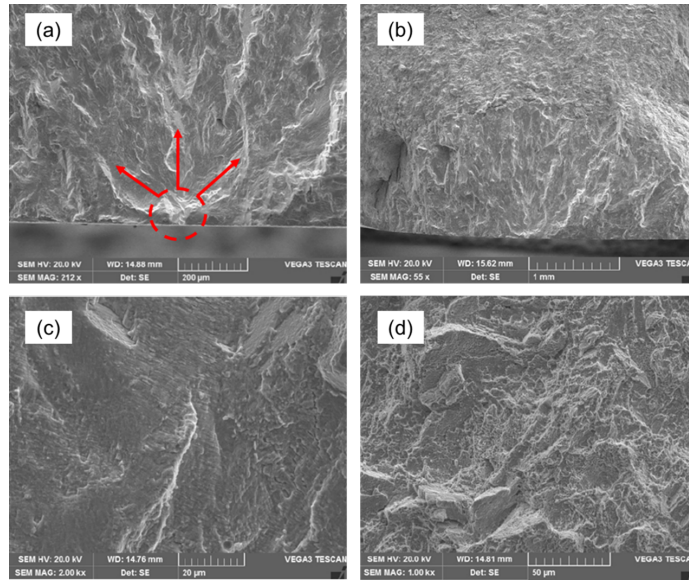


Figure 4.20: SEM image of pristine AM (a) crack initiation point, (b) fatigue propagation area, (c) high magnification showing striation marks and (d) high magnification showing dimple feature

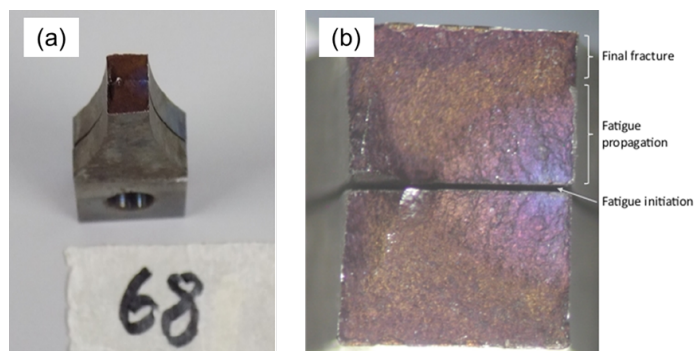


Figure 4.21: Picture of (a) fractured AM.LSP specimen and (b) closeup photograph of fractured surface in 550°C setting

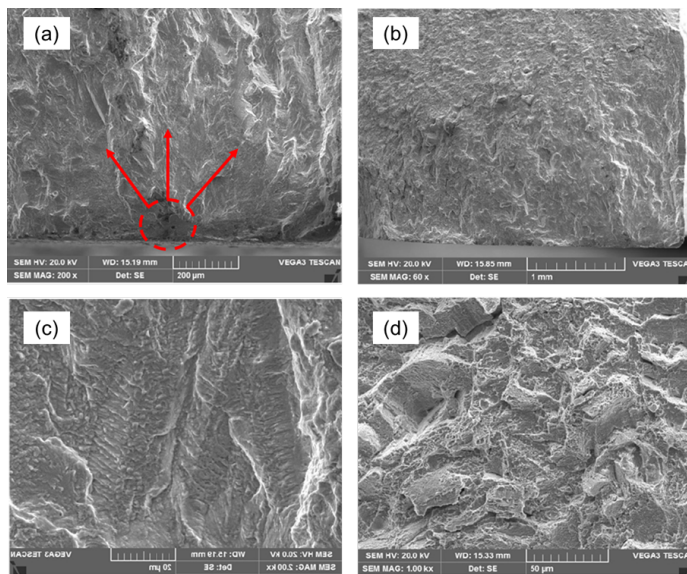


Figure 4.22: SEM image of AM_LSP (a) crack initiation point, (b) fatigue propagation area, (c) high magnification showing striation marks and (d) high magnification showing dimple feature

4.8.3 Summary

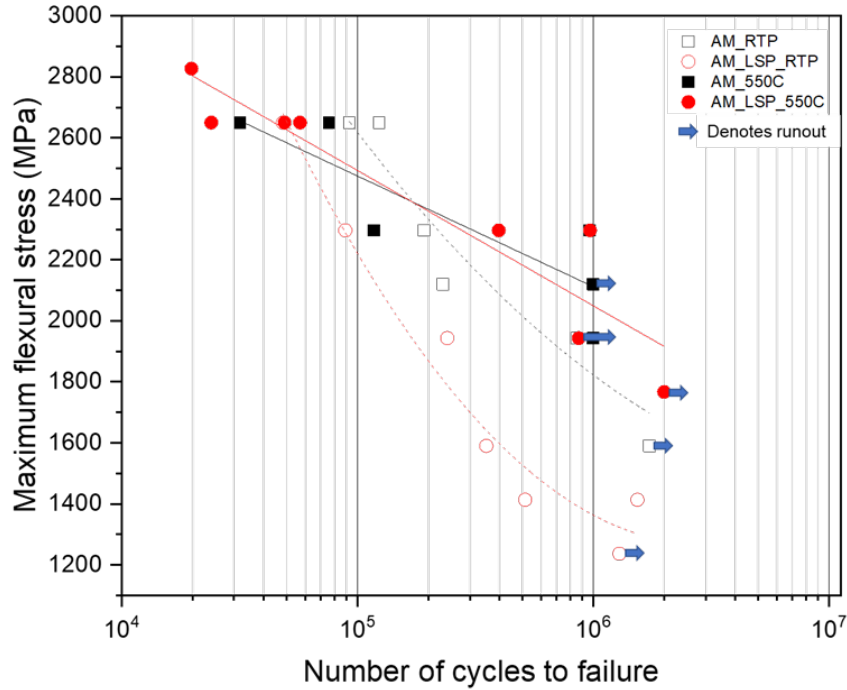


Figure 4.23: S-N curve of bending flexure test under both room temperature environment and 550°C setting

Figure 4.23 shows the performance of AM (black) and AM.LSP (red) in both room temperature (dotted line) and 550°C environment (solid line). Two significant observations can be derived from this Figure. Firstly, AM.LSP specimens performed badly compared to pristine AM specimens in the room temperature environment. It is possible that the combination of higher surface roughness and the presence of tensile stress region brought by the LSP process deteriorates the AM IN718 surface, thus showing a weaker bending fatigue resistance. It is inconclusive to postulate why the bending fatigue life of AM.LSP is significantly lower than AM specimen. For the quantification of this phenomenon, the collection of more data points and statistical analysis is recommended. Secondly, AM.LSP sees a bigger jump in performance in the heated environment as compared to the pristine AM specimen. In addition to the precipitate strengthening mechanism, the compressive stress generated by LSP was able to retain much of its beneficial effects and further delay the final fracture from initiating. The advantage of deep compressive stress is more prominent in

a high temperature environment and its effect outweighs the increase in surface roughness brought by the LSP process.

Chapter 5

Conclusion & future work

5.1 Summary and innovative contributions

This chapter summarises the performed research and lists the major conclusions arising from the obtained results. The identified innovations in each section are stated, followed by their relevance to industrial applications. Recommendations for future research are discussed to address some of the limitations faced in this research.

5.1.1 Development of laser shock peening process for additive manufactured Inconel 718 material

Summary and key findings

- An industrial grade powder bed fusion process fabricated additive manufactured Inconel 718 samples with a flat dog-bone geometry with a thickness of 3 mm. It was then subjected to laser shock peening to find out its response to the process
- A design of experiment was carried out to find out the optimal laser power density to utilise in order to get the best outcome in terms of the residual stress state (refer to publication that is listed in Appendix F). It was designated to be 7.7 GW/cm^2 as it produces a reasonable compressive stress state as compared to the other two power densities used in the optimisation

5.1.2 Effect of laser shock peening on the mechanical properties on additive manufactured Inconel 718

Summary and key findings

- A diverse set of mechanical tests were employed to investigate the effects of laser shock peened additive manufactured Inconel 718 specimens. Surface roughness, phase identification, cold work, grain size and tensile strength were recorded in this research work
- The surface roughness data obtained from contact profilometer showed an approximately 10x increase of its Ra value, reaching up to a value of $1.52 \mu\text{m}$.
- The data collected from the synchrotron X-ray diffraction experiment showed that the use of laser shock peening does not impact upon the phase composition of the material.
- Full width half maximum data extracted from the synchrotron X-ray diffraction showed that minimum cold work was introduced onto the surface of the material. However, there is an increase of full width half maximum value in the middle of the specimens, indicating that there might be dislocations present in the core region which needs to be investigated further
- Minimal cold work is observed on the surface of the material as determined through the Vicker's indentation method. A 2D heat map of the cross sectional area of LSP specimen was plotted to show that there was no significant difference in the hardness between the surface and bulk material
- Utilising EBSD data, it was concluded that minimum cold work was introduced into the material. Heat map of the kernel average misorientation values were relatively low and there was indication of dislocations being generated on the surface of additive manufactured Inconel 718 specimens
- SEM images were taken to observe the grain size difference between the pristine and processed specimens. Using the mean line intercept method, no significant differences were found on the grain size. This indicates that no grain

refinement was observed in the processed specimens

- Pristine additive manufactured Inconel 718 has an average grain size of $29.77 \pm 12.24 \mu\text{m}$ whereas laser shock peened specimen has an average grain size of $32.52 \pm 11.34 \mu\text{m}$
- Uniaxial test were used to find out the tensile strength of the specimens. AM_LSP was found to have a yield strength of $1543 \pm 21 \text{ MPa}$, which is approximately equal to its pristine state that has a yield strength of $1592 \pm 30 \text{ MPa}$. There were no significant improvements made to the material as the beneficial effects brought by the laser shock peening is more applicable in the fatigue test

Specific innovations

- The effect of laser shock peening on additive manufactured Inconel 718 is thoroughly investigated for the first time
- It was shown that laser shock peening brought an increase in surface roughness and minimal cold work into the material. No grain refinement was observed on the material and phase composition stays the same. Yield strength of AM_LSP remain unchanged

5.1.3 Residual stress relaxation of AM_LSP in various loading conditions

Summary and key findings

- Data collected from synchrotron x-ray diffraction was processed and mapped to the through thickness residual stress state of the laser shock peened specimens. Various loading conditions were tested on these materials to investigate the residual stress relaxation
- AM_LSP specimens were exposed to a thermal environment of 550°C for 1 hour and 15 hours. Residual stress relaxation was not found after 1 hour

and their stress relaxation was minimal. When the specimens were left for 15 hours, the compressive stress region decreases by 32% from 625 μm to 425 μm

- When AM_LSP specimens were put under mechanical cyclic loading at room temperature, no sign of stress relaxation was found. Stress relaxation under cyclic loading is largely dependent on the cold work introduced into the material. In the previous experiment, AM_LSP provides minimal cold work to the material and thus the stress relaxation was kept to the minimal
- In the thermomechanical environment, residual stress relaxation saw a decrease on both the surface stress and compressive region. This observation was also seen in the pure thermal environment. Therefore, based on the test result, it was reasonably assumed that residual stress relaxation is broadly determined by the temperature and time that the specimens were exposed

Specific innovations

- Residual stress relaxation for AM_LSP under mechanical cyclic loading in room temperature is very minimal. This gives great confidence for manufacturers to consider this manufacturing approach for room temperature use
- At 550°C, the specimen could still hold 50% of its initial residual stress profile after going through about a million loading cycles. This is an important data point for aeroengine manufacturers who are considering the laser shock peening approach to utilise additive manufactured Inconel 718 for high temperature applications

5.1.4 Three point flexural bending performance in both room temperature and heated environment

Summary and key findings

- Three point flexural bend test was conducted in both room temperature and 550°C environment. Seven specimens at various loading conditions were utilised to plot the $S - N$ curves

- It was shown that AM.LSP specimens performed poorly in the room temperature conditions. Fractography analysis of AM and AM.LSP condition showed that there was no major differences between their failure modes. It was hypothesized that the increase in surface roughness and the possible presence of tensile stress on other parts of the surface that was not measured in this experiment caused AM.LSP to underperform. Further investigations are required
- Laser shock peening did improve the bending fatigue performance of the specimens in a heated environment. It saw a huge increase of strength when compared to its room temperature result

Specific innovations

- The effect of laser shock peening on the structural performance of an experiment-scale additive manufactured Inconel 718 was investigated for the first time. Using three point flexure as a load case, it was shown that when the parameters were optimised, it is possible to level up the performance of laser shock peened additive manufactured Inconel 718
- The integration of laser shock peening process and additive manufactured Inconel 718 proved to be a viable manufacturing workflow for high temperature applications

5.2 Limitations of the research and recommendations for future work

The research presented in this thesis established the viability of additive manufactured Inconel 718 material for improved performance using laser shock peening. This section describes the limitations of the research as well as the opportunities to perform extensional research work in the context of this thesis.

5.2.1 Material optimisation

The current work fabricated IN718 specimens based on the standards given by the manufacturer. There are other school of thoughts in the scientific community to develop a new Inconel nickel alloy with a different chemical composition so that the printing process will generate a stronger matrix capable of handing a higher load. On the other hand, there has been extensive work done to develop new printing parameters (i.e. higher laser power or faster laser scanning speed) to lower the different cooling rates between the surface and bulk layer. Thus, it is possible to pick up a modified powder stock and enhanced processing parameters to fabricate a stronger material that could perform better than a standard additive manufactured Inconel 718 parameters.

5.2.2 Polishing specimen surface to a lower surface roughness value

The AM_LSP specimens saw a huge jump in Ra values on the surface of the specimen. Despite being in a range of 1 μm Ra, it has limited the full potential it can bring in a fatigue environment. Through extensive review, it was shown that the increase in roughness was due to the crater formed by the shots. Two remedies are proposed for the increase in surface roughness: (i) in-depth study of the LSP processing parameters and correlate it to the surface roughness values and (ii) introduce additional polishing process to lower the surface roughness to aerospace standards so that the full beneficial effects can be materialised.

5.2.3 Temperature data collection during the LSP process

The results of this project highlighted the importance of cold work that was subjected to thermal loading in a three point flexure test. It is suspected that the cold work was dissipated during the LSP process due to the thermal heat it generates. It is advisable to use temperature sensors to capture the heating process it may bring onto the surface of the material.

5.2.4 Damage analysis on fractured specimens

The analysis of the three-point flexural response in this thesis was limited to performance based metrics based on the $S - N$ curve and simple fractography analysis. Expanding the analysis to include the study of damage initiation and propagation in the specimens would provide further insights into the effect of LSP on the mechanical performance. This is possible through the implementation of in-situ as well as ex-situ inspection techniques such as acoustic emission (AE), micro-computed

tomography (CT), etc. The results generated can be correlated with the existing results in the vast body of literature related to damage mechanisms in AM IN718. Another important observation that was reinforced by the results of this work is the effect of the selected loading for the evaluation of mechanical performance. In order to completely understand the effect of LSP on flexural performance, it is recommended to test processed specimens at much higher loading temperature (up to 1000°C) and at various mechanical cyclic loading (up to 50% yield strength).

Bibliography

- [1] Joel C. Najmon, Sajjad Raeisi, and Andres Tovar. 2 - review of additive manufacturing technologies and applications in the aerospace industry. In Francis Froes and Rodney Boyer, editors, *Additive Manufacturing for the Aerospace Industry*, pages 7–31. Elsevier, 2019. ISBN 978-0-12-814062-8. doi: <https://doi.org/10.1016/B978-0-12-814062-8.00002-9>.
- [2] Paul R Gradl, Christopher S Protz, and Tal Wammen. Additive manufacturing and hot-fire testing of liquid rocket channel wall nozzles using blown powder directed energy deposition inconel 625 and jbk-75 alloys. In *AIAA Propulsion and Energy 2019 Forum*, page 4362, 2019.
- [3] M. E. Orme, M. Gschweidl, M. Ferrari, R. Vernon, I. J. Madera, R. Yancey, and F. Mouriaux. Additive manufacturing of lightweight, optimized, metallic components suitable for space flight. *Journal of Spacecraft and Rockets*, 54(5):1050–1059, 2017. doi: 10.2514/1.A33749.
- [4] 2019 annual report. Report, Rolls Royce plc, 2020.
- [5] S. N. Suci. High temperature turbine design considerations. *Aircraft Engineering and Aerospace Technology*, 42(12):10–17, 1970. ISSN 0002-2667. doi: 10.1108/eb034699.
- [6] Tobias Maconachie, Martin Leary, Bill Lozanovski, Xuezhe Zhang, Ma Qian, Omar Faruque, and Milan Brandt. Slm lattice structures: Properties, performance, applications and challenges. *Materials & Design*, 183:108137, 2019. ISSN 0264-1275. doi: <https://doi.org/10.1016/j.matdes.2019.108137>.
- [7] Y. Wen, S. Xun, M. Haoye, S. Baichuan, C. Peng, L. Xuejian, Z. Kaihong, Y. Xuan, P. Jiang, and L. Shibi. 3d printed porous ceramic scaffolds for bone tissue engineering: a review. *Biomater Sci*, 5(9):1690–1698, 2017. ISSN 2047-4830. doi: 10.1039/c7bm00315c.

- [8] Fuyao Yan, Wei Xiong, and Eric J. Faierson. Grain structure control of additively manufactured metallic materials. *Materials*, 10(11), 2017. ISSN 1996-1944. doi: 10.3390/ma10111260.
- [9] Jacob Smith, Wei Xiong, Wentao Yan, Stephen Lin, Puikei Cheng, Orion L. Kafka, Gregory J. Wagner, Jian Cao, and Wing Kam Liu. Linking process, structure, property, and performance for metal-based additive manufacturing: computational approaches with experimental support. *Computational Mechanics*, 57(4):583–610, 2016. ISSN 1432-0924. doi: 10.1007/s00466-015-1240-4.
- [10] C. Cellard, D. Reirant, M. François, E. Rouhaud, and D. Le Saunier. Laser shock peening of ti-17 titanium alloy: Influence of process parameters. *Materials Science and Engineering: A*, 532:362–372, 2012. ISSN 09215093. doi: 10.1016/j.msea.2011.10.104.
- [11] Ahmad Mostafa, Ignacio Picazo Rubio, Vladimir Brailovski, Mohammad Jahazi, and Mamoun Medraj. Structure, texture and phases in 3d printed in718 alloy subjected to homogenization and hip treatments. *Metals*, 7(6), 2017. ISSN 2075-4701. doi: 10.3390/met7060196.
- [12] Michael D. Sangid, Todd A. Book, Diwakar Naragani, John Rotella, Priya Ravi, Alexander Finch, Peter Kenesei, Jun-Sang Park, Hemant Sharma, Jonathan Almer, and Xianghui Xiao. Role of heat treatment and build orientation in the microstructure sensitive deformation characteristics of in718 produced via slm additive manufacturing. *Additive Manufacturing*, 22:479–496, 2018. ISSN 22148604. doi: 10.1016/j.addma.2018.04.032.
- [13] Johannes Ströbner, Michael Terock, and Uwe Glatzel. Mechanical and microstructural investigation of nickel-based superalloy in718 manufactured by selective laser melting (slm). *Advanced Engineering Materials*, 17(8):1099–1105, 2015. ISSN 14381656. doi: 10.1002/adem.201500158.
- [14] Meng Zhang, Chen-Nan Sun, Xiang Zhang, Phoi Chin Goh, Jun Wei, David Hardacre, and Hua Li. Fatigue and fracture behaviour of laser powder bed fusion stainless steel 316l: Influence of processing parameters. *Materials Science and Engineering: A*, 703:251–261, 2017. ISSN 0921-5093. doi: <https://doi.org/10.1016/j.msea.2017.07.071>.
- [15] Nima Shamsaei and Jutima Simsiriwong. Fatigue behaviour of additively-

manufactured metallic parts. *Procedia Structural Integrity*, 7:3–10, 2017. ISSN 2452-3216. doi: <https://doi.org/10.1016/j.prostr.2017.11.053>.

- [16] Roger C. Reed. *The Superalloys: Fundamentals and Applications*. Cambridge, 2006.
- [17] Panagiotis Stavropoulos, Panagis Foteinopoulos, Alexios Papacharalampopoulos, and Harry Bikas. Addressing the challenges for the industrial application of additive manufacturing: Towards a hybrid solution. *International Journal of Lightweight Materials and Manufacture*, 1(3):157–168, 2018. ISSN 25888404. doi: [10.1016/j.ijlmm.2018.07.002](https://doi.org/10.1016/j.ijlmm.2018.07.002).
- [18] M. Benedetti, V. Fontanari, M. Bandini, F. Zanini, and S. Carmignato. Low- and high-cycle fatigue resistance of ti-6al-4v eli additively manufactured via selective laser melting: Mean stress and defect sensitivity. *International Journal of Fatigue*, 107:96–109, 2018. ISSN 01421123. doi: [10.1016/j.ijfatigue.2017.10.021](https://doi.org/10.1016/j.ijfatigue.2017.10.021).
- [19] Sean Gribbin, Saeede Ghorbanpour, Nicholas C. Ferreri, Jonathan Bicknell, Igor Tsukrov, and Marko Knezevic. Role of grain structure, grain boundaries, crystallographic texture, precipitates, and porosity on fatigue behavior of inconel 718 at room and elevated temperatures. *Materials Characterization*, 149:184–197, 2019. ISSN 10445803. doi: [10.1016/j.matchar.2019.01.028](https://doi.org/10.1016/j.matchar.2019.01.028).
- [20] Bilal Ahmad, Sjoerd O. van der Veen, Michael E. Fitzpatrick, and Hua Guo. Residual stress evaluation in selective-laser-melting additively manufactured titanium (ti-6al-4v) and inconel 718 using the contour method and numerical simulation. *Additive Manufacturing*, 22:571–582, 2018. ISSN 22148604. doi: [10.1016/j.addma.2018.06.002](https://doi.org/10.1016/j.addma.2018.06.002).
- [21] P. Ganesh, R. Sundar, H. Kumar, R. Kaul, K. Ranganathan, P. Hedao, G. Raghavendra, S. Anand Kumar, P. Tiwari, D. C. Nagpure, K. S. Bindra, L. M. Kukreja, and S. M. Oak. Studies on fatigue life enhancement of pre-fatigued spring steel specimens using laser shock peening. *Materials & Design (1980-2015)*, 54:734–741, 2014. ISSN 02613069. doi: [10.1016/j.matdes.2013.08.104](https://doi.org/10.1016/j.matdes.2013.08.104).
- [22] Harold Luong and Michael R. Hill. The effects of laser peening on high-cycle fatigue in 7085-t7651 aluminum alloy. *Materials Science and Engineering: A*, 477(1):208–216, 2008. ISSN 0921-5093. doi: <https://doi.org/10.1016/j.msea.2007.05.024>.

- [23] Lloyd Hackel, Jochen Fuhr, Montu Sharma, Jon Rankin, Vincent Sherman, and Keivan Davami. Test results for wrought and am in718 treated by shot peening and laser peening plus thermal microstructure engineering. *Procedia Structural Integrity*, 19:452–462, 2019. ISSN 2452-3216. doi: <https://doi.org/10.1016/j.prostr.2019.12.049>.
- [24] William E. Frazier. Metal additive manufacturing: A review. *Journal of Materials Engineering and Performance*, 23(6):1917–1928, 2014. ISSN 1544-1024. doi: 10.1007/s11665-014-0958-z.
- [25] John J. Lewandowski and Mohsen Seifi. Metal additive manufacturing: A review of mechanical properties. *Annual Review of Materials Research*, 46(1):151–186, 2016. ISSN 1531-7331 1545-4118. doi: 10.1146/annurev-matsci-070115-032024.
- [26] Tuan D. Ngo, Alireza Kashani, Gabriele Imbalzano, Kate T. Q. Nguyen, and David Hui. Additive manufacturing (3d printing): A review of materials, methods, applications and challenges. *Composites Part B: Engineering*, 143:172–196, 2018. ISSN 13598368. doi: 10.1016/j.compositesb.2018.02.012.
- [27] Abdollah Saboori, Donato Gallo, Sara Biamino, Paolo Fino, and Mariangela Lombardi. An overview of additive manufacturing of titanium components by directed energy deposition: Microstructure and mechanical properties. *Applied Sciences*, 7(9), 2017. ISSN 2076-3417. doi: 10.3390/app7090883.
- [28] Kaufui V. Wong and Aldo Hernandez. A review of additive manufacturing. *ISRN Mechanical Engineering*, 2012:208760, 2012. ISSN xxxx-xxxx. doi: 10.5402/2012/208760.
- [29] Yi Zhang, Linmin Wu, Xingye Guo, Stephen Kane, Yifan Deng, Yeon-Gil Jung, Je-Hyun Lee, and Jing Zhang. Additive manufacturing of metallic materials: A review. *Journal of Materials Engineering and Performance*, 27(1):1–13, 2018. ISSN 1544-1024. doi: 10.1007/s11665-017-2747-y.
- [30] Chang-Jun Bae, Alisha B. Diggs, and Arathi Ramachandran. 6 - quantification and certification of additive manufacturing materials and processes. In Jing Zhang and Yeon-Gil Jung, editors, *Additive Manufacturing*, pages 181–213. Butterworth-Heinemann, 2018. ISBN 978-0-12-812155-9. doi: <https://doi.org/10.1016/B978-0-12-812155-9.00006-2>.
- [31] Adriaan Spierings and Gideon Levy. Comparison of density of stainless steel 316l parts produced with selective laser melting using different powder grades.

20th Annual International Solid Freeform Fabrication Symposium, SFF 2009, 2009.

- [32] Gregor Jacob, Christopher Brown, and Alkan Donmez. The influence of spreading metal powders with different particle size distributions on the powder bed density in laser-based powder bed fusion processes, 2018.
- [33] Quy Bau Nguyen, Mui Ling Sharon Nai, Zhiguang Zhu, Chen-Nan Sun, Jun Wei, and Wei Zhou. Characteristics of inconel powders for powder-bed additive manufacturing. *Engineering*, 3(5):695–700, 2017. ISSN 2095-8099. doi: <https://doi.org/10.1016/J.ENG.2017.05.012>.
- [34] Alessandro Averardi, Corrado Cola, Steven Eric Zeltmann, and Nikhil Gupta. Effect of particle size distribution on the packing of powder beds: A critical discussion relevant to additive manufacturing. *Materials Today Communications*, 24:100964, 2020. ISSN 2352-4928. doi: <https://doi.org/10.1016/j.mtcomm.2020.100964>.
- [35] Statista. 3d printing market distribution worldwide in 2016, by use case. Report, 2016.
- [36] Roland Berger. Additive manufacturing in aerospace and defense. Report, 2017.
- [37] Joy Gockel, Luke Sheridan, Brittanie Koerper, and Bo Whip. The influence of additive manufacturing processing parameters on surface roughness and fatigue life. *International Journal of Fatigue*, 124:380–388, 2019. ISSN 01421123. doi: 10.1016/j.ijfatigue.2019.03.025.
- [38] Bilal Ahmad, Sjoerd O. van der Veen, Michael E. Fitzpatrick, and Hua Guo. Residual stress evaluation in selective-laser-melting additively manufactured titanium (ti-6al-4v) and inconel 718 using the contour method and numerical simulation. *Additive Manufacturing*, 22:571–582, 2018. ISSN 22148604. doi: 10.1016/j.addma.2018.06.002.
- [39] Rakesh Kumar, Manoj Kumar, and Jasgurpreet Singh Chohan. The role of additive manufacturing for biomedical applications: A critical review. *Journal of Manufacturing Processes*, 64:828–850, 2021. ISSN 1526-6125. doi: <https://doi.org/10.1016/j.jmapro.2021.02.022>.
- [40] Alexander Paolini, Stefan Kollmannsberger, and Ernst Rank. Additive manufacturing in construction: A review on processes, applications, and digital

planning methods. *Additive Manufacturing*, 30:100894, 2019. ISSN 2214-8604. doi: <https://doi.org/10.1016/j.addma.2019.100894>.

- [41] Mohsen Seifi, Ayman Salem, Jack Beuth, Ola Harrysson, and John J. Lewandowski. Overview of materials qualification needs for metal additive manufacturing. *JOM*, 68(3):747–764, 2016. ISSN 1543-1851. doi: 10.1007/s11837-015-1810-0.
- [42] J. Michael Wilson, Cecil Piya, Yung C. Shin, Fu Zhao, and Karthik Ramani. Remanufacturing of turbine blades by laser direct deposition with its energy and environmental impact analysis. *Journal of Cleaner Production*, 80:170–178, 2014. ISSN 09596526. doi: 10.1016/j.jclepro.2014.05.084.
- [43] Additive manufacturing 3d opportunity in aerospace. Report, Deloitte, 2014.
- [44] Siavash H. Khajavi, Jouni Partanen, and Jan Holmström. Additive manufacturing in the spare parts supply chain. *Computers in Industry*, 65(1):50–63, 2014. ISSN 01663615. doi: 10.1016/j.compind.2013.07.008.
- [45] Lourdes D. Bobbio, Shipin Qin, Alexander Dunbar, Panagiotis Michaleris, and Allison M. Beese. Characterization of the strength of support structures used in powder bed fusion additive manufacturing of ti-6al-4v. *Additive Manufacturing*, 14:60–68, 2017. ISSN 22148604. doi: 10.1016/j.addma.2017.01.002.
- [46] Andrew H. Chern, Peeyush Nandwana, Tao Yuan, Michael M. Kirka, Ryan R. Dehoff, Peter K. Liaw, and Chad E. Duty. A review on the fatigue behavior of ti-6al-4v fabricated by electron beam melting additive manufacturing. *International Journal of Fatigue*, 119:173–184, 2019. ISSN 01421123. doi: 10.1016/j.ijfatigue.2018.09.022.
- [47] Ali Fatemi, Reza Molaei, Shahriar Sharifimehr, Nam Phan, and Nima Shamsaei. Multiaxial fatigue behavior of wrought and additive manufactured ti-6al-4v including surface finish effect. *International Journal of Fatigue*, 100:347–366, 2017. ISSN 01421123. doi: 10.1016/j.ijfatigue.2017.03.044.
- [48] Ali Fatemi, Reza Molaei, Shahriar Sharifimehr, Nima Shamsaei, and Nam Phan. Torsional fatigue behavior of wrought and additive manufactured ti-6al-4v by powder bed fusion including surface finish effect. *International Journal of Fatigue*, 99:187–201, 2017. ISSN 01421123. doi: 10.1016/j.ijfatigue.2017.03.002.

- [49] J. Günther, D. Krewerth, T. Lippmann, S. Leuders, T. Tröster, A. Weidner, H. Biermann, and T. Niendorf. Fatigue life of additively manufactured ti-6al-4v in the very high cycle fatigue regime. *International Journal of Fatigue*, 94:236–245, 2017. ISSN 01421123. doi: 10.1016/j.ijfatigue.2016.05.018.
- [50] D. Levy, A. Shirizly, and D. Rittel. Static and dynamic comprehensive response of additively manufactured discrete patterns of ti6al4v. *International Journal of Impact Engineering*, 122:182–196, 2018. ISSN 0734743X. doi: 10.1016/j.ijimpeng.2018.07.014.
- [51] M. Mazur, M. Leary, M. McMillan, S. Sun, D. Shidid, and M. Brandt. *Mechanical properties of Ti6Al4V and AlSi12Mg lattice structures manufactured by Selective Laser Melting (SLM)*, pages 119–161. 2017. ISBN 9780081004333. doi: 10.1016/b978-0-08-100433-3.00005-1.
- [52] Reza Molaei, Ali Fatemi, and Nam Phan. Significance of hot isostatic pressing (hip) on multiaxial deformation and fatigue behaviors of additive manufactured ti-6al-4v including build orientation and surface roughness effects. *International Journal of Fatigue*, 117:352–370, 2018. ISSN 01421123. doi: 10.1016/j.ijfatigue.2018.07.035.
- [53] Jonathan Pegues, Michael Roach, R. Scott Williamson, and Nima Shamsaei. Surface roughness effects on the fatigue strength of additively manufactured ti-6al-4v. *International Journal of Fatigue*, 116:543–552, 2018. ISSN 01421123. doi: 10.1016/j.ijfatigue.2018.07.013.
- [54] Yadir Torres, Perla Sarria, Francisco José Gotor, Eliel Gutiérrez, Eduardo Peon, Ana María Beltrán, and Jesús E. González. Surface modification of ti-6al-4v alloys manufactured by selective laser melting: Microstructural and tribo-mechanical characterization. *Surface and Coatings Technology*, 348:31–40, 2018. ISSN 02578972. doi: 10.1016/j.surfcoat.2018.05.015.
- [55] Lijun Xiao and Weidong Song. Additively-manufactured functionally graded ti-6al-4v lattice structures with high strength under static and dynamic loading: Experiments. *International Journal of Impact Engineering*, 111:255–272, 2018. ISSN 0734743X. doi: 10.1016/j.ijimpeng.2017.09.018.
- [56] Yan-Yan Zhu, Hai-Bo Tang, Zhuo Li, Cheng Xu, and Bei He. Solidification behavior and grain morphology of laser additive manufacturing titanium alloys. *Journal of Alloys and Compounds*, 777:712–716, 2019. ISSN 09258388. doi: 10.1016/j.jallcom.2018.11.055.

- [57] Yunhui Chen, Samuel J. Clark, Lorna Sinclair, Chu Lun Alex Leung, Sebastian Marussi, Thomas Connolley, Robert C. Atwood, Gavin J. Baxter, Martyn A. Jones, Iain Todd, and Peter D. Lee. Synchrotron x-ray imaging of directed energy deposition additive manufacturing of titanium alloy ti-6242. *Additive Manufacturing*, 41:101969, 2021. ISSN 2214-8604.
- [58] Mohammad Elahinia, Narges Shayesteh Moghaddam, Mohsen Taheri Andani, Amirhesam Amerinatanzi, Beth A. Bimber, and Reginald F. Hamilton. Fabrication of niti through additive manufacturing: A review. *Progress in Materials Science*, 83:630–663, 2016. ISSN 00796425. doi: 10.1016/j.pmatsci.2016.08.001.
- [59] M. Mahmoudi, G. Tapia, B. Franco, J. Ma, R. Arroyave, I. Karaman, and A. Elwany. On the printability and transformation behavior of nickel-titanium shape memory alloys fabricated using laser powder-bed fusion additive manufacturing. *Journal of Manufacturing Processes*, 35:672–680, 2018. ISSN 15266125. doi: 10.1016/j.jmapro.2018.08.037.
- [60] Narges Shayesteh Moghaddam, Sayed Ehsan Saghaian, Amirhesam Amerinatanzi, Hamdy Ibrahim, Peizhen Li, Guher P. Toker, Haluk E. Karaca, and Mohammad Elahinia. Anisotropic tensile and actuation properties of niti fabricated with selective laser melting. *Materials Science and Engineering: A*, 724:220–230, 2018. ISSN 09215093. doi: 10.1016/j.msea.2018.03.072.
- [61] Quan Zhou, Muhammad Dilawer Hayat, Gang Chen, Song Cai, Xuanhui Qu, Huiping Tang, and Peng Cao. Selective electron beam melting of niti: Microstructure, phase transformation and mechanical properties. *Materials Science and Engineering: A*, 744:290–298, 2019. ISSN 09215093. doi: 10.1016/j.msea.2018.12.023.
- [62] Hahn Choo, Kin-Ling Sham, John Bohling, Austin Ngo, Xianghui Xiao, Yang Ren, Philip J. Depond, Manyalibo J. Matthews, and Elena Garlea. Effect of laser power on defect, texture, and microstructure of a laser powder bed fusion processed 316l stainless steel. *Materials & Design*, 164, 2019. ISSN 02641275. doi: 10.1016/j.matdes.2018.12.006.
- [63] Michael J. Heiden, Lisa A. Deibler, Jeff M. Rodelas, Josh R. Koepke, Dan J. Tung, David J. Saiz, and Bradley H. Jared. Evolution of 316l stainless steel feedstock due to laser powder bed fusion process. *Additive Manufacturing*, 25: 84–103, 2019. ISSN 22148604. doi: 10.1016/j.addma.2018.10.019.

- [64] Harish Irrinki, John Samuel Dilip Jangam, Somayeh Pasebani, Sunil Badwe, Jason Stitzel, Kunal Kate, Ozkan Gulsoy, and Sundar V. Atre. Effects of particle characteristics on the microstructure and mechanical properties of 17-4 ph stainless steel fabricated by laser-powder bed fusion. *Powder Technology*, 331:192–203, 2018. ISSN 00325910. doi: 10.1016/j.powtec.2018.03.025.
- [65] Subrata Deb Nath, Harish Irrinki, Gautam Gupta, Martin Kearns, Ozkan Gulsoy, and Sundar Atre. Microstructure-property relationships of 420 stainless steel fabricated by laser-powder bed fusion. *Powder Technology*, 343:738–746, 2019. ISSN 00325910. doi: 10.1016/j.powtec.2018.11.075.
- [66] I. A. Segura, L. E. Murr, C. A. Terrazas, D. Bermudez, J. Mireles, V. S. V. Injeti, K. Li, B. Yu, R. D. K. Misra, and R. B. Wicker. Grain boundary and microstructure engineering of inconel 690 cladding on stainless-steel 316l using electron-beam powder bed fusion additive manufacturing. *Journal of Materials Science & Technology*, 35(2):351–367, 2019. ISSN 10050302. doi: 10.1016/j.jmst.2018.09.059.
- [67] Xianglong Wang, Jose Alberto Muñiz-Lerma, Oscar Sánchez-Mata, Mohammad Attarian Shandiz, and Mathieu Brochu. Microstructure and mechanical properties of stainless steel 316l vertical struts manufactured by laser powder bed fusion process. *Materials Science and Engineering: A*, 736:27–40, 2018. ISSN 09215093. doi: 10.1016/j.msea.2018.08.069.
- [68] Yiğit M. Arsoy, Luis E. Criales, and Tuğrul Özel. Modeling and simulation of thermal field and solidification in laser powder bed fusion of nickel alloy in625. *Optics & Laser Technology*, 109:278–292, 2019. ISSN 00303992. doi: 10.1016/j.optlastec.2018.08.016.
- [69] Ercan Cakmak, Michael M. Kirka, Thomas R. Watkins, Ryan C. Cooper, Ke An, Hahn Choo, Wei Wu, Ryan R. Dehoff, and Sudarsanam S. Babu. Microstructural and micromechanical characterization of in718 theta shaped specimens built with electron beam melting. *Acta Materialia*, 108:161–175, 2016. ISSN 13596454. doi: 10.1016/j.actamat.2016.02.005.
- [70] Zhen Chen, Shenggui Chen, Zhengying Wei, Lijuan Zhang, Pei Wei, Bingheng Lu, Shuzhe Zhang, and Yu Xiang. Anisotropy of nickel-based superalloy k418 fabricated by selective laser melting. *Progress in Natural Science: Materials International*, 28(4):496–504, 2018. ISSN 10020071. doi: 10.1016/j.pnsc.2018.07.001.

- [71] Jonathan Jones, Mark Whittaker, Robert Lancaster, and Stephen Williams. The influence of phase angle, strain range and peak cycle temperature on the tmf crack initiation behaviour and damage mechanisms of the nickel-based superalloy, rr1000. *International Journal of Fatigue*, 98:279–285, 2017. ISSN 01421123. doi: 10.1016/j.ijfatigue.2017.01.036.
- [72] S. J. Davies, S. P. Jeffs, M. P. Coleman, and R. J. Lancaster. Effects of heat treatment on microstructure and creep properties of a laser powder bed fused nickel superalloy. *Materials & Design*, 159:39–46, 2018. ISSN 02641275. doi: 10.1016/j.matdes.2018.08.039.
- [73] Dunyong Deng, Johan Moverare, Ru Lin Peng, and Hans Söderberg. Microstructure and anisotropic mechanical properties of ebm manufactured inconel 718 and effects of post heat treatments. *Materials Science and Engineering: A*, 693:151–163, 2017. ISSN 09215093. doi: 10.1016/j.msea.2017.03.085.
- [74] Dunyong Deng, Ru Lin Peng, Håkan Brodin, and Johan Moverare. Microstructure and mechanical properties of inconel 718 produced by selective laser melting: Sample orientation dependence and effects of post heat treatments. *Materials Science and Engineering: A*, 713:294–306, 2018. ISSN 09215093. doi: 10.1016/j.msea.2017.12.043.
- [75] Reza Esmailizadeh, Usman Ali, Ali Keshavarzkermani, Yahya Mahmoodkhani, Ehsan Marzbanrad, and Ehsan Toyserkani. On the effect of spatter particles distribution on the quality of hastelloy x parts made by laser powder-bed fusion additive manufacturing. *Journal of Manufacturing Processes*, 37: 11–20, 2019. ISSN 15266125. doi: 10.1016/j.jmapro.2018.11.012.
- [76] Bryton Farber, Kathryn A. Small, Christopher Allen, Robert J. Causton, Ashley Nichols, John Symbolick, and Mitra L. Taheri. Correlation of mechanical properties to microstructure in inconel 718 fabricated by direct metal laser sintering. *Materials Science and Engineering: A*, 712:539–547, 2018. ISSN 09215093. doi: 10.1016/j.msea.2017.11.125.
- [77] M. Haines, A. Plotkowski, C. L. Frederick, E. J. Schwalbach, and S. S. Babu. A sensitivity analysis of the columnar-to-equiaxed transition for ni-based superalloys in electron beam additive manufacturing. *Computational Materials Science*, 155:340–349, 2018. ISSN 09270256. doi: 10.1016/j.commatsci.2018.08.064.

- [78] Lena Huynh, John Rotella, and Michael D. Sangid. Fatigue behavior of in718 microtrusses produced via additive manufacturing. *Materials & Design*, 105: 278–289, 2016. ISSN 02641275. doi: 10.1016/j.matdes.2016.05.032.
- [79] C. Juillet, A. Oudriss, J. Balmain, X. Feaugas, and F. Pedraza. Characterization and oxidation resistance of additive manufactured and forged in718 ni-based superalloys. *Corrosion Science*, 142:266–276, 2018. ISSN 0010938X. doi: 10.1016/j.corsci.2018.07.032.
- [80] R. Konečná, L. Kunz, G. Nicoletto, and A. Bača. Long fatigue crack growth in inconel 718 produced by selective laser melting. *International Journal of Fatigue*, 92:499–506, 2016. ISSN 01421123. doi: 10.1016/j.ijfatigue.2016.03.012.
- [81] Alena Kreitchberg, Vladimir Brailovski, and Sylvain Turenne. Effect of heat treatment and hot isostatic pressing on the microstructure and mechanical properties of inconel 625 alloy processed by laser powder bed fusion. *Materials Science and Engineering: A*, 689:1–10, 2017. ISSN 09215093. doi: 10.1016/j.msea.2017.02.038.
- [82] Alena Kreitchberg, Vladimir Brailovski, and Sylvain Turenne. Elevated temperature mechanical behavior of in625 alloy processed by laser powder-bed fusion. *Materials Science and Engineering: A*, 700:540–553, 2017. ISSN 09215093. doi: 10.1016/j.msea.2017.06.045.
- [83] Yen-Ling Kuo, Shota Horikawa, and Koji Takehi. The effect of interdendritic δ phase on the mechanical properties of alloy 718 built up by additive manufacturing. *Materials & Design*, 116:411–418, 2017. ISSN 02641275. doi: 10.1016/j.matdes.2016.12.026.
- [84] Martin Leary, Maciej Mazur, Hugh Williams, Eric Yang, Ahmad Alghamdi, Bill Lozanovski, Xuezhe Zhang, Darpan Shidid, Lena Farahbod-Sternahl, Gerd Witt, Ingomar Kelbassa, Peter Choong, Ma Qian, and Milan Brandt. Inconel 625 lattice structures manufactured by selective laser melting (slm): Mechanical properties, deformation and failure modes. *Materials & Design*, 157:179–199, 2018. ISSN 02641275. doi: 10.1016/j.matdes.2018.06.010.
- [85] Dong Ma, Alexandru D. Stoica, Zhuqing Wang, and Allison M. Beese. Crystallographic texture in an additively manufactured nickel-base superalloy. *Materials Science and Engineering: A*, 684:47–53, 2017. ISSN 09215093. doi: 10.1016/j.msea.2016.12.028.

- [86] Mang Ni, Chao Chen, Xiaojun Wang, Pengwei Wang, Ruidi Li, Xiaoyong Zhang, and Kechao Zhou. Anisotropic tensile behavior of in situ precipitation strengthened inconel 718 fabricated by additive manufacturing. *Materials Science and Engineering: A*, 701:344–351, 2017. ISSN 09215093. doi: 10.1016/j.msea.2017.06.098.
- [87] Veerappan Prithivirajan and Michael D. Sangid. The role of defects and critical pore size analysis in the fatigue response of additively manufactured in718 via crystal plasticity. *Materials & Design*, 150:139–153, 2018. ISSN 02641275. doi: 10.1016/j.matdes.2018.04.022.
- [88] M. Pröbstle, S. Neumeier, J. Hopfenmüller, L. P. Freund, T. Niendorf, D. Schwarze, and M. Göken. Superior creep strength of a nickel-based superalloy produced by selective laser melting. *Materials Science and Engineering: A*, 674:299–307, 2016. ISSN 09215093. doi: 10.1016/j.msea.2016.07.061.
- [89] H. Qi, M. Azer, and A. Ritter. Studies of standard heat treatment effects on microstructure and mechanical properties of laser net shape manufactured inconel 718. *Metallurgical and Materials Transactions A*, 40(10):2410–2422, 2009. ISSN 1073-5623 1543-1940. doi: 10.1007/s11661-009-9949-3.
- [90] Tahira Raza, Joel Andersson, and Lars-Erik Svensson. Microstructure of slm alloy 718 in as-manufactured and post heat treated condition. *8th Swedish Production Symposium, SPS 2018*, 2018.
- [91] Luke Sheridan, Onome E. Scott-Emuakpor, Tommy George, and Joy E. Gockel. Relating porosity to fatigue failure in additively manufactured alloy 718. *Materials Science and Engineering: A*, 727:170–176, 2018. ISSN 09215093. doi: 10.1016/j.msea.2018.04.075.
- [92] Shang Sui, Jing Chen, Enxiang Fan, Haiou Yang, Xin Lin, and Weidong Huang. The influence of laves phases on the high-cycle fatigue behavior of laser additive manufactured inconel 718. *Materials Science and Engineering: A*, 695:6–13, 2017. ISSN 09215093. doi: 10.1016/j.msea.2017.03.098.
- [93] Shang Sui, Hua Tan, Jing Chen, Chongliang Zhong, Zuo Li, Wei Fan, Andres Gasser, and Weidong Huang. The influence of laves phases on the room temperature tensile properties of inconel 718 fabricated by powder feeding laser additive manufacturing. *Acta Materialia*, 164:413–427, 2019. ISSN 13596454. doi: 10.1016/j.actamat.2018.10.032.

- [94] Shi-Hai Sun, Yuichiro Koizumi, Tsuyoshi Saito, Kenta Yamanaka, Yun-Ping Li, Yujie Cui, and Akihiko Chiba. Electron beam additive manufacturing of inconel 718 alloy rods: Impact of build direction on microstructure and high-temperature tensile properties. *Additive Manufacturing*, 23:457–470, 2018. ISSN 22148604. doi: 10.1016/j.addma.2018.08.017.
- [95] Pan Tao, Huaixue Li, Baiying Huang, Quandong Hu, Shuili Gong, and Qingyan Xu. The crystal growth, intercellular spacing and microsegregation of selective laser melted inconel 718 superalloy. *Vacuum*, 159:382–390, 2019. ISSN 0042207X. doi: 10.1016/j.vacuum.2018.10.074.
- [96] W. Tillmann, C. Schaak, J. Nellesen, M. Schaper, M. E. Aydinöz, and K. P. Hoyer. Hot isostatic pressing of in718 components manufactured by selective laser melting. *Additive Manufacturing*, 13:93–102, 2017. ISSN 22148604. doi: 10.1016/j.addma.2016.11.006.
- [97] Zemin Wang, Kai Guan, Ming Gao, Xiangyou Li, Xiaofeng Chen, and Xiaoyan Zeng. The microstructure and mechanical properties of deposited-in718 by selective laser melting. *Journal of Alloys and Compounds*, 513:518–523, 2012. ISSN 09258388. doi: 10.1016/j.jallcom.2011.10.107.
- [98] Z. Xu, J. W. Murray, C. J. Hyde, and A. T. Clare. Effect of post processing on the creep performance of laser powder bed fused inconel 718. *Additive Manufacturing*, 24:486–497, 2018. ISSN 22148604. doi: 10.1016/j.addma.2018.10.027.
- [99] Zhengkai Xu, C. J. Hyde, C. Tuck, and A. T. Clare. Creep behaviour of inconel 718 processed by laser powder bed fusion. *Journal of Materials Processing Technology*, 256:13–24, 2018. ISSN 09240136. doi: 10.1016/j.jmatprotec.2018.01.040.
- [100] Yung Suk Jeremy Yoo, Todd A. Book, Michael D. Sangid, and Josh Kacher. Identifying strain localization and dislocation processes in fatigued inconel 718 manufactured from selective laser melting. *Materials Science and Engineering: A*, 724:444–451, 2018. ISSN 09215093. doi: 10.1016/j.msea.2018.03.127.
- [101] Dongyun Zhang, Zhe Feng, Chengjie Wang, Weidong Wang, Zhen Liu, and Wen Niu. Comparison of microstructures and mechanical properties of inconel 718 alloy processed by selective laser melting and casting. *Materials Science and Engineering: A*, 724:357–367, 2018. ISSN 09215093. doi: 10.1016/j.msea.2018.03.073.

- [102] A. K. Gujba and M. Medraj. Laser peening process and its impact on materials properties in comparison with shot peening and ultrasonic impact peening. *Materials (Basel)*, 7(12):7925–7974, 2014. ISSN 1996-1944 (Print) 1996-1944 (Linking). doi: 10.3390/ma7127925.
- [103] Xiaoming Zhao, Jing Chen, Xin Lin, and Weidong Huang. Study on microstructure and mechanical properties of laser rapid forming inconel 718. *Materials Science and Engineering: A*, 478(1-2):119–124, 2008. ISSN 09215093. doi: 10.1016/j.msea.2007.05.079.
- [104] P. Kanagarajah, F. Brenne, T. Niendorf, and H.J. Maier. Inconel 939 processed by selective laser melting: Effect of microstructure and temperature on the mechanical properties under static and cyclic loading. *Materials Science and Engineering: A*, 588:188–195, 2013. ISSN 0921-5093.
- [105] Hong Qin, Vahid Fallah, Qingshan Dong, Mathieu Brochu, Mark R. Daymond, and Mark Gallerneault. Solidification pattern, microstructure and texture development in laser powder bed fusion (lpbf) of al10sing alloy. *Materials Characterization*, 145:29–38, 2018. ISSN 10445803. doi: 10.1016/j.matchar.2018.08.025.
- [106] Syed Z. Uddin, Lawrence E. Murr, Cesar A. Terrazas, Philip Morton, David A. Roberson, and Ryan B. Wicker. Processing and characterization of crack-free aluminum 6061 using high-temperature heating in laser powder bed fusion additive manufacturing. *Additive Manufacturing*, 22:405–415, 2018. ISSN 22148604. doi: 10.1016/j.addma.2018.05.047.
- [107] Kartik Prasad, Rajdeep Sarkar, P. Ghosal, and Vikas Kumar. Simultaneous creep–fatigue damage accumulation of forged turbine disc of in 718 superalloy. *Materials Science and Engineering: A*, 572:1–7, 2013. ISSN 09215093. doi: 10.1016/j.msea.2013.02.003.
- [108] Jingyu Sun and Huang Yuan. Life assessment of multiaxial thermomechanical fatigue of a nickel-based superalloy inconel 718. *International Journal of Fatigue*, 120:228–240, 2019. ISSN 01421123. doi: 10.1016/j.ijfatigue.2018.11.018.
- [109] Itziar Serrano-Munoz, Tatiana Mishurova, Tobias Thiede, Maximilian Sprengel, Arne Kromm, Naresh Nadammal, Gert Nolze, Romeo Saliwan-Neumann, Alexander Evans, and Giovanni Bruno. The residual stress in as-built laser powder bed fusion in718 alloy as a consequence of the scanning strategy in-

- duced microstructure. *Scientific Reports*, 10(1):14645, 2020. ISSN 2045-2322. doi: 10.1038/s41598-020-71112-9.
- [110] A. Verma, B. Paul, Jung Singh, K. Ramaswamy, Siddhant Nalawade, and M. Sundararaman. Evolution of delta phase microstructure in alloy 718. pages 737–750, 01 2010. doi: 10.7449/2010/Superalloys2010737750.
- [111] K. N. Amato, S. M. Gaytan, L. E. Murr, E. Martinez, P. W. Shindo, J. Hernandez, S. Collins, and F. Medina. Microstructures and mechanical behavior of inconel 718 fabricated by selective laser melting. *Acta Materialia*, 60(5):2229–2239, 2012. ISSN 13596454. doi: 10.1016/j.actamat.2011.12.032.
- [112] G. H. Cao, T. Y. Sun, C. H. Wang, Xing Li, M. Liu, Z. X. Zhang, P. F. Hu, A. M. Russell, R. Schneider, D. Gerthsen, Z. J. Zhou, C. P. Li, and G. F. Chen. Investigations of γ , γ'' and δ precipitates in heat-treated inconel 718 alloy fabricated by selective laser melting. *Materials Characterization*, 136:398–406, 2018. ISSN 10445803. doi: 10.1016/j.matchar.2018.01.006.
- [113] Ian Gibson, David W Rosen, and Brent Stucker. *Additive Manufacturing Technologies*. 2010. ISBN 978-1-4419-1119-3. doi: 10.1007/978-1-4419-1120-9.
- [114] Meng Guo, Dongdong Gu, Lixia Xi, Lei Du, Hongmei Zhang, and Jiayao Zhang. Formation of scanning tracks during selective laser melting (slm) of pure tungsten powder: Morphology, geometric features and forming mechanisms. *International Journal of Refractory Metals and Hard Materials*, 79:37–46, 2019. ISSN 0263-4368. doi: <https://doi.org/10.1016/j.ijrmhm.2018.11.003>.
- [115] H. M. Khan, M. H. Dirikolu, E. Koç, and Z. C. Oter. Numerical investigation of heat current study across different platforms in slm processed multi-layer als10mg. *Optik*, 170:82–89, 2018. ISSN 0030-4026. doi: <https://doi.org/10.1016/j.ijleo.2018.05.081>.
- [116] Lavinia Tonelli, Alessandro Fortunato, and Lorella Ceschini. Cocr alloy processed by selective laser melting (slm): effect of laser energy density on microstructure, surface morphology, and hardness. *Journal of Manufacturing Processes*, 52:106–119, 2020. ISSN 1526-6125. doi: <https://doi.org/10.1016/j.jmapro.2020.01.052>.
- [117] M. Kirka, Kinga Unocic, Narendran Raghavan, Francisco Medina, Ryan Dehoff, and Sudarsanam Babu. Microstructure development in electron beam-melted inconel 718 and associated tensile properties. *JOM*, 68, 2016. doi: 10.1007/s11837-016-1812-6.
- [118] Yuan Chen, Fenggui Lu, Ke Zhang, Pulin Nie, Seyed Reza Elmi Hosseini, Kai Feng, and Zhuguo Li. Dendritic microstructure and hot cracking of

- laser additive manufactured inconel 718 under improved base cooling. *Journal of Alloys and Compounds*, 670:312–321, 2016. ISSN 0925-8388. doi: <https://doi.org/10.1016/j.jallcom.2016.01.250>.
- [119] Fencheng Liu, Xin Lin, Han Leng, Jun Cao, Qiang Liu, Chunping Huang, and Weidong Huang. Microstructural changes in a laser solid forming inconel 718 superalloy thin wall in the deposition direction. *Optics Laser Technology*, 45:330–335, 2013. ISSN 0030-3992. doi: <https://doi.org/10.1016/j.optlastec.2012.06.028>.
- [120] Derek H. Smith, Jonathan Bicknell, Luke Jorgensen, Brian M. Patterson, Nikolaus L. Cordes, Igor Tsukrov, and Marko Knezevic. Microstructure and mechanical behavior of direct metal laser sintered inconel alloy 718. *Materials Characterization*, 113:1–9, 2016. ISSN 10445803. doi: [10.1016/j.matchar.2016.01.003](https://doi.org/10.1016/j.matchar.2016.01.003).
- [121] Arun Ramanathan Balachandramurthi, Johan Moverare, Nikhil Dixit, and Robert Pederson. Influence of defects and as-built surface roughness on fatigue properties of additively manufactured alloy 718. *Materials Science and Engineering: A*, 735:463–474, 2018. ISSN 09215093. doi: [10.1016/j.msea.2018.08.072](https://doi.org/10.1016/j.msea.2018.08.072).
- [122] L. Doremus, J. Cormier, P. Villechaise, G. Henaff, Y. Nadot, and S. Pierret. Influence of residual stresses on the fatigue crack growth from surface anomalies in a nickel-based superalloy. *Materials Science & Engineering A*, 2015.
- [123] G.A. Webster and A.N. Ezeilo. Residual stress distributions and their influence on fatigue lifetimes. *International Journal of Fatigue*, 23:375–383, 2001. ISSN 0142-1123. doi: [https://doi.org/10.1016/S0142-1123\(01\)00133-5](https://doi.org/10.1016/S0142-1123(01)00133-5).
- [124] N. Kalentics, K. Huang, M. Ortega Varela de Seijas, A. Burn, V. Romano, and R. E. Logé. Laser shock peening: A promising tool for tailoring metallic microstructures in selective laser melting. *Journal of Materials Processing Technology*, 266:612–618, 2019. ISSN 09240136. doi: [10.1016/j.jmatprotec.2018.11.024](https://doi.org/10.1016/j.jmatprotec.2018.11.024).
- [125] M. Anderson, A. L. Thielin, F. Bridier, P. Bocher, and J. Savoie. δ phase precipitation in inconel 718 and associated mechanical properties. *Materials Science and Engineering: A*, 679:48–55, 2017. ISSN 0921-5093. doi: <https://doi.org/10.1016/j.msea.2016.09.114>.
- [126] Shuqi Li, Jingyun Zhuang, Jinyan Yang, Qun Deng, and Jinhui Du. The effect of delta-phase on crack propagation under creep and fatigue conditions in alloy 718. *Superalloys 718, 625,706 and Various Derivatives*, 1994.

- [127] Jinlan An, Lei Wang, Yang Liu, Wenliang Cai, and Xiu Song. The role of δ phase for fatigue crack propagation behavior in a ni base superalloy at room temperature. *Materials Science and Engineering: A*, 684:312–317, 2017. ISSN 09215093. doi: 10.1016/j.msea.2016.12.029.
- [128] Nikola Kalentics, Eric Boillat, Patrice Peyre, Snežana Čirić Kostić, Nebojša Bogojević, and Roland E. Logé. Tailoring residual stress profile of selective laser melted parts by laser shock peening. *Additive Manufacturing*, 16:90–97, 2017. ISSN 22148604. doi: 10.1016/j.addma.2017.05.008.
- [129] John J. deBarbadillo and Sarwan K. Mannan. Alloy 718 for oilfield applications. *JOM*, 2012. ISSN 1543-1851. doi: 10.1007/s11837-012-0238-z. URL <https://doi.org/10.1007/s11837-012-0238-z>.
- [130] Aref Yadollahi and Nima Shamsaei. Additive manufacturing of fatigue resistant materials: Challenges and opportunities. *International Journal of Fatigue*, 98:14–31, 2017. ISSN 0142-1123. doi: <https://doi.org/10.1016/j.ijfatigue.2017.01.001>.
- [131] S. Beretta and S. Romano. A comparison of fatigue strength sensitivity to defects for materials manufactured by am or traditional processes. *International Journal of Fatigue*, 94:178–191, 2017. ISSN 0142-1123. doi: <https://doi.org/10.1016/j.ijfatigue.2016.06.020>. Fatigue and Fracture Behavior of Additive Manufactured Parts.
- [132] Xinyuan Jin, Liang Lan, Shuang Gao, Bo He, and Yonghua Rong. Effects of laser shock peening on microstructure and fatigue behavior of ti-6al-4v alloy fabricated via electron beam melting. *Materials Science and Engineering: A*, 780, 2020. ISSN 09215093. doi: 10.1016/j.msea.2020.139199.
- [133] Goran Ivetic, Ivan Meneghin, Enrico Troiani, Gianluca Molinari, José Ocaña, Miguel Morales, Juan Porro, Agostino Lanciotti, Vjola Ristori, Claudia Polese, Jasper Plaisier, and Andrea Lausi. Fatigue in laser shock peened open-hole thin aluminium specimens. *Materials Science and Engineering: A*, 534:573–579, 2012. ISSN 0921-5093. doi: <https://doi.org/10.1016/j.msea.2011.12.010>.
- [134] Yongkang Zhang, Jian You, Jinzhong Lu, Chengyun Cui, Yingfang Jiang, and Xudong Ren. Effects of laser shock processing on stress corrosion cracking susceptibility of az31b magnesium alloy. *Surface and Coatings Technology*, 204(24): 3947–3953, 2010. ISSN 02578972. doi: 10.1016/j.surfcoat.2010.03.015.
- [135] Sundar, Ganesh, Ram Kishor Gupta, Ragvendra, Pant, Vivekanand Kain, Ranganathan, Rakesh Kaul, and Bindra. Laser shock peening and its applications:

- A review. *Lasers in Manufacturing and Materials Processing*, 6(4):424–463, 2019. ISSN 2196-7229 2196-7237. doi: 10.1007/s40516-019-00098-8.
- [136] <https://www.lambdatechs.com/laser-peening/>, 2020. [Online; accessed 01-Jan-2022].
- [137] Peyre and Fabbro. Laser shock processing : a review of the physics and applications. *Optical and Quantum Electronics*, 27, 1995. doi: 10.1007/BF00326477.
- [138] R. Fabbro, J. Fournier, P. Ballard, D. Devaux, and J. Virmont. Physical study of laser-produced plasma in confined geometry. *Journal of Applied Physics*, 68(2): 775–784, 1990. ISSN 0021-8979 1089-7550. doi: 10.1063/1.346783.
- [139] R. Sundar, H. Kumar, R. Kaul, K. Ranganathan, P. Tiwari, L. M. Kukreja, and S. M. Oak. Studies on laser peening using different sacrificial coatings. *Surface Engineering*, 28(8):564–568, 2012. ISSN 0267-0844. doi: 10.1179/1743294412Y.0000000029.
- [140] Charles S. Montross, Tao Wei, Lin Ye, Graham Clark, and Yiu-Wing Mai. Laser shock processing and its effects on microstructure and properties of metal alloys: a review. *International Journal of Fatigue*, 24, 2002.
- [141] Xiao-Dong Liu, De-Guang Shang, Ming Li, Jia Jin, Tao Chen, Y.B. Guo, and M.E. Barkey. Healing fatigue damage by laser shock peening for copper film. *International Journal of Fatigue*, 54:127–132, 2013. ISSN 0142-1123. doi: <https://doi.org/10.1016/j.ijfatigue.2013.03.013>.
- [142] J. Z. Lu, K. Y. Luo, Y. K. Zhang, G. F. Sun, Y. Y. Gu, J. Z. Zhou, X. D. Ren, X. C. Zhang, L. F. Zhang, K. M. Chen, C. Y. Cui, Y. F. Jiang, A. X. Feng, and L. Zhang. Grain refinement mechanism of multiple laser shock processing impacts on ansi 304 stainless steel. *Acta Materialia*, 58(16):5354–5362, 2010. ISSN 13596454. doi: 10.1016/j.actamat.2010.06.010.
- [143] I. Altenberger, E. A. Stach, G. Liu, R. K. Nalla, and R. O. Ritchie. An in situ transmission electron microscope study of the thermal stability of near-surface microstructures induced by deep rolling and laser-shock peening. *Scripta Materialia*, 48(12):1593–1598, 2003. ISSN 13596462. doi: 10.1016/s1359-6462(03)00143-x.
- [144] Igor Altenberger, Ravi K. Nalla, Yuji Sano, Lothar Wagner, and Robert O. Ritchie. On the effect of deep-rolling and laser-peening on the stress-controlled low- and high-cycle fatigue behavior of ti-6al-4v at elevated temperatures up to

- 550°C. *International Journal of Fatigue*, 44:292–302, 2012. ISSN 01421123. doi: 10.1016/j.ijfatigue.2012.03.008.
- [145] Binod Dhakal and S. Swaroop. Effect of laser shock peening on mechanical and microstructural aspects of 6061-t6 aluminum alloy. *Journal of Materials Processing Technology*, 282, 2020. ISSN 09240136. doi: 10.1016/j.jmatprotec.2020.116640.
- [146] K. Buchanan, K. Colas, J. Ribis, A. Lopez, and J. Garnier. Analysis of the metastable precipitates in peak-hardness aged al-mg-si(-cu) alloys with differing si contents. *Acta Materialia*, 132:209–221, 2017. ISSN 1359-6454. doi: <https://doi.org/10.1016/j.actamat.2017.04.037>.
- [147] Micheal Kattoura, Seetha Ramaiah Mannava, Dong Qian, and Vijay K. Vasudevan. Effect of laser shock peening on elevated temperature residual stress, microstructure and fatigue behavior of ati 718plus alloy. *International Journal of Fatigue*, 104:366–378, 2017. ISSN 01421123. doi: 10.1016/j.ijfatigue.2017.08.006.
- [148] Prevey, Hornbach, and Mason. Thermal residual stress relaxation and distortion in surface enhanced gas turbine components. *Proceedings of the 17th Heat Treating Society Conference and 1st International Induction Heat Treating Symposium*, 1998.
- [149] Prevey. The effect of cold work on the thermal stability of residual compression in surface enhanced in718. *20th ASM heat treating society conference proceedings*, 2000.
- [150] Eigenmann, Schulze, and Vohringer. Surface residual stress relaxation in steels by thermal or mechanical treatment. 1984.
- [151] Amrinder Gill, Abhishek Telang, S. R. Mannava, Dong Qian, Young-Shik Pyoun, Hitoshi Soyama, and Vijay K. Vasudevan. Comparison of mechanisms of advanced mechanical surface treatments in nickel-based superalloy. *Materials Science and Engineering: A*, 576:346–355, 2013. ISSN 09215093. doi: 10.1016/j.msea.2013.04.021.
- [152] Micheal Kattoura, Seetha Ramaiah Mannava, Dong Qian, and Vijay K. Vasudevan. Effect of laser shock peening on residual stress, microstructure and fatigue behavior of ati 718plus alloy. *International Journal of Fatigue*, 102:121–134, 2017. ISSN 01421123. doi: 10.1016/j.ijfatigue.2017.04.016.
- [153] N. Navin Kumar, Aditya Chandrakant Yadav, K. Raja, C. D. Naiju, S. Prabhakaran, and S. Kalainathan. Laser shock peening on al-si10-mg produced by dmils technique. *Materials Today: Proceedings*, 22:2916–2925, 2020. ISSN 22147853. doi: 10.1016/j.matpr.2020.03.425.

- [154] Nikola Kalentics, Manuel Ortega Varela de Seijas, Seth Griffiths, Christian Leinenbach, and Roland E. Logé. 3d laser shock peening – a new method for improving fatigue properties of selective laser melted parts. *Additive Manufacturing*, 33, 2020. ISSN 22148604. doi: 10.1016/j.addma.2020.101112.
- [155] Sihai Luo, Weifeng He, Kai Chen, Xiangfan Nie, Liucheng Zhou, and Yiming Li. Regain the fatigue strength of laser additive manufactured ti alloy via laser shock peening. *Journal of Alloys and Compounds*, 750:626–635, 2018. ISSN 0925-8388. doi: <https://doi.org/10.1016/j.jallcom.2018.04.029>.
- [156] Nikola Kalentics, Eric Boillat, Patrice Peyre, Snežana Ćirić Kostić, Nebojša Bogojević, and Roland E. Logé. Tailoring residual stress profile of selective laser melted parts by laser shock peening. *Additive Manufacturing*, 16:90–97, 2017. ISSN 22148604. doi: 10.1016/j.addma.2017.05.008.
- [157] Sean Gribbin, Jonathan Bicknell, Luke Jorgensen, Igor Tsukrov, and Marko Knezevic. Low cycle fatigue behavior of direct metal laser sintered inconel alloy 718. *International Journal of Fatigue*, 93:156–167, 2016. ISSN 01421123. doi: 10.1016/j.ijfatigue.2016.08.019.
- [158] Z. Song, W. Gao, D. Wang, Z. Wu, M. Yan, L. Huang, and X. Zhang. Very-high-cycle fatigue behavior of inconel 718 alloy fabricated by selective laser melting at elevated temperature. *Materials (Basel)*, 14(4), 2021. ISSN 1996-1944 (Print) 1996-1944 (Linking). doi: 10.3390/ma14041001.
- [159] Mark Basham, Jacob Filik, Michael T. Wharmby, Peter C. Y. Chang, Baha El Kassaby, Matthew Gerring, Jun Aishima, Karl Levik, Bill C. A. Pulford, Irakli Sikharulidze, Duncan Sneddon, Matthew Webber, Sarnjeet S. Dhesi, Francesco Maccherozzi, Olof Svensson, Sandor Brockhauser, Gabor Naray, and Alun W. Ashton. Data analysis workbench (dawn). *Journal of Synchrotron Radiation*, 22(3):853–858, 2015. ISSN 1600-5775. doi: 10.1107/S1600577515002283.
- [160] J. Filik, A. W. Ashton, P. C. Y. Chang, P. A. Chater, S. J. Day, M. Drakopoulos, M. W. Gerring, M. L. Hart, O. V. Magdysyuk, S. Michalik, A. Smith, C. C. Tang, N. J. Terrill, M. T. Wharmby, and H. Wilhelm. Processing two-dimensional x-ray diffraction and small-angle scattering data in dawn 2. *Journal of Applied Crystallography*, 50(3):959–966, 2017. ISSN 1600-5767. doi: 10.1107/S1600576717004708.
- [161] H. J. Stone, T. M. Holden, and R. C. Reed. Determination of the plane specific elastic constants of waspaloy using neutron diffraction. *Scripta Materialia*, 40(3):

- 353–358, 1999. ISSN 1359-6462. doi: [https://doi.org/10.1016/S1359-6462\(98\)00437-0](https://doi.org/10.1016/S1359-6462(98)00437-0).
- [162] Jan Hönnige, Cui Er Seow, Supriyo Ganguly, Xiangfang Xu, Sandra Cabeza, Harry Coules, and Stewart Williams. Study of residual stress and microstructural evolution in as-deposited and inter-pass rolled wire plus arc additively manufactured inconel 718 alloy after ageing treatment. *Materials Science and Engineering: A*, 801:140368, 2021. ISSN 0921-5093. doi: <https://doi.org/10.1016/j.msea.2020.140368>.
- [163] ISO 21432:2019. Non-destructive testing — Standard test method for determining residual stresses by neutron diffraction. Standard, International Organization for Standardization, Geneva, CH, 2019.
- [164] W. L. Bragg. The diffraction of short electromagnetic waves by a crystal. *Scientia*, 23(45), 1929.
- [165] *Stress Measurement*, pages 271–356. 2018. doi: <https://doi.org/10.1002/9781119356080.ch9>.
- [166] P. E. Aba-Perea, T. Pirling, P. J. Withers, J. Kelleher, S. Kabra, and M. Preuss. Determination of the high temperature elastic properties and diffraction elastic constants of ni-base superalloys. *Materials & Design*, 89:856–863, 2016. ISSN 0264-1275. doi: <https://doi.org/10.1016/j.matdes.2015.09.152>.
- [167] Rafael Barros, Francisco J. G. Silva, Ronny M. Gouveia, Abdollah Saboori, Giulio Marchese, Sara Biamino, Alessandro Salmi, and Eleonora Atzeni. Laser powder bed fusion of inconel 718: Residual stress analysis before and after heat treatment. *Metals*, 9(12):1290, 2019. ISSN 2075-4701.
- [168] D. J. Hughes and Z. Chen. High resolution near-surface stress determination using synchrotron x-rays. *Nuclear Instruments and Methods in Physics Research Section B: Beam Interactions with Materials and Atoms*, 238(1):214–218, 2005. ISSN 0168-583X. doi: <https://doi.org/10.1016/j.nimb.2005.06.051>.
- [169] Ranggi S. Ramadhan, Abdul K. Syed, Anton S. Tremsin, Winfried Kockelmann, Robert Dalglish, Bo Chen, David Parfitt, and Michael E. Fitzpatrick. Mapping residual strain induced by cold working and by laser shock peening using neutron transmission spectroscopy. *Materials & Design*, 143:56–64, 2018. ISSN 0264-1275. doi: <https://doi.org/10.1016/j.matdes.2018.01.054>.
- [170] John R. Taylor. *An introduction to error analysis*. University Science Books, Sausalito, Calif., 1997. ISBN 093570275X 9780935702750 0935702423 9780935702422.

- [171] W. Kraus and G. Nolze. Powder cell - a program for the representation and manipulation of crystal structures and calculation of the resulting x-ray powder patterns. *Journal of Applied Crystallography*, 29(3):301–303, 1996. doi: 10.1107/S0021889895014920.
- [172] Rafael Menezes Nunes, Daniel Pereira, Thomas Clarke, and Thomas Karl Hirsch. Delta phase characterization in inconel 718 alloys through x-ray diffraction. *ISIJ International*, 55(11):2450–2454, 2015. doi: 10.2355/isijinternational.ISIJINT-2015-111.
- [173] P. Sudharshan Phani and W.C. Oliver. A critical assessment of the effect of indentation spacing on the measurement of hardness and modulus using instrumented indentation testing. *Materials Design*, 164:107563, 2019. ISSN 0264-1275.
- [174] R. B. Rebak. *7 - Stress corrosion cracking (SCC) of nickel-based alloys*, pages 273–306. Woodhead Publishing, 2011. ISBN 978-1-84569-673-3. doi: <https://doi.org/10.1533/9780857093769.3.273>.
- [175] W. Cao, M. Khadhraoui, B. Brenier, J. Y. Guédou, and L. Castex. Thermomechanical relaxation of residual stress in shot peened nickel base superalloy. *Materials Science and Technology (United Kingdom)*, 10(11):947–954, 1994. doi: 10.1179/mst.1994.10.11.947.
- [176] A. Evans, S. B. Kim, J. Shackleton, G. Bruno, M. Preuss, and P. J. Withers. Relaxation of residual stress in shot peened udimet 720li under high temperature isothermal fatigue. *International Journal of Fatigue*, 27(10):1530–1534, 2005. ISSN 0142-1123. doi: <https://doi.org/10.1016/j.ijfatigue.2005.07.027>.
- [177] He Liu, Jianzhong Sun, Shiyong Lei, and Shungang Ning. In-service aircraft engines turbine blades life prediction based on multi-modal operation and maintenance data. *Propulsion and Power Research*, 2021. ISSN 2212-540X. doi: <https://doi.org/10.1016/j.jprr.2021.09.001>.
- [178] Xing Li, J.J. Shi, C.H. Wang, G.H. Cao, A.M. Russell, Z.J. Zhou, C.P. Li, and G.F. Chen. Effect of heat treatment on microstructure evolution of inconel 718 alloy fabricated by selective laser melting. *Journal of Alloys and Compounds*, 764: 639–649, 2018. ISSN 0925-8388. doi: <https://doi.org/10.1016/j.jallcom.2018.06.112>.
- [179] D.A. Lesyk, S. Martinez, B.N. Mordyuk, O.O. Pedash, V.V. Dzhemelinskyi, and . Lamikiz. Ultrasonic surface post-processing of hot isostatic pressed

- and heat treated superalloy parts manufactured by laser powder bed fusion. *Additive Manufacturing Letters*, 3:100063, 2022. ISSN 2772-3690. doi: <https://doi.org/10.1016/j.addlet.2022.100063>.
- [180] D. Karthik and S. Swaroop. Laser shock peening enhanced corrosion properties in a nickel based inconel 600 superalloy. *Journal of Alloys and Compounds*, 694:1309–1319, 2017. ISSN 0925-8388. doi: <https://doi.org/10.1016/j.jallcom.2016.10.093>.
- [181] Dennise Ardi, Wang Wei, Iain Berment-Parr, Goetz Feldmann, Ampara Aramcharoen, and Chow Wong. *Investigations of the Residual Stresses and Surface Integrity Generated by a Novel Mechanical Surface Strengthening*. 2016. doi: [10.21741/9781945291173-53](https://doi.org/10.21741/9781945291173-53).
- [182] Ching K. Yong, Gregory J. Gibbons, Chow C. Wong, and Geoff West. A critical review of the material characteristics of additive manufactured in718 for high-temperature application. *Metals*, 10(12), 2020. ISSN 2075-4701. doi: [10.3390/met10121576](https://doi.org/10.3390/met10121576).
- [183] M. Vashista and S. Paul. Correlation between full width at half maximum (fwhm) of xrd peak with residual stress on ground surfaces. *Philosophical Magazine*, 92(33): 4194–4204, 2012. ISSN 1478-6435. doi: [10.1080/14786435.2012.704429](https://doi.org/10.1080/14786435.2012.704429).
- [184] X. Li, J.J. Shi, G.H. Cao, A.M. Russell, Z.J. Zhou, C.P. Li, and G.F. Chen. Improved plasticity of inconel 718 superalloy fabricated by selective laser melting through a novel heat treatment process. *Materials Design*, 180:107915, 2019. ISSN 0264-1275. doi: <https://doi.org/10.1016/j.matdes.2019.107915>.
- [185] Jian Wang and Xinghang Zhang. Twinning effects on strength and plasticity of metallic materials. *MRS Bulletin*, 41(4):274–281, 2016. ISSN 1938-1425. doi: [10.1557/mrs.2016.67](https://doi.org/10.1557/mrs.2016.67).
- [186] Nathalie Bozzolo S. Allain M. Humbert David Barbier, N. Gey. Ebsd for analysing the twinning microstructure in fine-grained twip steels and its influence on work hardening. *Journal of Microscopy*, 2009.
- [187] Amrinder S. Gill, Abhishek Telang, Chang Ye, S. R. Mannava, Dong Qian, and Vijay K. Vasudevan. Localized plastic deformation and hardening in laser shock peened inconel alloy 718spf. *Materials Characterization*, 142:15–26, 2018. ISSN 1044-5803. doi: <https://doi.org/10.1016/j.matchar.2018.05.010>.

- [188] Oleg Mishin, Andrew Godfrey, and Dorte Jensen. Analysis of deformation structures in fcc materials using ebsd and tem techniques. *Electron Backscatter Diffraction in Materials Science*, pages 263–275, 03 2010. doi: 10.1007/978-0-387-88136-2_19.
- [189] Masayuki Kamaya, Yohei Sakakibara, Rika Yoda, Seiichi Suzuki, Hirobumi Morita, Daisuke Kobayashi, Kenta Yamagiwa, Tomoya Nishioka, Yuya Maekawa, Tempei Tanakamaru, Hikaru Nagashima, and Toshihiro Ohtani. A round robin ebsd measurement for quantitative assessment of small plastic strain. *Materials Characterization*, 170:110662, 2020. ISSN 1044-5803. doi: <https://doi.org/10.1016/j.matchar.2020.110662>.
- [190] Steven J. Lainé, Kevin M. Knowles, Phillip J. Doorbar, Richard D. Cutts, and David Rugg. Microstructural characterisation of metallic shot peened and laser shock peened ti–6al–4v. *Acta Materialia*, 123:350–361, 2017. ISSN 1359-6454. doi: <https://doi.org/10.1016/j.actamat.2016.10.044>.
- [191] George T. (Rusty) Gray. High-strain-rate deformation: Mechanical behavior and deformation substructures induced. *Annual Review of Materials Research*, 42(1): 285–303, 2012.
- [192] Eslam Fayed, Mohammad Saadati, Davood Shahriari, V. Brailovski, Mohammad Jahazi, and Mamoun Medraj. Effect of homogenization and solution treatments time on the elevated-temperature mechanical behavior of inconel 718 fabricated by laser powder bed fusion. *Scientific Reports*, 11, 2021. doi: 10.1038/s41598-021-81618-5.
- [193] Amrinder S. Gill, Abhishek Telang, and Vijay K. Vasudevan. Characteristics of surface layers formed on inconel 718 by laser shock peening with and without a protective coating. *Journal of Materials Processing Technology*, 225:463–472, 2015. ISSN 0924-0136. doi: <https://doi.org/10.1016/j.jmatprotec.2015.06.026>.
- [194] Peyre, Fabbro, Merrien, and Lieurade. Laser shock processing of aluminium alloys. application to high cycle fatigue behaviour. *Materials Science and Engineering: A*, 1996.
- [195] X. C. Zhang, Y. K. Zhang, J. Z. Lu, F. Z. Xuan, Z. D. Wang, and S. T. Tu. Improvement of fatigue life of ti–6al–4v alloy by laser shock peening. *Materials Science and Engineering: A*, 527(15):3411–3415, 2010. ISSN 0921-5093. doi: <https://doi.org/10.1016/j.msea.2010.01.076>.

- [196] L. Wagner. Mechanical surface treatments on titanium, aluminum and magnesium alloys. *Materials Science and Engineering: A*, 263(2):210–216, 1999. ISSN 0921-5093. doi: [https://doi.org/10.1016/S0921-5093\(98\)01168-X](https://doi.org/10.1016/S0921-5093(98)01168-X).
- [197] Zhong Zhou, Amrinder S. Gill, Dong Qian, S. R. Mannava, Kristina Langer, Youhai Wen, and Vijay K. Vasudevan. A finite element study of thermal relaxation of residual stress in laser shock peened in718 superalloy. *International Journal of Impact Engineering*, 38(7):590–596, 2011. ISSN 0734-743X. doi: <https://doi.org/10.1016/j.ijimpeng.2011.02.006>.
- [198] Dennis J. Buchanan, Reji John, and Robert A. Brockman. Relaxation of shot-peened residual stresses under creep loading. *Journal of Engineering Materials and Technology*, 131(3), 2009. ISSN 0094-4289. doi: 10.1115/1.3120393.
- [199] P. Prév y. The measurement of subsurface residual stress and cold work distributions in nickel base alloys.
- [200] Wyman Z. Zhuang and Gary R. Halford. Investigation of residual stress relaxation under cyclic load. *International Journal of Fatigue*, 23:31–37, 2001. ISSN 0142-1123. doi: [https://doi.org/10.1016/S0142-1123\(01\)00132-3](https://doi.org/10.1016/S0142-1123(01)00132-3).
- [201] Kai Siang Chin, Idapalapati Sridhar, Anna Paradowska, Mark Reid, Shashwat Shukla, and Dennise Ardi. *Mechanical Stress Relaxation of a Laser Peened and Shot Peened Ni-Based Superalloy*, pages 182–189. 2020. ISBN 978-981-15-0053-4.
- [202] Carlos Rubio-Gonz lez, Garnica-Guzm n A, and Gilberto Gomez-Rosas. Relaxation of residual stresses induced by laser shock processing. *Revista Mexicana de F sica*, 55, 2009.
- [203] Giuseppe Statti, Ali Mehmanparast, Romali Biswal, and Cesare Mario Rizzo. Evaluation of cyclic loading effects on residual stress relaxation in offshore wind welded structures. *Journal of Multiscale Modelling*, 12, 2021. URL <https://doi.org/10.1142/S1756973721500050>.
- [204] Zhang-Jie Wang, Qing-Jie Li, Yi-Nan Cui, Zhan-Li Liu, Evan Ma, Ju Li, Jun Sun, Zhuo Zhuang, Ming Dao, Zhi-Wei Shan, and Subra Suresh. Cyclic deformation leads to defect healing and strengthening of small-volume metal crystals. *Proceedings of the National Academy of Sciences of the United States of America*, 112(44):13502–13507, 2015. doi: 10.1073/pnas.1518200112.

- [205] Z. W. Shan, Raja K. Mishra, S. A. Syed Asif, Oden L. Warren, and Andrew M. Minor. Mechanical annealing and source-limited deformation in submicrometre-diameter ni crystals. *Nature Materials*, 7(2):115–119, 2008. ISSN 1476-4660. doi: 10.1038/nmat2085.
- [206] A. Röttger, J. Boes, W. Theisen, M. Thiele, C. Esen, A. Edelmann, and R. Hellmann. Microstructure and mechanical properties of 316l austenitic stainless steel processed by different slm devices. *The International Journal of Advanced Manufacturing Technology*, 108(3):769–783, 2020. ISSN 1433-3015. doi: 10.1007/s00170-020-05371-1.
- [207] Ching Kiat Yong, Geoff D. West, Greg J. Gibbons, and Chow Cher Wong. Influence of laser shock peening (lsp) on the material properties of additive manufactured in718. In Sho Itoh and Shashwat Shukla, editors, *Advanced Surface Enhancement*, pages 305–313. Springer Singapore. ISBN 978-981-15-0054-1.
- [208] Yong Wang, Xiaoyu Pan, Xibin Wang, Zhibing Liu, Shuyao Liu, Wenjuan Wan, and Puyi Wang. Influence of laser shock peening on surface integrity and tensile property of high strength low alloy steel. *Chinese Journal of Aeronautics*, 34(6): 199–208, 2021. ISSN 1000-9361. doi: <https://doi.org/10.1016/j.cja.2020.09.004>.
- [209] E. J. Pavlina and C. J. Van Tyne. Correlation of yield strength and tensile strength with hardness for steels. *Journal of Materials Engineering and Performance*, 17(6): 888–893, 2008. ISSN 1544-1024. doi: 10.1007/s11665-008-9225-5.
- [210] E. I. Galindo-Nava and P. E. J. Rivera-Díaz-Del-Castillo. Understanding the factors controlling the hardness in martensitic steels. *Scripta Materialia*, 110:96–100, 2016. doi: 10.1016/j.scriptamat.2015.08.010.
- [211] M. Tiryakioğlu, J. S. Robinson, M. A. Salazar-Guapuriche, Y. Y. Zhao, and P. D. Eason. Hardness-strength relationships in the aluminum alloy 7010. *Materials Science and Engineering A*, 631:196–200, 2015. doi: 10.1016/j.msea.2015.02.049.
- [212] M. L. Zhu and F. Z. Xuan. Correlation between microstructure, hardness and strength in haz of dissimilar welds of rotor steels. *Materials Science and Engineering A*, 527(16-17):4035–4042, 2010. doi: 10.1016/j.msea.2010.03.066.
- [213] Allan Clauer and John Koucky. Laser shock processing increases the fatigue life of metal parts. *Materials and Processing Report*, 6(6):3–5, 1991. ISSN 0887-1949. doi: 10.1080/08871949.1991.11752452.

- [214] M. J. Leap, J. Rankin, J. Harrison, L. Hackel, J. Nemeth, and J. Candela. Effects of laser peening on fatigue life in an arrestment hook shank application for naval aircraft. *International Journal of Fatigue*, 33(6):788–799, 2011. ISSN 01421123. doi: 10.1016/j.ijfatigue.2010.12.016.
- [215] Jie Sheng, Hang Zhang, Xiaoqi Hu, and Shu Huang. Influence of laser peening on the high-temperature fatigue life and fracture of inconel 718 nickel-based alloy. *Theoretical and Applied Fracture Mechanics*, 109:102757, 2020. ISSN 0167-8442. doi: <https://doi.org/10.1016/j.tafmec.2020.102757>.
- [216] Niloofar Sanaei and Ali Fatemi. Analysis of the effect of surface roughness on fatigue performance of powder bed fusion additive manufactured metals. *Theoretical and Applied Fracture Mechanics*, 108:102638, 2020. ISSN 0167-8442. doi: <https://doi.org/10.1016/j.tafmec.2020.102638>.
- [217] Chuanli Yu, Zhiyong Huang, Zian Zhang, Jiebin Shen, Jian Wang, and Zhiping Xu. Influence of post-processing on very high cycle fatigue resistance of inconel 718 obtained with laser powder bed fusion. *International Journal of Fatigue*, 153:106510, 2021. ISSN 0142-1123. doi: <https://doi.org/10.1016/j.ijfatigue.2021.106510>.
- [218] David B. Witkin, Thomas V. Albright, and Dhruv N. Patel. Empirical approach to understanding the fatigue behavior of metals made using additive manufacturing. *Metallurgical and Materials Transactions A*, 47(8):3823–3836, 2016. ISSN 1543-1940. doi: 10.1007/s11661-016-3501-z.
- [219] Eric Wycisk, Andreas Solbach, Shafaqat Siddique, Dirk Herzog, Frank Walther, and Claus Emmelmann. Effects of defects in laser additive manufactured ti-6al-4v on fatigue properties. *Physics Procedia*, 56:371–378, 2014. ISSN 1875-3892. doi: <https://doi.org/10.1016/j.phpro.2014.08.120>.
- [220] A.G. Sanchez, C. You, M. Leering, D. Glaser, D. Furfari, M.E. Fitzpatrick, J. Whar-ton, and P.A.S. Reed. Effects of laser shock peening on the mechanisms of fatigue short crack initiation and propagation of aa7075-t651. *International Journal of Fatigue*, 143:106025, 2021. ISSN 0142-1123.
- [221] J.C. Newman, E.P. Phillips, and M.H. Swain. Fatigue-life prediction methodology using small-crack theory. *International Journal of Fatigue*, 21(2):109–119, 1999. ISSN 0142-1123.
- [222] Zelin Chen, Zihao Dong, Chang Liu, Yajun Dai, and Chao He. Characterization on crack initiation and early propagation region of Nickel-Based alloys in very high cycle fatigue. *Materials (Basel)*, 15(17), August 2022.

- [223] Arun Sundar Sundaram Singaravelu, Jason J. Williams, Harsh Dev Goyal, Sridhar Niverty, Sudhanshu S. Singh, Tyler J. Stannard, Xianghui Xiao, and Nikhilesh Chawla. 3d time-resolved observations of fatigue crack initiation and growth from corrosion pits in al 7xxx alloys using in situ synchrotron x-ray tomography. *Metallurgical and Materials Transactions A*, 51(1):28–41, Jan 2020.

Appendix A

EOS IN718 material specifications

Material data sheet

EOS NickelAlloy IN718

EOS NickelAlloy IN718 is a heat and corrosion resistant nickel alloy powder which has been optimized especially for processing on EOS M systems.

This document provides information and data for parts built using EOS NickelAlloy IN718 powder (EOS art.-no. 9011-0020) on the following system specifications:

- EOSINT M280 400W System with PSW3.6 and Parameter Set IN718_Performance 1.0
- EOS M290 400W System with EOSPRINT 1.0 and Parameter Set IN718_Performance 1.0

Description

Parts built from EOS NickelAlloy IN718 have chemical composition corresponding to UNS N07718, AMS 5662, AMS 5664, W.Nr 2.4668, DIN NiCr19Fe19NbMo3. This kind of precipitation-hardening nickel-chromium alloy is characterized by having good tensile, fatigue, creep and rupture strength at temperatures up to 700 °C (1290 °F).

This material is ideal for many high temperature applications such as gas turbine parts, instrumentation parts, power and process industry parts etc. It also has excellent potential for cryogenic applications.

Parts built from EOS NickelAlloy IN718 can be easily post-hardened by precipitation-hardening heat treatments. In both as-built and age-hardened states the parts can be machined, spark-eroded, welded, micro shot-peened, polished and coated if required. Due to the layerwise building method, the parts have a certain anisotropy - see Technical Data for examples.

Material data sheet

Technical data

General process data

| | |
|--|--|
| Typical achievable part accuracy [1], [11] | |
| - small parts | approx. $\pm 40 - 60 \mu\text{m}$ approx. $\pm 1.6 - 2.4 \times 10^{-3}$ inch |
| - large parts | $\pm 0.2 \%$ |
| Min. wall thickness [2], [11] | |
| | typ. $0.3 - 0.4 \text{ mm}$ typ. $0.012 - 0.016$ inch |
| Surface roughness [3], [11] | |
| - after shot-peening | $R_a 4 - 6.5 \mu\text{m}$, $R_z 20 - 50 \mu\text{m}$ $R_a 0.16 - 0.25 \times 10^{-3}$ inch, $R_z 0.78 - 1.97 \times 10^{-3}$ inch |
| - after polishing | R_z up to $< 0.5 \mu\text{m}$ R_z up to $< 0.02 \times 10^{-3}$ inch (can be very finely polished) |
| Volume rate [4] | |
| - Parameter Set IN718_Performance ($40 \mu\text{m}$) | $4 \text{ mm}^3/\text{s}$ ($14.4 \text{ cm}^3/\text{h}$) $0.88 \text{ in}^3/\text{h}$ |

[1] Based on users' experience of dimensional accuracy for typical geometries, e.g. $\pm 40 \mu\text{m}$ (1.6×10^{-3} inch) when parameters can be optimized for a certain class of parts or $\pm 60 \mu\text{m}$ (2.4×10^{-3} inch) when building a new kind of geometry for the first time. Part accuracy is subject to appropriate data preparation and post-processing, in accordance with EOS training.

[2] Mechanical stability is dependent on geometry (wall height etc.) and application#

[3] Due to the layerwise building, the surface structure depends strongly on the orientation of the surface, for example sloping and curved surfaces exhibit a stair-step effect. The values also depend on the measurement method used. The values quoted here given an indication of what can be expected for horizontal (up-facing) or vertical surfaces.

[4] Volume rate is a measure of build speed during laser exposure. The total build speed depends on the average volume rate, the recoating time (related to the number of layers) and other factors such as DMLS-Start settings.

Material data sheet

Physical and chemical properties of parts

| | |
|----------------------|---|
| Material composition | Ni (50 - 55 wt-%) Cr (17.0 - 21.0 wt-%) Nb (4.75 - 5.5 wt-%) Mo (2.8 - 3.3 wt-%) Ti (0.65 - 1.15 wt-%) Al (0.20 - 0.80 wt-%) Co (≤ 1.0 wt-%) Cu (≤ 0.3 wt-%) C (≤ 0.08 wt-%) Si, Mn (each ≤ 0.35 wt-%) P, S (each ≤ 0.015 wt-%) B (≤ 0.006 wt-%) Fe (balance) |
| Relative density | approx. 100 % |
| Density | min. 8.15 g/cm ³ min. 0.294 lb/in ³ |

Material data sheet

Mechanical properties of parts at 20 °C (68 °F)

| | As built | Heat treated per AMS 5662 [5] | Heat treated per AMS 5664 [6] |
|--------------------------------------|-------------------------------------|--|--|
| Tensile strength [7] | | | |
| - in horizontal direction (XY) | typ. 1060 ± 50 MPa (154 ± 7 ksi) | | |
| - in vertical direction (Z) | typ. 980 ± 50 MPa (142 ± 7 ksi) | min. 1241 MPa (180 ksi) typ. 1400 ± 100 MPa (203 ± 15 ksi) | min. 1241 MPa (180 ksi) typ. 1380 ± 100 MPa (200 ± 15 ksi) |
| Yield strength (Rp 0.2 %) [7] | | | |
| - in horizontal direction (XY) | typ. 780 ± 50 MPa (113 ± 7 ksi) | | |
| - in vertical direction (Z) | typ. 634 ± 50 MPa (92 ± 7 ksi) | min. 1034 MPa (150 ksi) typ. 1150 ± 100 MPa (167 ± 15 ksi) | min. 1034 MPa (150 ksi) typ. 1240 ± 100 MPa (180 ± 15 ksi) |
| Elongation at break [7] | | | |
| - in horizontal direction (XY) | typ. (27 ± 5) % | | |
| - in vertical direction (Z) | typ. (31 ± 5) % | min. 12 % typ. (15 ± 3) % | min. 12 % typ. (18 ± 5) % |
| Modulus of elasticity [7] | | | |
| - in horizontal direction (XY) | typ. 160 ± 20 GPa (23 ± 3 Msi) | | |
| - in vertical direction (Z) | | 170 ± 20 GPa 24.7 ± 3 Msi | 170 ± 20 GPa 24.7 ± 3 Msi |
| Hardness [8] | | | |
| | approx. 30 HRC approx. 287 HB | approx. 47 HRC approx. 446 HB | approx. 43 HRC approx. 400 HB |

[5] Heat treatment procedure per AMS 5662:

1. *Solution Anneal* at 980 °C (1800 °F) for 1 hour, air (Argon) cool.
2. *Ageing treatment*; hold at 720 °C (1330 °F) 8 hours, furnace cool to 620 °C (1150 °F) in 2 hours, hold at 620 °C (1150 °F) 8 hours, air (Argon) cool.

Material data sheet

- [6] Heat treatment procedure per AMS 5664:
 - 1. *Solution Anneal* at 1065 °C (1950 °F) for 1 hour, air (/argon) cool.
 - 2. *Ageing treatment*; hold at 760 °C (1400 °F) 10 hours, furnace cool to 650 °C (1200 °F) in 2 hours, hold at 650 °C (1200 °F) 8 hours, air (/argon) cool
- [7] Tensile testing according to ISO 6892-1:2009 (B) Annex D, proportional test pieces, diameter of the neck area 5 mm (0.2 inch) , original gauge length 25 mm (1 inch).
- [8] Rockwell C (HRC) hardness measurement according to EN ISO 6508-1 on polished surface. Note that measured hardness can vary significantly depending on how the specimen has been prepared.

Material data sheet

Mechanical properties of parts at high temperature (649 °C, 1200 °F) [11]

| | Heat treated per AMS 5662 [5] | Heat treated per AMS 5664 [6] |
|--------------------------------|---|--|
| Tensile Strength (Rm) [9] | | |
| - in vertical direction (Z) | min. 965 MPa (140 ksi) typ. 1170 ± 50 MPa (170 ± 7 ksi) | typ. 1210 ± 50 MPa (175 ± 7 ksi) |
| Yield strength (Rp 0.2 %) [9] | | |
| - in vertical direction (Z) | min. 862 MPa (125 ksi) typ. 970 ± 50 MPa (141 ± 7 ksi) | typ. 1010 ± 50 MPa (146 ± 7 ksi) |
| Elongation at break [9] | | |
| - in vertical direction (Z) | min. 6 % typ. (16 ± 3) % | typ. (20 ± 3) % |
| Stress-Rupture Properties [10] | | |
| - in vertical direction (Z) | min. 23 hours at stress level 689 MPa (100 ksi) | |
| | 51 ± 5 hours (final applied stress to rupture 792.5 MPa / 115 ksi) | 81 ± 10 hours (final applied stress to rupture 861.5 MPa / 125 ksi) |

[9] Elevated temperature tensile testing at 649 °C (1200 °F) in accordance with EN 10002-5 (92)

[10] Testing at 649 °C (1200 °F) in accordance with ASTM E139 (2006), smooth specimens. Test method as described in AMS 5662 (3.5.1.2.3.3): "The load required to produce an initial axial stress of 689 MPa (100 ksi) shall be used to rupture or for 23 hours, whichever occurs first. After the 23 hours and at intervals of 8 hours minimum, thereafter, the stress shall be increased in increments of 34.5 MPa (5 ksi)."

[11] Hint: these properties were determined on an EOSINT M 270 IM Xtended and EOSINT M 280-400W. Test parts from following machine types EOSINT M 270 Dual Mode, EOSINT M 280-200W and EOS M 290-400W correspond with these data.

Material data sheet

Thermal properties of parts

| | Heat treated per AMS 5662 [4] |
|--|--|
| Coefficient of thermal expansion | |
| - over 25 - 200 °C (36 - 390 °F) | approx. 12.5 - 13.0 x 10 ⁻⁶ m/m°C approx. 6.9 - 7.2 x 10 ⁻⁶ in/in°F |
| - over 25 - 750 °C (36 - 930 °F) | approx. 16.6 - 17.2 x 10 ⁻⁶ m/m°C approx. 9.2 - 9.6 x 10 ⁻⁶ in/in°F |
| Maximum operating temperature for parts under load | approx. 650 °C approx. 1200 °F |
| Oxidation resistance up to [11] | approx. 980 °C approx. 1800 °F |

[12] Based on literature of conventional Ni-alloy with identical chemistry

Abbreviations

| | |
|---------|---------------|
| typ. | typical |
| min. | minimum |
| approx. | approximately |
| wt | weight |

Notes

The data are valid for the combinations of powder material, machine and parameter sets referred to on page 1, when used in accordance with the relevant Operating Instructions (including Installation Requirements and Maintenance) and Parameter Sheet. Part properties are measured using defined test procedures. Further details of the test procedures used by EOS are available on request.

The data correspond to our knowledge and experience at the time of publication. They do not on their own provide a sufficient basis for designing parts. Neither do they provide any agreement or guarantee about the specific properties of a part or the suitability of a part for a specific application. The producer or the purchaser of a part is responsible for checking the properties and the suitability of a part for a particular application. This also applies regarding any rights of protection as well as laws and regulations. The data are subject to change without notice as part of EOS' continuous development and improvement processes.

EOS[®], EOSINT[®] and DMLS[®] are registered trademarks of EOS GmbH.

© 2014 EOS GmbH – Electro Optical Systems. All rights reserved.

Appendix B

Powder composition

IMR TEST LABS

A Curtiss-Wright Business Unit
www.imrtest.com

IMR Test Labs - Singapore Pte Ltd
30 Loyang Way #03-16, Singapore 508769
T: +65.6592.5325 | F: +65.6592.5326
www.imrsingapore.sg
Co. Regn. No. 201101179E

12 August 2020

Yong Ching Kiat
A*STAR Research Entities
Advanced Remanufacturing
& Technology Centre
20 Biopolis Way
#08-01 Centros,
Singapore, 138668

TEST REPORT

IMR Report Number 202000831

PO Number
4700077403

Date Received
29 July 2020

Sample ID
IN718 Tumble RPM 15
30 mins Dry 80°C > 12h
Sieve 80 µm

SUMMARY

One sample was received for chemical analysis.

The results are on the following page(s).



Reviewed by



Cheryl Reano
Chemist

Reviewed by



Yusuf Apsoro
Technical Director

All procedures were performed in accordance with the IMR Quality Manual, current revision, and related procedures; and the PWA-MCL Manual F-23 and related procedures. The information contained in this test report represents only the material tested and may not be reproduced, except in full, without the written approval of IMR Test Labs – Singapore Pte Ltd (“IMR”). IMR maintains a quality system in compliance with the ISO/IEC 17025 and is accredited by the American Association for Laboratory Accreditation (A2LA), certificate #1140.10. IMR will perform all testing in good faith using the proper procedures, trained personnel, and equipment to accomplish the testing required. Conformance will be based on results without measurement uncertainty applied, unless otherwise requested by the customer. IMR’s liability to the customer or any third party is limited at all times to the amount charged for the services provided. All samples will be retained for a minimum of 3 months and may be destroyed thereafter unless otherwise specified by the customer. The recording of false, fictitious, or fraudulent statements or entries on this document may be punished as a felony under federal statutes. IMR Test Labs - Singapore is a GEAE S-400 approved lab (Supplier Code 69562).

CHEMISTRY

| Element | Sample |
|----------------|---------|
| C ¹ | 0.04 |
| Si | 0.02 |
| Mn | 0.02 |
| P | <0.01 |
| S ¹ | 0.002 |
| Cr | 18.98 |
| Mo | 3.07 |
| Cu | 0.02 |
| Co | 0.08 |
| Fe | 17.89 |
| Ti | 1.01 |
| Al | 0.50 |
| Nb | 5.22 |
| Ta | <0.01 |
| V | 0.02 |
| W | 0.01 |
| O ² | 0.024 |
| N ³ | 0.010 |
| Ni | Balance |

¹Determined by combustion- infrared absorbance

²Determined by inert gas fusion-infrared absorbance

³Determined by inert gas fusion-thermal conductivity

Results in weight percent unless otherwise indicated

Method(s): CSP-017 Rev. E (ICP-OES), ASTM E 1019-18 (Comb./IGF)

Appendix C

Python codes for lmfit

```

1 import os
2 import csv
3 import matplotlib.pyplot as plt
4 import pandas as pd
5 import numpy as np
6 from numpy import exp, loadtxt, pi, sqrt
7 import glob
8 import json
9 from lmfit import Model, Parameters, fit_report, minimize, Minimizer
10 from lmfit.models import GaussianModel, LinearModel, ConstantModel
11 os.chdir(r'C:\Users\kiat_y_c\Desktop\Warwick Main\Year 3\Synchrotron &
12 Neutron Experiments\SXRD Experiments\DIAMOND Round 1\MG27288\103423-
13 pilatus2M-files\103423_ascii') #working directory
14 filenames = glob.glob( '*dat' ) #use the .dat file that I have sent you
15
16 #function
17 for filename in filenames:
18     data = loadtxt(filename)
19     x = data[:, 0]
20     y = data[:, 1]
21
22     define_mod = GaussianModel (prefix='g1_')
23     line_mod = ConstantModel (prefix='line_')
24
25     pars = define_mod.guess(y, x=x)
26     pars += line_mod.guess (y, x=x)
27
28     mod = define_mod + line_mod
29
30     out = mod.fit(y, pars, x=x)
31
32     #writing the output to a csv file
33     #with open('report_'+filename+'.txt','w') as f:
34         #f.write(out.fit_report(min_correl=0.25))
35
36     #plotting the graph
37     plt.plot(x, y, '.')
38     plt.plot(x, out.best_fit, 'r', label='Best fit')
39
40     comps = out.eval_components()
41     plt.plot(x, comps['g1_'], 'b--', label='Gaussian component')
42     plt.axhline(comps ['line_'], label='Line component')
43     plt.legend(loc='best')
44     plt.savefig('figure_'+filename+'.jpg')
45     plt.clf()
46
47     y = json.loads(out.params.dumps())
48
49     x = pd.DataFrame(y['params'])
50
51     x.columns =
52     ['Attribute', 'Value', 'C', 'D', 'E', 'F', 'G', 'Error', 'I', 'J', 'K']
53
54     x = x.drop(columns = ['C', 'D', 'E', 'F', 'G', 'I', 'J', 'K'])
55
56     x_transposed = x.T

```

```
57
58 x_transposed = x_transposed.drop(x_transposed.index[0])
59
60 df = x_transposed
61 df2 = df.join(df.shift(-1).add_prefix('Error_'))
df2 = df2.drop(['Error'])

df2.to_csv(filename+'.csv')
```

Appendix D



Publication 1

Appendix E

Publication 2

Review

A Critical Review of the Material Characteristics of Additive Manufactured IN718 for High-Temperature Application

Ching Kiat Yong ^{1,*}, Gregory J. Gibbons ¹, Chow Cher Wong ² and Geoff West ¹

¹ Warwick Manufacturing Group (WMG), University of Warwick, Coventry CV4 7AL, UK; G.J.Gibbons@warwick.ac.uk (G.J.G.); G.West@warwick.ac.uk (G.W.)

² Advanced Remanufacturing and Technology Centre (ARTC), CleanTech Two, Singapore 637143, Singapore; wongcc@artc.a-star.edu.sg

* Correspondence: ching-kiat.yong@warwick.ac.uk; Tel.: +44-65-82000994

Received: 13 October 2020; Accepted: 10 November 2020; Published: 25 November 2020



Abstract: This paper reviews state of the art additive manufactured (AM) IN718 alloy intended for high-temperature applications. AM processes have been around for decades and have gained traction in the past five years due to the huge economic benefit this brings to manufacturers. It is crucial for the scientific community to look into AM IN718 applicability in order to see a step-change in production. Microstructural studies reveal that the grain structure plays a significant role in determining the fatigue lifespan of the material. Controlling IN718 respective phases such as the γ'' , δ and Laves phase is seen to be crucial. Literature reviews have shown that the mechanical properties of AM IN718 were very close to its wrought counterpart when treated appropriately. Higher homogenization temperature and longer ageing were recommended to dissolve the damaging phases. Various surface enhancement techniques were examined to find out their compatibility to AM IN718 alloy that is intended for high-temperature application. Laser shock peening (LSP) technology stands out due to the ability to impart low cold work which helps in containing the beneficial compressive residual stress it brings in a high-temperature fatigue environment.

Keywords: laser powder bed fusion; Inconel 718; high temperature; material characterisation; laser shock peening

1. Introduction

Additive manufacturing (AM) is a promising technology for fabricating a wide range of structures and complex geometries from three-dimensional (3D) model data. The process consists of depositing successive layers of material, one layer on top of another. AM was first developed by Chuck Hull in 1983, who established the process which was later known as stereolithography [1]. Designs are drawn using a computer-aided design (CAD) program which is then translated into model data. A 3D printer takes this data and slices it into several dimensional plans which instruct it where to deposit the layers of material. In 2015, the American Society of Testing and Materials (ASTM) issued a standard for AM technologies that consists of seven main processes [2], which established and defines the terms used in the field.

Alloys used for high-temperature application are highly sought after in the aerospace and nuclear industry due to their high strength and stability at extreme temperatures. Alloys that operate at high temperature are critical for these industries as the efficiency of fuel conversion is closely related to the operating temperature. Generally, these alloys are nickel-, iron- or cobalt-based. Their strength could sometimes become a weakness, as machining these alloys can be very difficult and expensive due to

the natural tendency for work hardening. The shift to AM technology has allowed manufacturers to produce complex geometries such as lattice structures [3,4], where traditional manufacturing such as casting or forging are a lot more time-consuming, or incapable of achieving these geometries.

This review paper aims to provide an overview of the AM of Inconel 718 (IN718), focusing on powder-bed fusion (PBF), which is one of the seven AM technologies. To the best of the authors' knowledge, a robust understanding of the fatigue response for AM IN718 in a high-temperature environment remains elusive. The literature review covers the current research gap and challenges encountered in adopting AM IN718 for commercial use. Microstructural development and mechanical performances of AM IN718 are the focus in this area. Effects such as build orientation and the AM thermal history are purposely left out as reviews in this area have been extensively done by the scientific community. Post-processing methods for AM IN718 are explored, as the scientific community sought out ways to push its usability for high-value applications [5–11].

2. Additive Manufacturing (AM)

2.1. Benefits of the AM Process

Researchers have made great efforts to understand the process–structure–property–performance relations of AM materials [12]. It is crucial to understand the consequence of each additional process that will impact the material's performance by altering its structure. Figure 1 illustrate a general material design chart with the intent to produce the optimal mechanical properties suited for its specific application. In the upcoming sections, material-specific heat treatment will be brought up frequently and the effect of IN718 material properties on its mechanical properties.

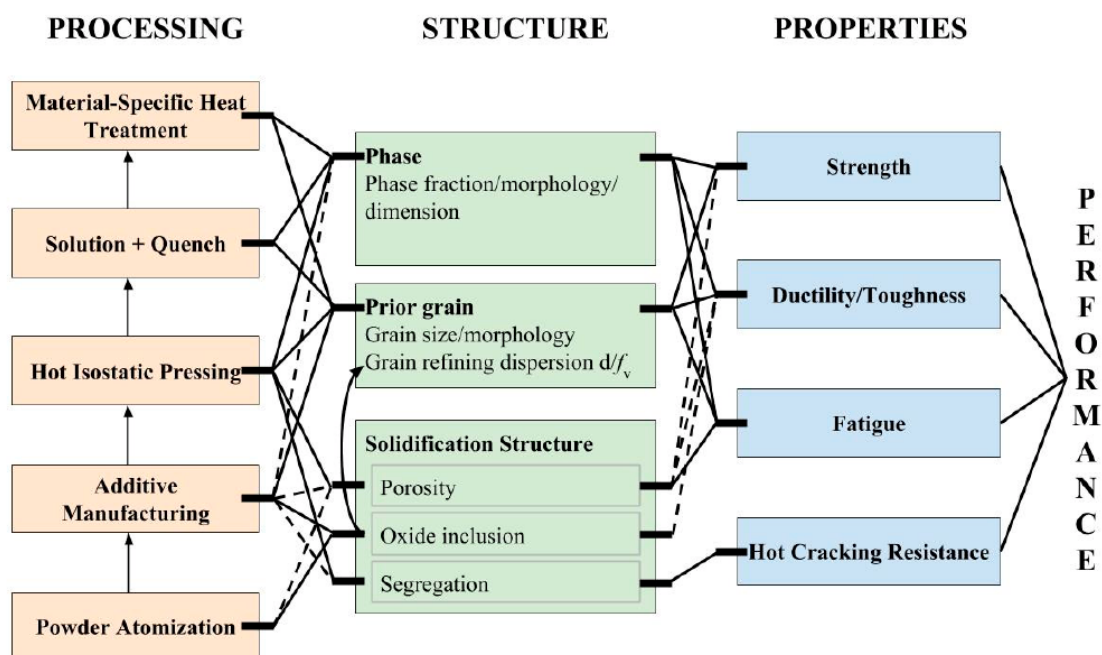


Figure 1. Material design chart that showcase the process–structure–properties–performance relationship for additive manufacturing (AM) metal alloy, provided by [13].

Reviews of the AM process have been compiled thoroughly by many authors [14–19]. Discussion on the impact of AM technology on different sectors have been brought up extensively by Ngo et al. [14], whereas author such as Saboori et al. decided to focus on the impact of AM titanium components on the manufacturing process. This section will focus on the seven technologies that were established by the ASTM community, and the benefits of each individual technology to give a broad overview

of the current AM landscape. Table 1 articulates the seven processes that were brought up by the various researchers.

Table 1. Description of the AM technologies and benefits associated with it [14,20–23].

| Technologies | Description | Benefits |
|--------------------------|--|---|
| Powder-Bed Fusion | Using a laser or electron beam to fuse thin layers of fine powders together, which are spread and closely packed on a platform. Subsequent layers of powders are applied on top of the previous layers until the final part is built | <ul style="list-style-type: none"> • Fine resolution High quality |
| Direct Energy Deposition | A nozzle mounted on a multi axis arm, which deposits melted material onto the substrate | <ul style="list-style-type: none"> • Suitable for reparation works • Good mechanical properties |
| Material Jetting | Droplets of material are deposited from the nozzle onto the platform, where it solidifies and subsequent layers are built on it | <ul style="list-style-type: none"> • Smooth surface finishing • Multi-material printing |
| Binder Jetting | Utilize a binder that was deposited using an inkjet-print head to join materials in a powder bed | <ul style="list-style-type: none"> • Parts can be made with a range of different colours |
| Material Extrusion | Continuous filament of a polymer is heated and extruded onto the platform or on top of previous layers | <ul style="list-style-type: none"> • Low cost • High speed |
| Vat Photo-polymerization | A pre-deposited photopolymer in a vat is selectively cured by light | <ul style="list-style-type: none"> • Fine resolution • High quality |
| Sheet Lamination | Layer-by-layer cutting and lamination of sheets or ribbons of metal | <ul style="list-style-type: none"> • Low cost • High speed |

2.2. Industrial Value

In the past 10 years, many companies have embraced AM technologies and are beginning to enjoy real business benefits from them. In a report by Statista, the global 3D printer market size reached US\$7.3 billion in 2017 and the aerospace and defence sectors account for 17.8% of the market distribution in 2016 [24]. The global AM market is expected to see double digit growth into 2022 with market analysis projecting a growth of up to 35% per annum [25]. Recent developments such as cheaper metal powder [26] and the influx of new vendors [27] have significantly reduced the cost of the printers and AM has worked its way into a number of markets. The growing consensus of adopting AM into a production floor is attributed to several advantages over traditional manufacturing, as shown in Table 2.

Table 2. Advantages of AM over traditional manufacturing adapted from [28]. Adapted from [28], with permission from Elsevier, 2020.

| Areas of Application | Advantages |
|--|---|
| Rapid Prototyping | <ul style="list-style-type: none"> • Reduce time to market by accelerating prototyping • Reduce the cost involved in product development • Making companies more efficient and competitive at innovation |
| Production of Spare Parts | <ul style="list-style-type: none"> • Reduce repair times • Reduce labour cost • Avoid costly warehousing |
| Small Volume Manufacturing | <ul style="list-style-type: none"> • Small batches can be produced cost-efficiently • Eliminate the investment in tooling |
| Customized Unique Items | <ul style="list-style-type: none"> • Eliminate mass customization at low cost • Quick production of exact and customized replacement parts on site • Eliminate penalty for redesign |
| Complex Work Pieces | <ul style="list-style-type: none"> • Produce complex work pieces at low cost |
| Machine Tool Manufacturing | <ul style="list-style-type: none"> • Reduce labour cost • Avoid costly warehousing • Enables mass customization at low cost |
| Rapid Manufacturing | <ul style="list-style-type: none"> • Directly manufacturing finished components • Relatively inexpensive production of small number of parts |
| Component Manufacturing | <ul style="list-style-type: none"> • Enable customization at low cost • Improve quality • Shorten supply chain • Reduce the cost involved in development • Help eliminate excess parts |
| On-site and On-demand Manufacturing of Replacement Parts | <ul style="list-style-type: none"> • Eliminate storage and transportation cost • Reduce downtime • Shorten supply chain • Allow product lifecycle leverage |
| Rapid Repair | <ul style="list-style-type: none"> • Reduction in repair time • Opportunity to modify repaired components to the latest design |

A wide variety of materials can be utilized, but metals are generally popular due to their extensive use in industrial and consumer appliances. Figure 2 illustrates the activity map of selected aerospace companies, with many players focusing their research and development work on AM technology. General Electric (GE) leads the industry in terms of the both the volume and machine capacity, and had printed more than 100,000 parts by 2020. Rolls Royce, MTU Aero Engines, Pratt and Whitney and GKN Aerospace have established their own competencies centre to upskill their AM capabilities [25]. GE Aviation has been particularly successful in implementing AM technology into its product. In 2015, GE announced that the next LEAP engine will have nearly 20 3D-printed fuel nozzles [29], simplifying parts by combining multiple components. Traditionally, the aerospace industry used advanced and costly materials like titanium and nickel alloys, which are difficult to manufacture and create a large amount of waste. For example, Wilson et al. [30] has shown that through the use of AM technology, his team was able to achieve a 45% carbon footprint improvement and a 36% savings in total energy over replacing it with an entirely new blade. In 2019, Rolls Royce produced its first AM low-pressure turbine for the Trent XWB-84 which is expected to result in a component weight reduction of up to 40% as well as generate significant cost savings for the company [31].

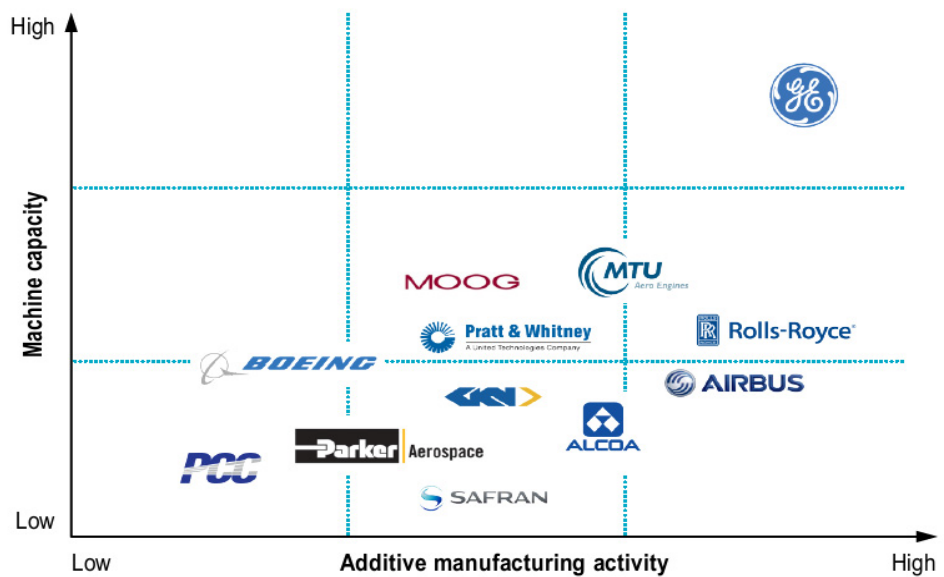


Figure 2. AM industry activity map of selected aerospace companies taken from [25], with permission from Roland Berger in 2020.

A separate report by Deloitte highlighted that AM technology has been shown to take the scrap rate to around 10–20% [32] while fabricating parts with intricate geometries such as internal cavities and lattice structures. Moreover, AM has the potential to lower overall cost as it is able to manufacture spare parts on demand, reducing maintenance time and the need for inventory management [33]. Boeing and Airbus typically source 4 million spare parts around the globe, and airlines usually maintain an inventory of spares to avoid their planes from becoming grounded. AM technology is an enabler for these companies to embark on a supply chain transformation, making on-demand manufacturing possible. Combined with the outbreak of COVID-19, companies are looking towards a “just in case” framework rather than “just in time” [34], specifically benefiting from the advanced production capability of AM processes.

2.3. Types of Metal AM Process

Out of the seven main AM processes, powder-bed fusion (PBF) and direct energy deposition (DED) are generally used to produce high-quality metal parts. Lewandowski et al. [15] categorized these two mainstream processes into respective energy sources for fusion and the companies that have a specialization in them, as shown in Figure 3.

The DED process has a high degree of control and freedom as it can simultaneously feed multiple types of powders through its nozzle, as shown in Figure 4a. By adjusting the feed rate, it is feasible to achieve desirable microstructural features and chemical composition which is favourable for building functionally graded materials [35] or structural metal components [21]. Apart from manufacturing near net shape components, DED is suitable for repairing high-value parts with little wastage [36–38]. This capability enables manufacturers to remanufacture turbine blades with cracks and voids which is economically viable and helps in design enhancements at the time of restoration [30]. Consequently, remanufacturing using accurate AM processes will enable industries to save energy and material, and contribute towards sustainable design and manufacturing. Despite its benefits, DED faces several challenges in terms of quality and efficiency. Resolutions are generally very low and parts have a rough surface finish that may need post-processing such as by machining to obtain tight tolerances [18].

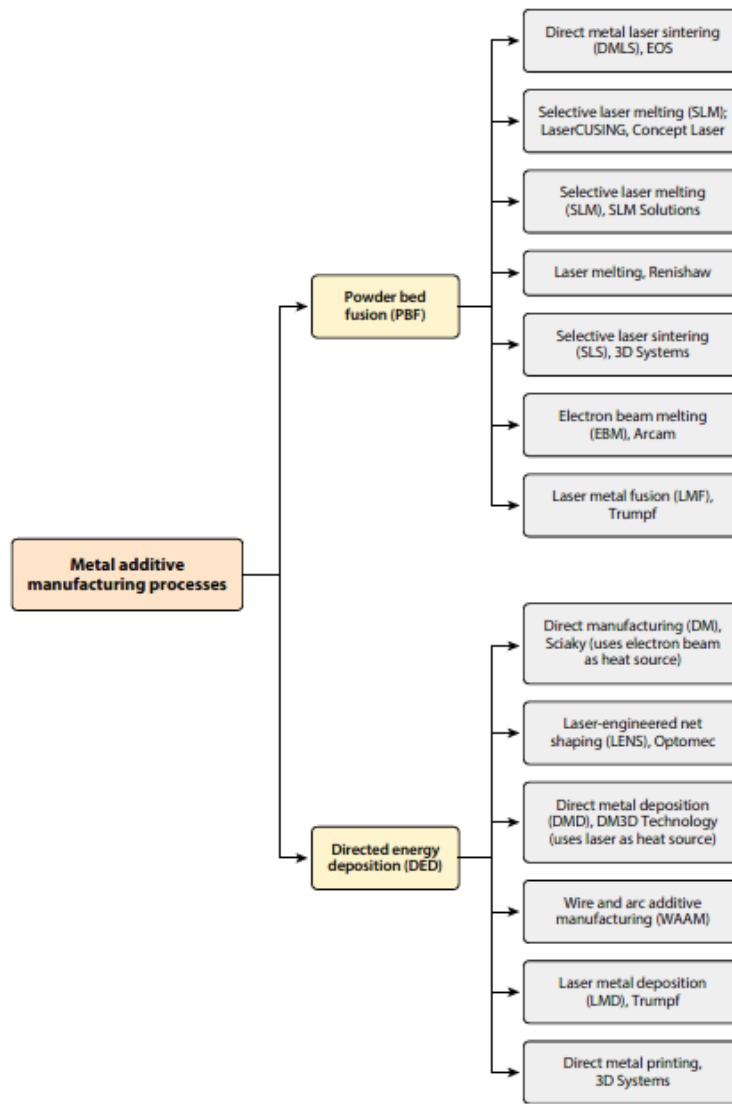


Figure 3. Various AM processes adapted from [15], with permission from Annual Reviews in 2020.

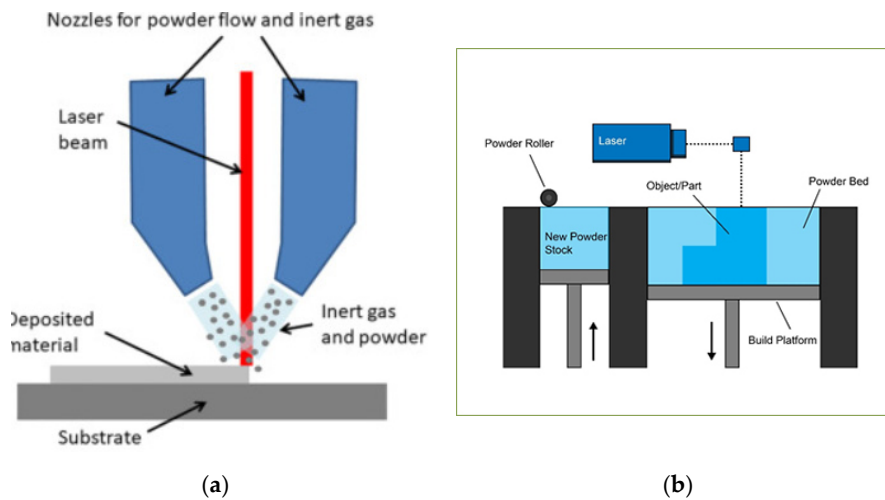


Figure 4. Schematic diagram of (a) direct energy deposition (DED), adapted from [39], with permission from Elsevier, 2020; and (b) powder-bed fusion (PBF), adapted from [40], with permission from Elsevier, 2020.

PBF has a unique position because of its potential to manufacture metal components in a range of alloys, at high resolution and accuracy, which has broadened the application to various industries. The process consists of depositing thin layers of fine powder on a platform which is then fused with a laser or electron beam, as shown in Figure 4b. Many metallic materials such as stainless and tool steels, aluminium alloys, titanium and its alloys, and nickel-based alloys can be manufactured by this process.

The main difference between DED and PBF is the way that that powder is fed. In PBF, metal powders are uniformly spread by a rake or roller, while in DED, powders are blown out from the nozzle. The high precision of PBF allows for the optimisation of component design and manufacturing cost. For example, GE aviation has been using metal PBF machines to manufacture its fuel nozzles and next-generation materials, including heat-resistant ceramic matrix composites (CMCs) and carbon-fibre blades. The fuel nozzles were five times more durable than the previous model and reduced the number of required parts from 25 to just five [29].

Another successful case study came from Arconic, which managed to install its 3D printed titanium brackets on the airframe of an Airbus A350 XWB commercial plane, which helps to lower the wastage of raw materials by 80% as compared to manufacturing conventionally [41]. Some of the common materials which have been processed by PBF by other authors are listed in Table 3.

Table 3. Common alloys processed by PBF.

| Alloy | Examples | Reference |
|----------------|---|--------------|
| Titanium | Ti-6Al-4V, Ti-6.5Al-1Mo-1V-2Zr, Ti-6.5Al-3.5Mo-1.5Zr-0.3Si, Ti-5Al-4Mo-2Zr-2Sn-4Cr, Ti-3Al-10V-2Fe | [42–54] |
| Intermetallics | NiTi | [55–58] |
| Steel | 316L, 17-4PH, AISI 420 | [59–64] |
| Nickel | IN718, IN625, C263, Hastelloy X, K418 | [5,65–100] |
| Aluminium | Al-Si10-Mg, Al-Si12-Mg, 6061 | [49,101,102] |

IN718 is the most commonly used nickel-based alloy in the aerospace industry due to its superior mechanical properties at elevated temperatures and it has been widely used in the turbine section of the aeroengine [103–105]. It has the ability to withstand loading at an operating temperature close to its melting point of 1336 °C [106]. It has a high phase stability of face-centred-cubic (FCC) nickel matrix and the capability to be strengthened by other alloys such as chromium and/or aluminium [107]. The microstructure of IN718 is referred to by γ (gamma), a continuous matrix phase where cobalt and chromium prefers to reside; γ' (gamma prime), an intermetallic phase based on $\text{Ni}_3(\text{Al,Ti})$ with a L_{12} crystal structure; γ'' (gamma double prime), a metastable phase that is the primary strengthening precipitate with a body-centred tetragonal (BCT) ordered compound with a $D0_{22}$ crystal structure; δ (delta), an equilibrium phase with an orthorhombic $D0_a$ structure; Laves phase with an embrittling TCP phase; carbides and borides that prefer to reside on the grain boundaries [20,108,109]. However, the usage of PBF IN718 in the aeroengine has been an obstacle owing to the presence of undesirable phases [110] and its unconventional microstructure [80,110,111]. Efforts have been made to limit these defects through the use of heat treatment [5,110] and hot isostatic pressing (HIP-ing) [74], but the results have been mixed and no significant improvements have been made on PBF IN718. Special attention is paid to the microstructure effect of AM IN718 on its material performance.

3. Microstructure of AM IN718

3.1. Grain Structure

In this review, grain structure constitutes both grain size and grain texture of the material. Unlike its wrought counterpart, AM IN718 display a mixture of columnar and equiaxed grains when no additional treatment is applied. This is due to its uneven cooling rate as the material is being built up layer by layer. Factors such as heat flux and thermal gradients greatly affect the growth of the grains, which are not discussed in this paper. Interested readers could look at the references given

here [93,112–114]. Ahmad et al. [110] showed that AM IN718 has columnar grain growing parallel to the building direction. A magnified image of the microstructure of AM IN718 without any additional treatment using a scanning electron microscope (SEM) is shown in Figure 5.

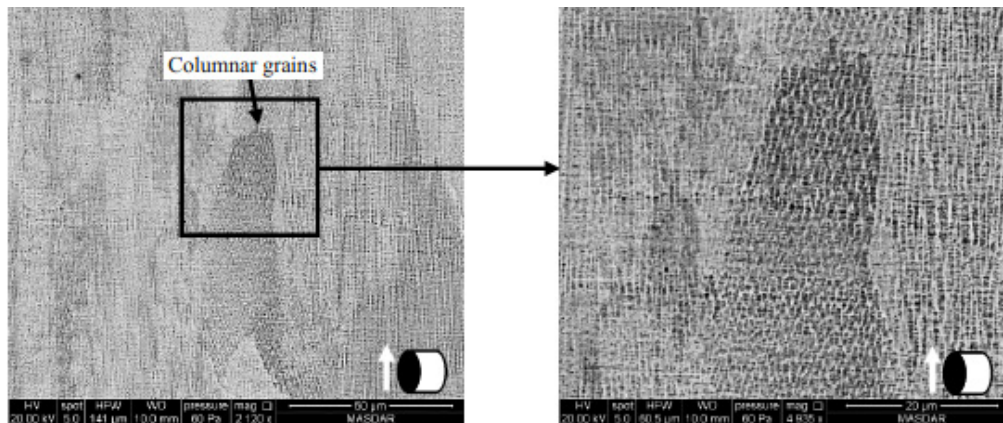


Figure 5. Scanning electron microscope (SEM) image showing the columnar grains of AM IN718, taken from [110]

Gribbin et al. [115] took one step further and utilized electron backscatter diffraction (EBSD) to investigate the crystallographic structure of the material. As-built AM IN718 exhibits elongated grain structure with a moderate $\langle 100 \rangle$ fibre texture formed along the build direction, as shown in Figure 6. Fatigue strength of the wrought alloy outperforms the AM alloy at room temperature, suggesting the grain texture is likely the main competing microstructural feature affecting the fatigue performances at room temperature. The microstructural study findings were comparable to other studies as well [70,80,86,116], although fatigue life is known generally to be dominated by surface characteristic such as surface roughness [50,117–119] and porosity [79,120], and thus the conclusion made by Gribbin et al. might be incomplete and further investigation has to be undertaken. The fatigue response of the as-built AM material had a similar response to the wrought material at elevated temperature of 500 °C. Both materials had a fatigue limit of approximately 600 MPa [115] despite AM IN718's inherent weakness of high content of δ precipitates, which is known to deteriorate the fatigue behaviour at high temperature. This suggests that the difference in microstructural features is not pronounced in high-temperature environments as compared to the room temperature condition.

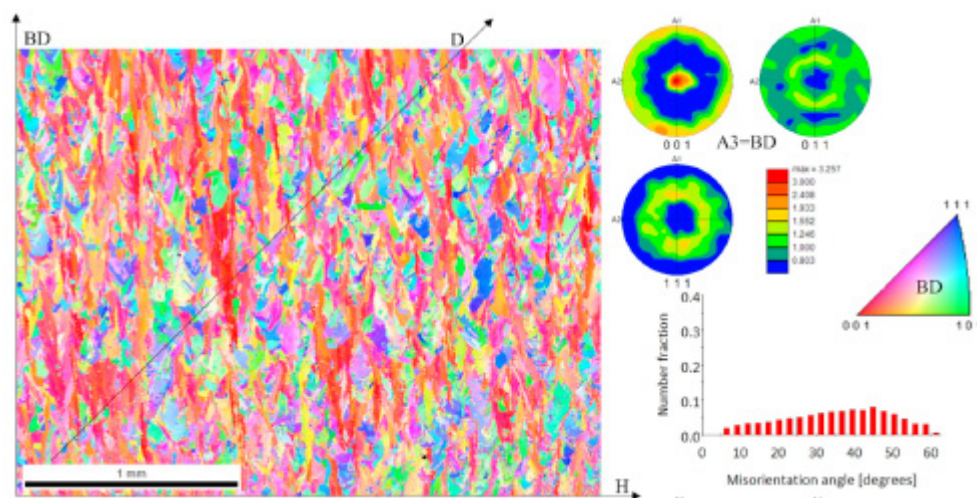


Figure 6. Electron backscatter diffraction (EBSD) map and the pole figures showing the crystallographic texture of as-built AM IN718. Adapted from [115], with permission from Elsevier, 2020.

Another interesting finding on wrought IN718 in elevated temperature has [121] shown that the coarse-grain alloy has a fatigue strength significantly lower than fine-grain alloy when it is beyond 10^5 cycles. It is likely that in order to maximize AM IN718 capability in high-temperature applications, controlling the grain size of the alloy will be vital, and any grain size refinement technique for AM metal alloys will be welcome.

3.2. Effects of δ Phases

IN718 is a precipitation-strengthened nickel-based superalloy with γ'' as the main phase contributing to its excellent high temperature strength [122]. However, the metastable γ'' phase easily transforms to a stable δ phase under certain thermal conditions, decreasing the volume fraction of γ'' , which indirectly affects the mechanical properties of the alloy [123]. It is generally undesirable as it is known to decrease the fracture toughness and ductility of the material [124,125]. δ precipitates usually formed during the heat treatment process or during service and mainly reside at the grain boundaries [126]. However, there are cases where δ precipitates have been shown to display beneficial effects such as grain stabilization [127] and increasing stress rupture resistance [128]. An et al. [129] investigated the role of the δ phase for fatigue crack propagation behaviour in wrought IN718 and showed that the growth rate increases with increasing δ phase volume fractions. There were both long needle-like and granular shaped δ precipitates present in the alloy which have very different effects on the fatigue crack growth. When γ'' transforms into long needle-like δ precipitates, a precipitates free zone formed around the δ phase, inhibiting micro cracks that are detrimental to the fatigue performance of the alloy. The granular-shaped δ precipitates, with low length-diameter ratio, act as a pin between the grain boundaries, increasing the strength of the alloy.

AM IN718 usually has a slight variation on the volume fraction of its respective phases. In Gribbin's study, the δ phase content in wrought IN718 was $1.6\% \pm 0.5\%$ while in the as-built AM IN718 it was $3.8\% \pm 0.4\%$ [115], which is rather unusual for the IN718 alloy. The increase of the δ phase content could be due to the heat treatment used to solution treat the alloy, leaving the precipitates undissolved. Yang et al. [130] compared the microstructure and mechanical performances of PBF-fabricated IN 718 alloy in various heat treatment conditions. The results show that the morphology and distributions of the δ phase are key factors determining their high temperature performance. Too much δ phase along the grain boundaries could cause dislocation to pile up [86], causing local stress concentrations and premature failure. The lack of the δ phase will reduce the strength of the alloy at elevated temperature as it will have limited influence of the pinning effect on grain boundaries.

The formation of intragranular δ precipitates was also observed in AM IN718, which is a common observation for IN718 alloy when the parameters of the heat treatment are not optimized [123]. The presence of a high concentrations of niobium in the feedstock [115], combined with the inconsistent heat flux caused by heating and melting of the powder, is the reason why intragranular δ precipitates are formed. Maximizing the volume fraction of intergranular δ precipitates gives the alloy better ductility while a high amount of intragranular δ precipitates hardens the material [123]. The ratio between intragranular and intergranular precipitates could be a critical parameter in optimizing the mechanical properties at elevated temperature of AM IN718 based on past studies.

3.3. Effects of Laves Phases

Niobium is one of the elements present in IN718 and it is highly prone to segregation and tends to form some undesirable phases such as the δ and the Laves phases, which is known for degrading tensile ductility, fatigue and creep rupture properties [131–133]. A high concentration of niobium has been reported by other researchers which catalyse the formation of the Laves phase, depleting the strengthening γ'' phase. The Laves phase provides crack initiation and propagation sites during the melting of the metal powder [132] and is a general observation when IN718 alloy undergoes a process in a high-temperature environment [134] such as heat treatment [5,135,136] or during the powder deposition of the AM process [73,116,137].

The presence of the Laves phase generally deteriorates the ductility, ultimate tensile strength [138] and fatigue life of IN718 alloy [139]. Sui et al. [78] reported that AM IN718 alloy outperforms its wrought counterpart at low stress amplitude due to the role that the Laves phase played during the crack propagation stage. At high stress amplitude, almost all the Laves phase splintered into small fragments that caused microscopic holes or cracks to form. The S-N diagram developed by Sui et al. is shown in Figure 7. The existence of a micron-scaled Laves phase led to local stress concentrations more easily than the wrought alloy, causing it to break up at high stress amplitude. A schematic diagram on the fragmentation of the Laves phase is shown in Figure 8.

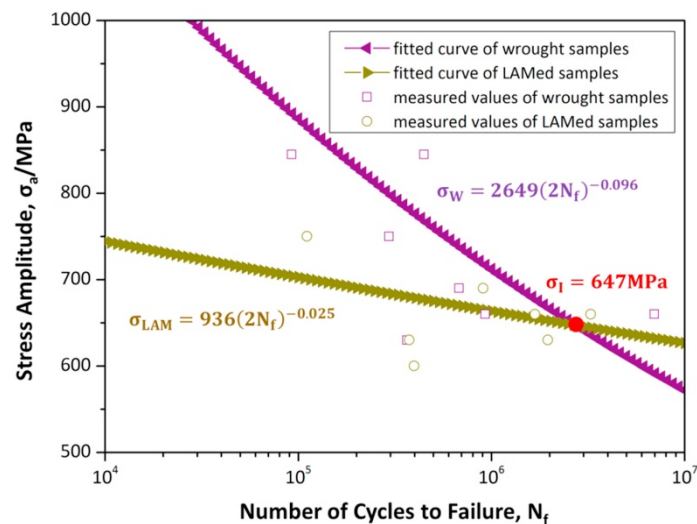


Figure 7. High cycle properties of wrought (in purple) and AM (in green) IN718 alloy. Adapted from [78], with permission from Elsevier, 2020.

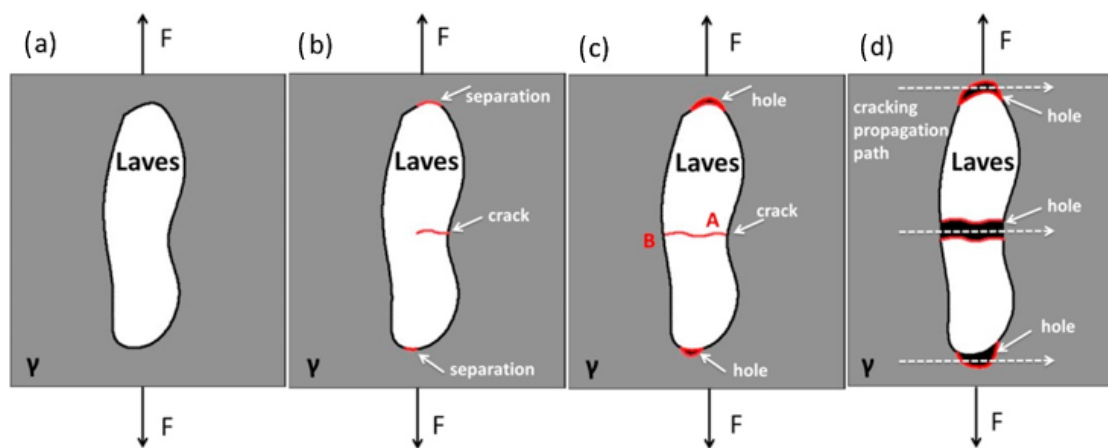


Figure 8. Schematic diagram of (a) Laves phase present in the matrix, (b) crack initiated in the Laves when a tensile force is applied, (c) crack propagates through the Laves, (d) breaking up of Laves phase at high amplitude. Adapted from [78], with permission from Elsevier, 2020.

To the best of the authors' knowledge, there have been no studies on the effect of the Laves phase on the properties affecting the fatigue life of AM IN718 at high temperature. It is generally regarded as a "parasitic" phase that consumes the available niobium content. Studies have shown that either increasing the homogenization temperature or time [122,140] could lower the volume fraction of the Laves phase. Laves and carbide are generally dissolved resulting in the release of a considerable amount of niobium back to the Y' matrix [136]. With that in mind, it is advisable to formulate new heat treatment standards cater for AM IN718 alloy that is entirely different from the Aerospace Material Specifications (AMS) standards that industry currently uses.

4. Mechanical Properties of Powder-Bed Fusion (PBF) IN718 Alloy

Table 4 presents previous work on the mechanical testing of PBF IN718 alloy. Most of the test data are rather similar with slight differences due to either the geometry of the test piece or the direction of the test piece when it is being tested. Generally, a post-processing step such as heat treatment or HIP-ing gives a better tensile strength but with a slight dip in ductility. There were some instances where the tensile properties were superior to the wrought ones, giving the manufacturer extra confidence in employing AM IN718 on its production line. Researchers such as Strößner et al. [111] and Gallmeyer et al. [141] have attempted to optimize the heat treatment process by increasing its homogenization or ageing temperature and thereby controlling the growth of the γ'' phase, and minimizing the impact of either the δ or Laves phases, resulting in an increase in the strength and hardness of the material.

Table 4. Summary of mechanical properties of PBF IN718 alloy.

| Condition | UTS/MPa | YS/MPa | El/% | Stress Ratio | Loading Frequency/Hz | Cycles to Failure | Reference |
|------------------------|--|---------------|--------------|--------------|----------------------|----------------------------------|---------------------|
| As-built | 1110 ± 11 | 711 ± 14 | 24.5 ± 1.1 | - | - | - | [84] |
| | 1167 ± 10 | 858 ± 12 | 21.5 ± 1.3 | - | - | - | [84] |
| | 845 | 580 | 21.5 ± 1.3 | - | - | - | [84] |
| | 1010 ± 10 | 737 ± 4 | 20 | - | - | - | [84] |
| | 997.8 | 800 | 20.6 ± 2.1 | - | - | - | [84] |
| | 1335 | 760 | 21.3 | - | - | - | [141] |
| | 1142.5 ± 5.5 | 898 ± 9 | 22.55 ± 3.35 | - | - | - | [73] |
| | 1451 | 1174 | 13.5 | - | - | - | [69] |
| | 1370 ± 25 | - | 22.2 ± 2 | - | - | - | [77] |
| | 1221 | 1007 | 16.0 | - | - | - | [82] |
| As-built, heat treated | - | - | - | 0 | 20 | 2 × 10 ⁶ (run out) | [144] |
| | 1085 ± 11 | 816 ± 24 | 19.1 ± 0.7 | - | - | - | [111] |
| | 1010 ± 10 | 737 ± 4 | 20.6 ± 2.1 | - | - | - | [111] |
| | 1417 ± 4 | 1222 ± 26 | 15.9 ± 1.0 | - | - | - | [111] |
| | 1387 ± 12 | 1186 ± 23 | 17.4 ± 0.4 | - | - | - | [111] |
| | 1325 | 620 | 28.6 | - | - | - | SA980 [141] |
| | 1530 | 1135 | 10.6 | - | - | - | SHT-1 [141] |
| | 1560 | 1240 | 11.6 | - | - | - | SHT-2 [141] |
| | 1500 | 1120 | 14.5 | - | - | - | DA620 [141] |
| | 1580 | 1300 | 9.6 | - | - | - | DA720 [141] |
| | 1640 | 1245 | 16.6 | - | - | - | SA1020 + A720 [141] |
| | 1319 ± 39 | 1131.5 ± 29.5 | 16 ± 6 | - | - | - | [73] |
| | As-built, hot isostatic pressing (HIP), heat treated | 1200 | 890 | 28 | - | - | - |
| 1384 ± 8 | | 1123 ± 13 | 21.5 ± 3.5 | - | - | - | [145] |
| Wrought | 1241 | 1034 | 10 | - | - | - | AMS 5662 [146] |
| | 1610 | 1160 | 13.5 | - | - | - | [141] |
| As-cast | 802 | 758 | 5 | - | - | - | AMS 5383 [146] |

Data about the fatigue strength of PBF IN718 alloy was limited as it usually costs a significant amount of resources to develop. Fatigue tests are typically conducted on servo hydraulic test machines which are capable of applying large amplitude cycles over a long period of time [142]. They are heavily used in high-value industries such as the aerospace and biomedical sectors where safety standards are much more stringent than in other sectors. For AM IN718 alloy to be used in a safety-critical application, it is vital to understand the process-structure-property relationship, and the availability of fatigue data gives extra confidence for manufacturers to utilize this technology. At the same time, several problems such as weak grain texture and detrimental residual stress [43,115,143] have to be dealt with in order to widen the adoption of AM IN718 alloy. This drives a need to introduce novel post-processing methods to improve the quality of AM products, which will be discussed in the next section.

5. Suitability of Surface Enhancement Process

Erfan et al. [147] utilize a common approach in cost, risk analysis and management to review the known surface treatment process in order to evaluate the commercial value that these processes bring

to the AM production line. Ranking is undertaken according to the time and money needed to utilize the treatment, as seen in Figure 9b. Examples of material removal mechanical processes are traditional machining and polishing techniques. They were ranked first, due to the wealth of research findings to make the process more effective and the relatively low cost to employ in AM products. Next in line are processes such as chemical etching [148] and electrochemical polishing (ECP) [149] techniques that are used for parts with intricate geometries such as lattice and cellular structure which are hard to reach. In addition, these chemical techniques have been able to decrease surface roughness with an average and max height improvement of 73% and 65% respectively for ECP [149].

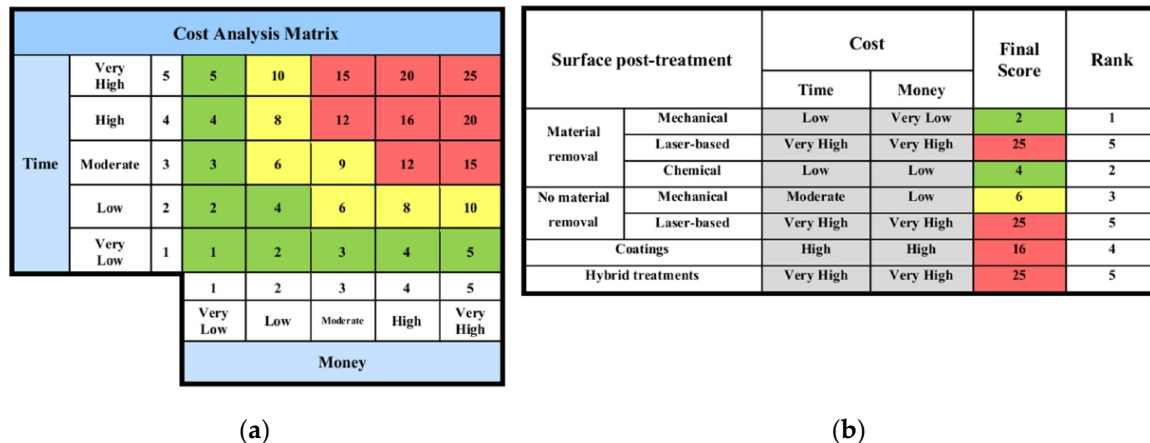


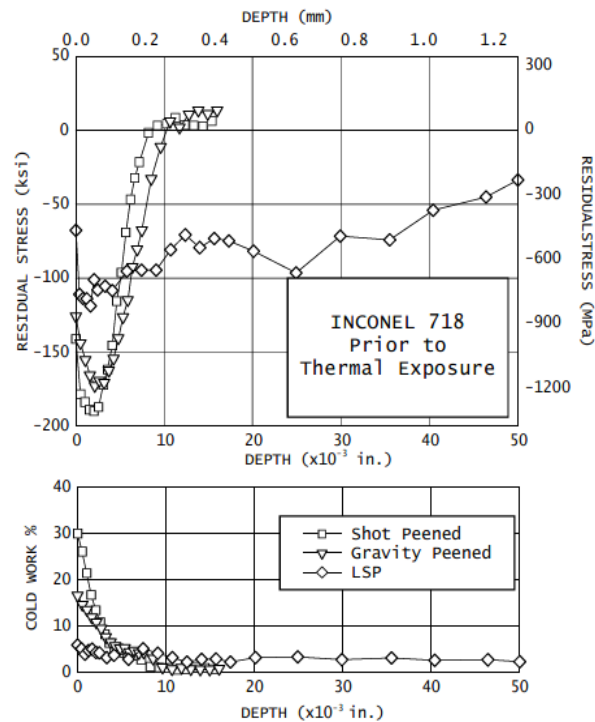
Figure 9. Taken from [147], with permission from Elsevier, 2020. (a) cost analysis matrix (b) scores and rank of various surface treatment process in terms of cost analysis.

On the other hand, surface treatments such as shot-peening [150], deep-rolling [151] and laser shock peening (LSP) [152] are categorized under no material removal mechanical treatments and are commonly used to increase the usability of AM materials. For high-temperature applications, LSP has additional advantages over other surface treatments due to its ability to impart deep compressive residual stresses [153], lower cold work on the surface [154] and the ability for grain refinements [155,156]. Inherently, the LSP process introduces high strain rates up to 10^6 s^{-1} which generate beneficial dislocations near the surface layer [157–159].

Table 5 compares the effects of shot peening and LSP on strain rate, cold work, depth of influence and the typical roughness of various metal alloys. Generally, LSP brings about a significant lower cold work as compared to shot peening. A lower amount of cold work was observed in Ti-6Al-4V [160] and IN718 coupons where the cold work was between 1–6% [154]. The amount of cold work that is being induced by LSP boils down to the material's deformation capability. Although it is beyond the scope of this work to discuss shot peening, it is useful to bring it up as a comparison to LSP as it is a widely adapted technique in the industry. Shot peening involves multiple steel or ceramic shots projected at a high velocity through a nozzle, striking the surface with force sufficient to create plastic deformation. Due to the continuous shots, most of the energy is expended in inducing plastic deformation, resulting in a highly cold-worked surface layer [160]. On the other hand, LSP produces remarkably low cold work on the surface at room temperature [161], as shown in Figure 10. The cold work produced by shot peening comes close to 0% after a depth of 10×10^{-3} inch, dropping from the initial 30%. This begs the question of why LSP is able to drive similar or higher compressive residual stresses and yet produce a lower amount of cold work on the surface.

Table 5. Comparison of shot peening and laser shock peening (LSP).

| | Strain Rate (s ⁻¹) | Cold Work (%) | Depth (mm) | Typical Roughness Ra (μm) |
|-----------------------|-----------------------------------|---------------|------------|------------------------------|
| Shot peen (X20 Steel) | 10 ³ –10 ⁴ | 15–50 | 0.2 | 4.52 |
| LSP (X20 Steel) | 10 ⁶ –10 ⁷ | 5–7 | 1.2 | 0.98 |
| Shot peen (Ti-6Al-4V) | - | 75 | Surface | - |
| LSP (Ti-6Al-4V) | - | 1–2 | Surface | - |
| Shot peen (IN718) | - | 30 | Surface | - |
| LSP (IN718) | - | 3–6 | Surface | - |

**Figure 10.** Taken from [160], Residual stress distribution and cold work developed by in IN718 coupons using various surface enhancement process.

A high degree of cold work has been found to relax rapidly at high temperature [160–162] which is detrimental for high temperature application in the nuclear and aerospace industries. LSP might be in a more advantageous position than shot peening if it is able to withstand thermal stress relaxation in these industries. More investigation has to be done to find out the process-structure-property-performance relationship, utilizing advanced material characterization methods such as EBSD or transmission electron microscopy (TEM).

There are interesting initiatives where LSP is being used as a post-processing step for AM metal components such as aluminium [163], stainless steel [164] and titanium alloy [152]. Kalentics et al. [164,165] have proposed using LSP to tailor the residual stresses of stainless steel samples by moving the baseplate back and forth from a printing machine to an LSP station. He has dubbed it as 3D LSP, an ex-situ LSP and AM process which has been shown to increase both the magnitude and depth of compressive residual stress. The depth of compressive residual stress could reach up to 1 mm for an AM 316L stainless steel component subjected to the 3D LSP principle, as shown in Figure 11. This research is a promising start to combine LSP techniques into AM material, making it more useable for aerospace applications.

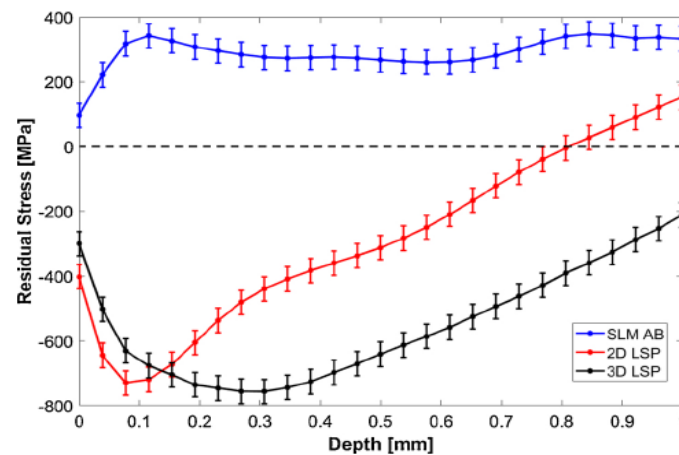


Figure 11. Taken from [164], with permission from Elsevier, 2020. Residual stress curve measured for 316L Stainless Steel for as-built (AB), LSP after AM (2D LSP) and ex-situ LSP on AM (3D LSP). Adapted from [164], with permission from Elsevier, 2020

6. Conclusions

The current priority of aeroengine manufacturers is to investigate the applicability of AM components in their manufacturing process as it offers significant processing flexibility and potential cost reduction. IN718 is one of those metal alloys that is suitable for the AM process route as it allows manufacturers to process it in an easy and straightforward way that ensures that the material properties are still well preserved. With layer-wise building of components, the process produces up to about 5% waste, reducing the raw material wastage significantly as compared to manufacturing it conventionally for aeroengine components.

Inherently, as-built AM products give a mixture of columnar and equiaxed grains which directly impacts the mechanical properties of the material at room temperature. At high temperature usage, its effect is not as prominent, and grain size will be the crucial factor in determining its fatigue life. Further research should be performed to identify the effects of the various phases present in the alloy that affect the usability of the material. It should be possible to control the growth of γ'' , δ and Laves to maximize the properties of AM IN718 alloy as suited for its intended application.

Numerous heat-treatment procedures have been attempted by the scientific community to match its tensile strength with the wrought alloy. Higher homogenization temperature and longer ageing time is usually employed to reduce the presence of harmful phases such as the δ and Laves phases. Such knowledge is important for developing beneficial microstructures and material properties for the intended application.

Analysis obtained from the literature suggest that the mechanical properties of PBF IN718 alloy were very similar to its wrought counterpart. However, there were insufficient experimental data to showcase the fatigue lifespan of AM IN718 alloy due to the complexity and high cost of the experiments.

Surface enhancement techniques were explored in this study as this could assist AM IN718 alloy to perform better in high-temperature applications. LSP has the potential to be a suitable technique as it can induce a lower amount of cold work which is beneficial in a high-temperature environment.

Author Contributions: Conceptualisation, literature review and writing of the manuscript were done by C.K.Y. Supervision and review of the manuscript performed by G.J.G., G.W. and C.C.W. All authors have read and agreed to the published version of the manuscript.

Funding: This research was funded by Agency for Science, Technology and Research (A*STAR) Singapore and Warwick Manufacturing Group (WMG), University of Warwick.

Acknowledgments: This research is part of the EngD project that is sponsored by A*STAR and the authors are thankful for the funding.

Conflicts of Interest: The authors declare no conflict of interest.

References

1. Systems, D. Our Story. Available online: <https://uk.3dsystems.com/our-story> (accessed on 10 January 2020).
2. ISO. *F42 Committee Terminology for Additive Manufacturing—General Principles—Terminology*; International Organization for Standardization: London, UK, 2017.
3. Wen, Y.; Xun, S.; Haoye, M.; Baichuan, S.; Peng, J.; Xuejian, L.; Kaihong, Z.; Xuan, Y.; Jiang, P.; Lu, S. 3D printed porous ceramic scaffolds for bone tissue engineering: A review. *Biomater. Sci.* **2017**, *5*, 1690–1698. [[CrossRef](#)] [[PubMed](#)]
4. Maconachie, T.; Leary, M.; Lozanovski, B.; Zhang, X.; Qian, M.; Faruque, O.; Brandt, M. SLM lattice structures: Properties, performance, applications and challenges. *Mater. Des.* **2019**, *183*, 108137. [[CrossRef](#)]
5. Zhang, D.; Niu, W.; Cao, X.; Liu, Z. Effect of standard heat treatment on the microstructure and mechanical properties of selective laser melting manufactured Inconel 718 superalloy. *Mater. Sci. Eng. A* **2015**, *644*, 32–40. [[CrossRef](#)]
6. Hackel, L.; Fuhr, J.; Sharma, M.; Rankin, J.; Sherman, V.; Davami, K. Test Results for Wrought and AM In718 Treated by Shot Peening and Laser Peening Plus Thermal Microstructure Engineering. *Procedia Struct. Integr.* **2019**, *19*, 452–462. [[CrossRef](#)]
7. Salvati, E.; Lunt, A.J.; Heason, C.P.; Baxter, G.J.; Korsunsky, A.M. An analysis of fatigue failure mechanisms in an additively manufactured and shot peened IN 718 nickel superalloy. *Mater. Des.* **2020**, *191*, 108–605. [[CrossRef](#)]
8. Xu, X.; Ganguly, S.; Ding, J.; Seow, C.E.; Williams, S. Enhancing mechanical properties of wire + arc additively manufactured INCONEL 718 superalloy through in-process thermomechanical processing. *Mater. Des.* **2018**, *160*, 1042–1051. [[CrossRef](#)]
9. Kumar, N.N.; Yadav, A.C.; Raja, K.; Prabhakaran, S.; Naiju, C.D.; Kalainathan, S. Study on Effect of Laser Peening on Inconel 718 Produced by DMLS Technique. In Proceedings of the International Conference on Advances in Design, Materials, Manufacturing and Surface Engineering for Mobility, Chennai, India, 11 October 2019.
10. Jinoop, A.N.; Subbu, S.K.; Paul, C.P.; Palani, I.A. Post-processing of Laser Additive Manufactured Inconel 718 Using Laser Shock Peening. *Int. J. Precis. Eng. Manuf.* **2019**, *20*, 1621–1628. [[CrossRef](#)]
11. Kattoura, M.; Telang, A.; Mannava, S.R.; Qian, D.; Kattoura, M. Effect of Ultrasonic Nanocrystal Surface Modification on residual stress, microstructure and fatigue behavior of ATI 718Plus alloy. *Mater. Sci. Eng. A* **2018**, *711*, 364–377. [[CrossRef](#)]
12. Yan, W.; Lin, S.; Kafka, O.L.; Yu, C.; Liu, Z.; Lian, Y.; Wolff, S.; Cao, J.; Wagner, G.J.; Liu, W.K. Modeling process-structure-property relationships for additive manufacturing. *Front. Mech. Eng.* **2018**, *13*, 482–492. [[CrossRef](#)]
13. Yan, F.; Xiong, W.; Faierson, E.J. Grain Structure Control of Additively Manufactured Metallic Materials. *Materials* **2017**, *10*, 1260. [[CrossRef](#)]
14. Ngo, T.D.; Kashani, A.; Imbalzano, G.; Nguyen, K.T.; Hui, D. Additive manufacturing (3D printing): A review of materials, methods, applications and challenges. *Compos. Part B Eng.* **2018**, *143*, 172–196. [[CrossRef](#)]
15. Lewandowski, J.J.; Seifi, M. Metal Additive Manufacturing: A Review of Mechanical Properties. *Annu. Rev. Mater. Res.* **2016**, *46*, 151–186. [[CrossRef](#)]
16. Zhang, Y.; Wu, L.; Guo, X.; Kane, S.; Deng, Y.; Jung, Y.-G.; Lee, J.-H.; Zhang, J. Additive Manufacturing of Metallic Materials: A Review. *J. Mater. Eng. Perform.* **2018**, *27*, 1–13. [[CrossRef](#)]
17. Wong, K.-F.V.; Hernandez, A. A Review of Additive Manufacturing. *ISRN Mech. Eng.* **2012**, *2012*, 1–10. [[CrossRef](#)]
18. Saboori, A.; Gallo, D.; Biamino, S.; Fino, P.; Lombardi, M. An Overview of Additive Manufacturing of Titanium Components by Directed Energy Deposition: Microstructure and Mechanical Properties. *Appl. Sci.* **2017**, *7*, 883. [[CrossRef](#)]
19. Frazier, W.E. Metal Additive Manufacturing: A Review. *J. Mater. Eng. Perform.* **2014**, *23*, 1917–1928. [[CrossRef](#)]
20. Gibson, I.; Rosen, D.; Stucker, B. *Additive Manufacturing Technologies*; Springer International Publishing: New York, NY, USA, 2010.
21. Graf, B.; Gumenyuk, A.; Rethmeier, M. Laser Metal Deposition as Repair Technology for Stainless Steel and Titanium Alloys. *Phys. Procedia* **2012**, *39*, 376–381. [[CrossRef](#)]

22. University, L. Material Jetting. About Additive Manufacturing. Available online: <https://www.lboro.ac.uk/research/amrg/about/the7categoriesofadditivemanufacturing/materialjetting/> (accessed on 10 January 2020).
23. University, L. Binder Jetting. About Additive Manufacturing. Available online: <https://www.lboro.ac.uk/research/amrg/about/the7categoriesofadditivemanufacturing/binderjetting/> (accessed on 10 January 2020).
24. Statista. *3D Printing Market Distribution Worldwide in 2016, by Use Case*; Statista: Hamburg, Germany, 2016.
25. Berger, R. *Additive Manufacturing in Aerospace and Defense*; Ronald Berger Strategy Consultants: Munich, Germany, 2017.
26. Medina, F. Reducing Metal Alloy Powder Costs for Use in Powder Bed Fusion Additive Manufacturing: Improving the Economics for Production, in Materials Science and Engineering. Ph.D. Thesis, University of Texas, El Paso, TX, USA, January 2013.
27. The Additive Manufacturing Industry Landscape 2020: 240 Companies Driving Digital Manufacturing. 2020. Available online: <https://amfg.ai/2020/05/26/the-additive-manufacturing-industry-landscape-2020-231-companies-driving-digital-manufacturing/> (accessed on 10 January 2020).
28. Attaran, M. The rise of 3-D printing: The advantages of additive manufacturing over traditional manufacturing. *Bus. Horizons* **2017**, *60*, 677–688. [CrossRef]
29. Kellner, T. Fit to Print: New Plant Will Assemble World's First Passenger Jet Engine With 3D Printed Fuel Nozzles, Next-Gen Materials. 2014. Available online: <https://www.ge.com/reports/post/80701924024/fit-to-print/> (accessed on 10 January 2020).
30. Wilson, J.M.; Piya, C.; Shin, Y.C.; Zhao, F.; Ramani, K. Remanufacturing of turbine blades by laser direct deposition with its energy and environmental impact analysis. *J. Clean. Prod.* **2014**, *80*, 170–178. [CrossRef]
31. Rolls Royce. *2019 Annual Report*; Rolls Royce plc: London, UK, 2020.
32. Cotteleer, M.; Holdowsky, J.; Mahto, M.; Coykendall, J. 3D opportunity for aerospace and defense: Additive manufacturing takes flight. Available online: <https://www2.deloitte.com/insights/us/en/focus/3d-opportunity/additive-manufacturing-3d-opportunity-in-aerospace.html> (accessed on 10 January 2020).
33. Khajavi, S.H.; Partanen, J.; Holmström, J. Additive manufacturing in the spare parts supply chain. *Comput. Ind.* **2014**, *65*, 50–63. [CrossRef]
34. Board, E. *Companies Should Shift From 'Just in Time' To 'Just in Case'*; Financial Times: London, UK, 2020.
35. Wilson, J.M.; Shin, Y.C. Microstructure and wear properties of laser-deposited functionally graded Inconel 690 reinforced with TiC. *Surf. Coatings Technol.* **2012**, *207*, 517–522. [CrossRef]
36. Zhong, C.; Kittel, J.; Gasser, A.; Schleifenbaum, J.H. Study of nickel-based super-alloys Inconel 718 and Inconel 625 in high-deposition-rate laser metal deposition. *Opt. Laser Technol.* **2019**, *109*, 352–360. [CrossRef]
37. Sun, G.; Shen, X.; Wang, Z.; Zhan, M.; Yao, S.; Zhou, R.; Ni, Z. Laser metal deposition as repair technology for 316L stainless steel: Influence of feeding powder compositions on microstructure and mechanical properties. *Opt. Laser Technol.* **2019**, *109*, 71–83. [CrossRef]
38. Kumar, L.J.; Nair, C.K. Laser metal deposition repair applications for Inconel 718 alloy. *Mater. Today Proc.* **2017**, *4*, 11068–11077. [CrossRef]
39. Sing, S.L.; Tey, C.F.; Tan, J.H.K.; Huang, S.; Yeong, W.Y. 2–3D printing of metals in rapid prototyping of biomaterials: Techniques in additive manufacturing. In *Rapid Prototyping of Biomaterials*, 2nd ed.; Narayan, R., Ed.; Woodhead Publishing, 2020; pp. 17–40. Available online: <https://www.sciencedirect.com/book/9780081026632/rapid-prototyping-of-biomaterials#book-info> (accessed on 10 January 2020).
40. Dev Singh, D.; Mahender, T.; Reddy, A.R. Powder bed fusion process: A brief review. *Mater. Today Proc.* **2020**. [CrossRef]
41. Molitch-Hou, M. Arconic Talks Installing 3D-Printed Bracket on Series Production Commercial Airbus Airframe. Available online: <https://www.engineering.com/3DPrinting/3DPrintingArticles/ArticleID/15709/Arconic-Talks-Installing-3D-Printed-Bracket-on-Series-Production-Commercial-Airbus-Airframe.aspx> (accessed on 10 January 2020).
42. Zhu, Y.-Y.; Tang, H.-B.; Li, Z.; Xu, C.; He, B. Solidification behavior and grain morphology of laser additive manufacturing titanium alloys. *J. Alloy. Compd.* **2019**, *777*, 712–716. [CrossRef]
43. Benedetti, M.; Fontanari, V.; Bandini, M.; Zanini, F.; Carmignato, S. Low- and high-cycle fatigue resistance of Ti-6Al-4V ELI additively manufactured via selective laser melting: Mean stress and defect sensitivity. *Int. J. Fatigue* **2018**, *107*, 96–109. [CrossRef]

44. Chern, A.H.; Nandwana, P.; Yuan, T.; Kirka, M.M.; Dehoff, R.R.; Liaw, P.K.; Duty, C.E. A review on the fatigue behavior of Ti-6Al-4V fabricated by electron beam melting additive manufacturing. *Int. J. Fatigue* **2019**, *119*, 173–184. [[CrossRef](#)]
45. Fatemi, A.; Molaei, R.; Sharifimehr, S.; Phan, N.; Shamsaei, N. Multiaxial fatigue behavior of wrought and additive manufactured Ti-6Al-4V including surface finish effect. *Int. J. Fatigue* **2017**, *100*, 347–366. [[CrossRef](#)]
46. Fatemi, A.; Molaei, R.; Sharifimehr, S.; Shamsaei, N.; Phan, N. Torsional fatigue behavior of wrought and additive manufactured Ti-6Al-4V by powder bed fusion including surface finish effect. *Int. J. Fatigue* **2017**, *99*, 187–201. [[CrossRef](#)]
47. Günther, J.; Krewerth, D.; Lippmann, T.; Leuders, S.; Tröster, T.; Weidner, A.; Biermann, H.; Niendorf, T. Fatigue life of additively manufactured Ti-6Al-4V in the very high cycle fatigue regime. *Int. J. Fatigue* **2017**, *94*, 236–245. [[CrossRef](#)]
48. Levy, D.; Shirizly, A.; Rittel, D. Static and dynamic comprehensive response of additively manufactured discrete patterns of Ti6Al4V. *Int. J. Impact Eng.* **2018**, *122*, 182–196. [[CrossRef](#)]
49. Mazur, M.; Leary, M.; McMillan, M.; Sun, S.; Shidid, D.; Brandt, M. Mechanical properties of Ti6Al4V and AlSi12Mg lattice structures manufactured by Selective Laser Melting (SLM). In *Laser Additive Manufacturing*; Elsevier BV: Amsterdam, The Netherlands, 2017; pp. 119–161.
50. Pegues, J.; Roach, M.; Williamson, R.S.; Shamsaei, N. Surface roughness effects on the fatigue strength of additively manufactured Ti-6Al-4V. *Int. J. Fatigue* **2018**, *116*, 543–552. [[CrossRef](#)]
51. Torres, Y.; Sarria, P.; Gotor, F.J.; Gutiérrez, E.; Peon, E.; Beltrán, A.M.; González, J.E. Surface modification of Ti-6Al-4V alloys manufactured by selective laser melting: Microstructural and tribo-mechanical characterization. *Surf. Coatings Technol.* **2018**, *348*, 31–40. [[CrossRef](#)]
52. Xiao, L.; Song, W. Additively-manufactured functionally graded Ti-6Al-4V lattice structures with high strength under static and dynamic loading: Experiments. *Int. J. Impact Eng.* **2018**, *111*, 255–272. [[CrossRef](#)]
53. Bobbio, L.D.; Qin, S.; Dunbar, A.; Michaleris, P.; Beese, A.M. Characterization of the strength of support structures used in powder bed fusion additive manufacturing of Ti-6Al-4V. *Addit. Manuf.* **2017**, *14*, 60–68. [[CrossRef](#)]
54. Molaei, R.; Fatemi, A.; Phan, N. Significance of hot isostatic pressing (HIP) on multiaxial deformation and fatigue behavior of additive manufactured Ti-6Al-4V including build orientation and surface roughness effects. *Int. J. Fatigue* **2018**, *117*, 352–370. [[CrossRef](#)]
55. Elahinia, M.; Moghaddam, N.S.; Andani, M.T.; Amerinatanzi, A.; Bimber, B.A.; Hamilton, R.F. Fabrication of NiTi through additive manufacturing: A review. *Prog. Mater. Sci.* **2016**, *83*, 630–663. [[CrossRef](#)]
56. Mahmoudi, M.; Tapia, G.; Franco, B.; Ma, J.; Arróyave, R.; Karaman, I.; Elwany, A. On the printability and transformation behavior of nickel-titanium shape memory alloys fabricated using laser powder-bed fusion additive manufacturing. *J. Manuf. Process.* **2018**, *35*, 672–680. [[CrossRef](#)]
57. Moghaddam, N.S.; Saghaian, S.E.; Amerinatanzi, A.; Ibrahim, H.; Li, P.; Toker, G.P.; Karaca, H.E.; Elahinia, M. Anisotropic tensile and actuation properties of NiTi fabricated with selective laser melting. *Mater. Sci. Eng. A* **2018**, *724*, 220–230. [[CrossRef](#)]
58. Zhou, Q.; Hayat, M.D.; Chen, G.; Cai, S.; Qu, X.; Tang, H.; Cao, P. Selective electron beam melting of NiTi: Microstructure, phase transformation and mechanical properties. *Mater. Sci. Eng. A* **2019**, *744*, 290–298. [[CrossRef](#)]
59. Heiden, M.J.; Deibler, L.A.; Rodelas, J.M.; Koepke, J.R.; Tung, D.J.; Saiz, D.J.; Jared, B.H. Evolution of 316L stainless steel feedstock due to laser powder bed fusion process. *Addit. Manuf.* **2019**, *25*, 84–103. [[CrossRef](#)]
60. Choo, H.; Sham, K.-L.; Bohling, J.; Ngo, A.; Xiao, X.; Ren, Y.; Depond, P.J.; Matthews, M.J.; Garlea, E. Effect of laser power on defect, texture, and microstructure of a laser powder bed fusion processed 316L stainless steel. *Mater. Des.* **2019**, *164*, 107534. [[CrossRef](#)]
61. Atre, S.V.; Jangam, J.S.D.; Pasebani, S.; Badwe, S.; Stitzel, J.; Kate, K.H.; Gulsoy, O.; Atre, S.V. Effects of particle characteristics on the microstructure and mechanical properties of 17-4 PH stainless steel fabricated by laser-powder bed fusion. *Powder Technol.* **2018**, *331*, 192–203. [[CrossRef](#)]
62. Nath, S.D.; Irrinki, H.; Gupta, G.; Kearns, M.; Gulsoy, O.; Atre, S.V. Microstructure-property relationships of 420 stainless steel fabricated by laser-powder bed fusion. *Powder Technol.* **2019**, *343*, 738–746. [[CrossRef](#)]
63. Segura, I.; Murr, L.; Terrazas, C.; Bermudez, D.; Mireles, J.; Injeti, V.; Li, K.; Yu, B.; Misra, R.; Wicker, R. Grain boundary and microstructure engineering of Inconel 690 cladding on stainless-steel 316L using electron-beam powder bed fusion additive manufacturing. *J. Mater. Sci. Technol.* **2019**, *35*, 351–367. [[CrossRef](#)]

64. Wang, X.; Muñiz-Lerma, J.A.; Sánchez-Mata, O.; Shandiz, M.A.; Brochu, M. Microstructure and mechanical properties of stainless steel 316L vertical struts manufactured by laser powder bed fusion process. *Mater. Sci. Eng. A* **2018**, *736*, 27–40. [[CrossRef](#)]
65. Arisoy, Y.M.; Criales, L.E.; Özel, T. Modeling and simulation of thermal field and solidification in laser powder bed fusion of nickel alloy IN625. *Opt. Laser Technol.* **2019**, *109*, 278–292. [[CrossRef](#)]
66. Davies, S.; Jeffs, S.; Coleman, M.; Lancaster, R. Effects of heat treatment on microstructure and creep properties of a laser powder bed fused nickel superalloy. *Mater. Des.* **2018**, *159*, 39–46. [[CrossRef](#)]
67. Esmaeilzadeh, R.; Ali, U.; Keshavarzkermani, A.; Mahmoodkhani, Y.; Marzbanrad, E.; Toyserkani, E. On the effect of spatter particles distribution on the quality of Hastelloy X parts made by laser powder-bed fusion additive manufacturing. *J. Manuf. Process.* **2019**, *37*, 11–20. [[CrossRef](#)]
68. Zhao, X.; Chen, J.; Lin, X.; Huang, W. Study on microstructure and mechanical properties of laser rapid forming Inconel 718. *Mater. Sci. Eng. A* **2008**, *478*, 119–124. [[CrossRef](#)]
69. Zhang, D.; Feng, Z.; Wang, C.; Wang, W.; Liu, Z.; Niu, W. Comparison of microstructures and mechanical properties of Inconel 718 alloy processed by selective laser melting and casting. *Mater. Sci. Eng. A* **2018**, *724*, 357–367. [[CrossRef](#)]
70. Yoo, Y.S.J.; Book, T.A.; Sangid, M.D.; Kacher, J. Identifying strain localization and dislocation processes in fatigued Inconel 718 manufactured from selective laser melting. *Mater. Sci. Eng. A* **2018**, *724*, 444–451. [[CrossRef](#)]
71. Xu, Z.; Murray, J.; Hyde, C.; Clare, A. Effect of post processing on the creep performance of laser powder bed fused Inconel 718. *Addit. Manuf.* **2018**, *24*, 486–497. [[CrossRef](#)]
72. Xu, Z.; Hyde, C.; Tuck, C.; Clare, A. Creep behaviour of inconel 718 processed by laser powder bed fusion. *J. Mater. Process. Technol.* **2018**, *256*, 13–24. [[CrossRef](#)]
73. Wang, Z.; Guan, K.; Gao, M.; Li, X.Y.; Chen, X.; Zeng, X. The microstructure and mechanical properties of deposited-IN718 by selective laser melting. *J. Alloy. Compd.* **2012**, *513*, 518–523. [[CrossRef](#)]
74. Tillmann, W.; Schaak, C.; Nellesen, J.; Schaper, M.; Aydinöz, M.; Hoyer, K.-P. Hot isostatic pressing of IN718 components manufactured by selective laser melting. *Addit. Manuf.* **2017**, *13*, 93–102. [[CrossRef](#)]
75. Tao, P.; Li, H.; Huang, B.; Hu, Q.; Gong, S.; Xu, Q. The crystal growth, intercellular spacing and microsegregation of selective laser melted Inconel 718 superalloy. *Vacuum* **2019**, *159*, 382–390. [[CrossRef](#)]
76. Sun, S.-H.; Koizumi, Y.; Saito, T.; Yamanaka, K.; Li, Y.-P.; Cui, Y.; Chiba, A. Electron beam additive manufacturing of Inconel 718 alloy rods: Impact of build direction on microstructure and high-temperature tensile properties. *Addit. Manuf.* **2018**, *23*, 457–470. [[CrossRef](#)]
77. Sui, S.; Tan, H.; Chen, J.; Zhong, C.; Li, Z.; Fan, W.; Gasser, A.; Huang, W. The influence of Laves phases on the room temperature tensile properties of Inconel 718 fabricated by powder feeding laser additive manufacturing. *Acta Mater.* **2019**, *164*, 413–427. [[CrossRef](#)]
78. Sui, S.; Chen, J.; Fan, E.; Yang, H.; Lin, X.; Huang, W. The influence of Laves phases on the high-cycle fatigue behavior of laser additive manufactured Inconel 718. *Mater. Sci. Eng. A* **2017**, *695*, 6–13. [[CrossRef](#)]
79. Sheridan, L.; Scott-Emuakpor, O.E.; George, T.; Gockel, J.E. Relating porosity to fatigue failure in additively manufactured alloy 718. *Mater. Sci. Eng. A* **2018**, *727*, 170–176. [[CrossRef](#)]
80. Sangid, M.D.; Book, T.A.; Naragani, D.; Rotella, J.; Ravi, P.; Finch, A.; Kenesei, P.; Park, J.-S.; Sharma, H.; Almer, J.; et al. Role of heat treatment and build orientation in the microstructure sensitive deformation characteristics of IN718 produced via SLM additive manufacturing. *Addit. Manuf.* **2018**, *22*, 479–496. [[CrossRef](#)]
81. Raza, T.; Andersson, J.; Svensson, L.-E. Microstructure of SLM Alloy 718 in as-manufactured and Post Heat Treated Condition. *Procedia Manuf.* **2018**, *25*, 450–458. [[CrossRef](#)]
82. Qi, H.; Azer, M.; Ritter, A. Studies of Standard Heat Treatment Effects on Microstructure and Mechanical Properties of Laser Net Shape Manufactured INCONEL 718. *Met. Mater. Trans. A* **2009**, *40*, 2410–2422. [[CrossRef](#)]
83. Pröbstle, M.; Neumeier, S.; Hopfenmüller, J.; Freund, L.; Niendorf, T.; Schwarze, D.; Göken, M. Superior creep strength of a nickel-based superalloy produced by selective laser melting. *Mater. Sci. Eng. A* **2016**, *674*, 299–307. [[CrossRef](#)]
84. Ni, M.; Chen, C.; Wang, X.; Wang, P.; Li, R.; Zhang, X.; Zhou, K. Anisotropic tensile behavior of in situ precipitation strengthened Inconel 718 fabricated by additive manufacturing. *Mater. Sci. Eng. A* **2017**, *701*, 344–351. [[CrossRef](#)]

85. Ma, D.; Stoica, A.D.; Wang, Z.; Beese, A.M. Crystallographic texture in an additively manufactured nickel-base superalloy. *Mater. Sci. Eng. A* **2017**, *684*, 47–53. [CrossRef]
86. Kuo, Y.-L.; Horikawa, S.; Takehi, K. The effect of interdendritic δ phase on the mechanical properties of Alloy 718 built up by additive manufacturing. *Mater. Des.* **2017**, *116*, 411–418. [CrossRef]
87. Konečná, R.; Kunz, L.; Nicoletto, G.; Bača, A. Long fatigue crack growth in Inconel 718 produced by selective laser melting. *Int. J. Fatigue* **2016**, *92*, 499–506. [CrossRef]
88. Juillet, C.; Oudriss, A.; Balmain, J.; Feaugas, X.; Pedraza, F. Characterization and oxidation resistance of additive manufactured and forged IN718 Ni-based superalloys. *Corros. Sci.* **2018**, *142*, 266–276. [CrossRef]
89. Haines, M.; Plotkowski, A.; Frederick, C.; Schwalbach, E.; Babu, S. A sensitivity analysis of the columnar-to-equiaxed transition for Ni-based superalloys in electron beam additive manufacturing. *Comput. Mater. Sci.* **2018**, *155*, 340–349. [CrossRef]
90. Farber, B.; Small, K.A.; Allen, C.; Causton, R.J.; Nichols, A.; Simbolick, J.; Taheri, M.L. Correlation of mechanical properties to microstructure in Inconel 718 fabricated by Direct Metal Laser Sintering. *Mater. Sci. Eng. A* **2018**, *712*, 539–547. [CrossRef]
91. Deng, D.; Peng, R.L.; Brodin, H.; Moverare, J. Microstructure and mechanical properties of Inconel 718 produced by selective laser melting: Sample orientation dependence and effects of post heat treatments. *Mater. Sci. Eng. A* **2018**, *713*, 294–306. [CrossRef]
92. Deng, D.; Moverare, J.; Peng, R.L.; Söderberg, H. Microstructure and anisotropic mechanical properties of EBM manufactured Inconel 718 and effects of post heat treatments. *Mater. Sci. Eng. A* **2017**, *693*, 151–163. [CrossRef]
93. Choi, J.-P.; Shin, G.-H.; Yang, S.; Yang, D.-Y.; Lee, J.-S.; Brochu, M.; Yu, J.-H. Densification and microstructural investigation of Inconel 718 parts fabricated by selective laser melting. *Powder Technol.* **2017**, *310*, 60–66. [CrossRef]
94. Cakmak, E.; Kirka, M.M.; Watkins, T.; Cooper, R.C.; An, K.; Choo, H.; Wu, W.; Dehoff, R.R.; Babu, S. Microstructural and micromechanical characterization of IN718 theta shaped specimens built with electron beam melting. *Acta Mater.* **2016**, *108*, 161–175. [CrossRef]
95. Prithvirajan, V.; Sangid, M.D. The role of defects and critical pore size analysis in the fatigue response of additively manufactured IN718 via crystal plasticity. *Mater. Des.* **2018**, *150*, 139–153. [CrossRef]
96. Kreitzberg, A.; Brailovski, V.; Turenne, S. Effect of heat treatment and hot isostatic pressing on the microstructure and mechanical properties of Inconel 625 alloy processed by laser powder bed fusion. *Mater. Sci. Eng. A* **2017**, *689*, 1–10. [CrossRef]
97. Kreitzberg, A.; Brailovski, V.; Turenne, S. Elevated temperature mechanical behavior of IN625 alloy processed by laser powder-bed fusion. *Mater. Sci. Eng. A* **2017**, *700*, 540–553. [CrossRef]
98. Huynh, L.; Rotella, J.; Sangid, M.D. Fatigue behavior of IN718 microtrusses produced via additive manufacturing. *Mater. Des.* **2016**, *105*, 278–289. [CrossRef]
99. Chen, Z.; Chen, S.; Wei, Z.; Zhang, L.; Wei, P.; Lu, B.; Zhang, S.; Xiang, Y. Anisotropy of nickel-based superalloy K418 fabricated by selective laser melting. *Prog. Nat. Sci.* **2018**, *28*, 496–504. [CrossRef]
100. Leary, M.; Mazur, M.; Williams, H.; Yang, E.; Alghamdi, A.; Lozanovski, B.; Zhang, X.; Shidid, D.; Farahbod-Sternahl, L.; Witt, G.; et al. Inconel 625 lattice structures manufactured by selective laser melting (SLM): Mechanical properties, deformation and failure modes. *Mater. Des.* **2018**, *157*, 179–199. [CrossRef]
101. Qin, H.; Fallah, V.; Dong, Q.; Brochu, M.; Daymond, M.R.; Gallerneault, M. Solidification pattern, microstructure and texture development in Laser Powder Bed Fusion (LPBF) of Al10SiMg alloy. *Mater. Charact.* **2018**, *145*, 29–38. [CrossRef]
102. Uddin, S.Z.; Murr, L.; Terrazas, C.A.; Morton, P.; Roberson, D.A.; Wicker, R.B. Processing and characterization of crack-free aluminum 6061 using high-temperature heating in laser powder bed fusion additive manufacturing. *Addit. Manuf.* **2018**, *22*, 405–415. [CrossRef]
103. Prasad, K.; Sarkar, R.; Ghosal, P.; Kumar, V. Simultaneous creep–fatigue damage accumulation of forged turbine disc of IN 718 superalloy. *Mater. Sci. Eng. A* **2013**, *572*, 1–7. [CrossRef]
104. Reed, R.C. *The Superalloys: Fundamentals and Applications*; C.U. Press: Cambridge, UK, 2006.
105. Sun, J.; Yuan, H. Life assessment of multiaxial thermomechanical fatigue of a nickel-based superalloy Inconel 718. *Int. J. Fatigue* **2019**, *120*, 228–240. [CrossRef]
106. International, A.W. Inconel 718. Available online: <https://www.alloywire.com/products/inconel-718/> (accessed on 1 June 2020).

107. Akca, E.; Gürsel, A. A Review on Superalloys and IN718 Nickel-Based INCONEL Superalloy. *Period. Eng. Nat. Sci.* **2015**, *3*. [[CrossRef](#)]
108. Cao, G.; Sun, T.; Wang, C.; Li, X.; Liu, M.; Zhang, Z.; Hu, P.; Russell, A.; Schneider, R.; Gerthsen, D.; et al. Investigations of γ' , γ'' and δ precipitates in heat-treated Inconel 718 alloy fabricated by selective laser melting. *Mater. Charact.* **2018**, *136*, 398–406. [[CrossRef](#)]
109. Amato, K.; Gaytan, S.; Murr, L.; Martinez, E.C.; Shindo, P.; Hernandez, J.; Collins, S.F.; Medina, F.S. Microstructures and mechanical behavior of Inconel 718 fabricated by selective laser melting. *Acta Mater.* **2012**, *60*, 2229–2239. [[CrossRef](#)]
110. Mostafa, A.; Rubio, I.P.; Brailovski, V.; Jahazi, M.; Medraj, M. Structure, Texture and Phases in 3D Printed IN718 Alloy Subjected to Homogenization and HIP Treatments. *Metals* **2017**, *7*, 196. [[CrossRef](#)]
111. Strößner, J.; Terock, M.; Glatzel, U. Mechanical and Microstructural Investigation of Nickel-Based Superalloy IN718 Manufactured by Selective Laser Melting (SLM). *Adv. Eng. Mater.* **2015**, *17*, 1099–1105. [[CrossRef](#)]
112. Tonelli, L.; Fortunato, A.; Ceschini, L. CoCr alloy processed by Selective Laser Melting (SLM): Effect of Laser Energy Density on microstructure, surface morphology, and hardness. *J. Manuf. Process.* **2020**, *52*, 106–119. [[CrossRef](#)]
113. Guo, M.; Gu, D.; Xi, L.; Du, L.; Zhang, H.; Zhang, J. Formation of scanning tracks during Selective Laser Melting (SLM) of pure tungsten powder: Morphology, geometric features and forming mechanisms. *Int. J. Refract. Met. Hard Mater.* **2019**, *79*, 37–46. [[CrossRef](#)]
114. Khan, H.; Dirikolu, M.H.; Koc, E.; Oter, Z.C. Numerical investigation of heat current study across different platforms in SLM processed multi-layer AlSi10Mg. *Optik* **2018**, *170*, 82–89. [[CrossRef](#)]
115. Gribbin, S.; Ghorbanpour, S.; Ferreri, N.C.; Bicknell, J.; Tsukrov, I.; Knezevic, M. Role of grain structure, grain boundaries, crystallographic texture, precipitates, and porosity on fatigue behavior of Inconel 718 at room and elevated temperatures. *Mater. Charact.* **2019**, *149*, 184–197. [[CrossRef](#)]
116. Chlebus, E.; Gruber, K.; Kuźnicka, B.; Kurzac, J.; Kurzynowski, T. Effect of heat treatment on the microstructure and mechanical properties of Inconel 718 processed by selective laser melting. *Mater. Sci. Eng. A* **2015**, *639*, 647–655. [[CrossRef](#)]
117. As, S.; Skallerud, B.; Tveiten, B. Surface roughness characterization for fatigue life predictions using finite element analysis. *Int. J. Fatigue* **2008**, *30*, 2200–2209. [[CrossRef](#)]
118. Gockel, J.; Sheridan, L.; Koerper, B.; Whip, B. The influence of additive manufacturing processing parameters on surface roughness and fatigue life. *Int. J. Fatigue* **2019**, *124*, 380–388. [[CrossRef](#)]
119. Balachandramurthi, A.R.; Moverare, J.; Dixit, N.; Pederson, R. Influence of defects and as-built surface roughness on fatigue properties of additively manufactured Alloy 718. *Mater. Sci. Eng. A* **2018**, *735*, 463–474. [[CrossRef](#)]
120. Yadollahi, A.; Mahtabi, M.J.; Khalili, A.; Doude, H.; Newman, J. Fatigue life prediction of additively manufactured material: Effects of surface roughness, defect size, and shape. *Fatigue Fract. Eng. Mater. Struct.* **2018**, *41*, 1602–1614. [[CrossRef](#)]
121. Kobayashi, K.; Yamaguchi, K.; Hayakawa, M.; Kimura, M. Grain size effect on high-temperature fatigue properties of alloy 718. *Mater. Lett.* **2005**, *59*, 383–386. [[CrossRef](#)]
122. Zhang, Y.; Yang, L.; Chen, T.; Zhang, W.; Huang, X.; Dai, J. Investigation on the optimized heat treatment procedure for laser fabricated IN718 alloy. *Opt. Laser Technol.* **2017**, *97*, 172–179. [[CrossRef](#)]
123. Anderson, M.; Thielin, A.-L.; Bridier, F.; Bocher, P.; Savoie, J. δ Phase precipitation in Inconel 718 and associated mechanical properties. *Mater. Sci. Eng. A* **2017**, *679*, 48–55. [[CrossRef](#)]
124. Mitra, J.; Banerjee, S.; Tewari, R.; Dey, G.K. Fracture behavior of Alloy 625 with different precipitate microstructures. *Mater. Sci. Eng. A* **2013**, *574*, 86–93. [[CrossRef](#)]
125. Shankar, V.; Rao, K.B.S.; Mannan, S. Microstructure and mechanical properties of Inconel 625 superalloy. *J. Nucl. Mater.* **2001**, *288*, 222–232. [[CrossRef](#)]
126. Mahadevan, S.; Nalawade, S.; Singh, J.B.; Verma, A.; Paul, B.; Ramaswamy, K. Evolution of δ Phase Microstructure in Alloy 718. In Proceedings of the Superalloy 718 and Derivatives, Pittsburgh, PA, USA, 10–13 October 2012.
127. Li, J.; Zhao, Z.; Bai, P.; Qu, H.; Liu, B.; Li, L.; Wu, L.; Guan, R.; Liu, H.; Guo, Z. Microstructural evolution and mechanical properties of IN718 alloy fabricated by selective laser melting following different heat treatments. *J. Alloy. Compd.* **2019**, *772*, 861–870. [[CrossRef](#)]

128. Li, S.; Yang, J.; Zhuang, J.; Deng, Q.; Du, J.; Xie, X.; Li, B.; Xu, Z.; Cao, Z.; Su, Z.; et al. The Effect of Delta-Phase on Crack Propagation under Creep and Fatigue Conditions in Alloy 718. *Superalloys 2008* **1994**, *718*, 625–706. [[CrossRef](#)]
129. An, J.; Wang, L.; Liu, Y.; Cai, W.; Song, X. The role of δ phase for fatigue crack propagation behavior in a Ni base superalloy at room temperature. *Mater. Sci. Eng. A* **2017**, *684*, 312–317. [[CrossRef](#)]
130. Gao, Y.; Zhang, D.; Cao, M.; Chen, R.; Feng, Z.; Poprawe, R.; Schleifenbaum, J.H.; Ziegler, S. Effect of δ phase on high temperature mechanical performances of Inconel 718 fabricated with SLM process. *Mater. Sci. Eng. A* **2019**, *767*, 138–327. [[CrossRef](#)]
131. Schirra, J.; Caless, R.; Hatala, R. The Effect of Laves Phase on the Mechanical Properties of Wrought and Cast + HIP Inconel 718. *Superalloys 2008* **1991**, *718*, 375–388. [[CrossRef](#)]
132. Chen, Y.; Guo, Y.; Xu, M.; Ma, C.; Zhang, Q.; Wang, L.; Jianhua, Y.; Li, Z. Study on the element segregation and Laves phase formation in the laser metal deposited IN718 superalloy by flat top laser and gaussian distribution laser. *Mater. Sci. Eng. A* **2019**, *754*, 339–347. [[CrossRef](#)]
133. Radhakrishna, C.; Rao, K.P. The formation and control of Laves phase in superalloy 718 welds. *J. Mater. Sci.* **1997**, *32*, 1977–1984. [[CrossRef](#)]
134. Li, J.; Shrestha, S.L.; Yan, L.; Li, Z.; Xintai, Z. The formation of eutectic phases and hot cracks in one Ni–Mo–Cr superalloy. *Mater. Des.* **2016**, *93*, 324–333. [[CrossRef](#)]
135. You, X.; Tan, Y.; Shi, S.; Yang, J.-M.; Wang, Y.; Li, J.; You, Q. Effect of solution heat treatment on the precipitation behavior and strengthening mechanisms of electron beam smelted Inconel 718 superalloy. *Mater. Sci. Eng. A* **2017**, *689*, 257–268. [[CrossRef](#)]
136. Tucho, W.M.; Cuvillier, P.; Sjolyst-Kverneland, A.; Hansen, V. Microstructure and hardness studies of Inconel 718 manufactured by selective laser melting before and after solution heat treatment. *Mater. Sci. Eng. A* **2017**, *689*, 220–232. [[CrossRef](#)]
137. Wang, X.; Chou, K. Effects of thermal cycles on the microstructure evolution of Inconel 718 during selective laser melting process. *Addit. Manuf.* **2017**, *18*, 1–14. [[CrossRef](#)]
138. Liu, F.; Lyu, F.; Liu, F.; Lin, X.; Huang, C. Laves phase control of inconel 718 superalloy fabricated by laser direct energy deposition via δ aging and solution treatment. *J. Mater. Res. Technol.* **2020**, *9*, 9753–9765. [[CrossRef](#)]
139. Xie, H.; Yang, K.; Li, F.; Sun, C.; Yu, Z. Investigation on the Laves phase formation during laser cladding of IN718 alloy by CA-FE. *J. Manuf. Process.* **2020**, *52*, 132–144. [[CrossRef](#)]
140. Huang, W.; Yang, J.; Yang, H.; Jing, G.; Wang, Z.; Zeng, X. Heat treatment of Inconel 718 produced by selective laser melting: Microstructure and mechanical properties. *Mater. Sci. Eng. A* **2019**, *750*, 98–107. [[CrossRef](#)]
141. Gallmeyer, T.G.; Moorthy, S.; Kappes, B.B.; Mills, M.J.; Amin-Ahmadi, B.; Stebner, A.P. Knowledge of process-structure-property relationships to engineer better heat treatments for laser powder bed fusion additive manufactured Inconel 718. *Addit. Manuf.* **2020**, *31*, 100977. [[CrossRef](#)]
142. ASTM E8/E8M. *Standard Test Methods for Tension Testing of Metallic Materials*; ASTM International: West Conshohocken, PA, USA, 2016.
143. Ahmad, B.; Van Der Veen, S.; Fitzpatrick, M.E.; Guo, H. Residual stress evaluation in selective-laser-melting additively manufactured titanium (Ti-6Al-4V) and inconel 718 using the contour method and numerical simulation. *Addit. Manuf.* **2018**, *22*, 571–582. [[CrossRef](#)]
144. Konečná, R.; Nicoletto, G.; Kunz, L.; Bača, A. Microstructure and directional fatigue behavior of Inconel 718 produced by selective laser melting. *Procedia Struct. Integr.* **2016**, *2*, 2381–2388. [[CrossRef](#)]
145. Moussaoui, K.; Rubio, W.; Mousseigne, M.; Sultan, T.; Rezai, F. Effects of Selective Laser Melting additive manufacturing parameters of Inconel 718 on porosity, microstructure and mechanical properties. *Mater. Sci. Eng. A* **2018**, *735*, 182–190. [[CrossRef](#)]
146. Kok, Y.; Tan, X.; Wang, P.; Nai, M.; Loh, N.; Liu, E.; Tor, S. Anisotropy and heterogeneity of microstructure and mechanical properties in metal additive manufacturing: A critical review. *Mater. Des.* **2018**, *139*, 565–586. [[CrossRef](#)]
147. Maleki, E.; Bagherifard, S.; Bandini, M.; Guagliano, M. Surface post-treatments for metal additive manufacturing: Progress, challenges, and opportunities. *Addit. Manuf.* **2020**, 101619. [[CrossRef](#)]
148. Shuai, C.; Yang, Y.; Feng, P.; Peng, S.; Guo, W.; Min, A.; Gao, C. A multi-scale porous scaffold fabricated by a combined additive manufacturing and chemical etching process for bone tissue engineering. *Int. J. Bioprint.* **2018**, *4*, 133. [[CrossRef](#)]

149. Ali, U.; Fayazfar, H.; Ahmed, F.; Toyserkani, E. Internal surface roughness enhancement of parts made by laser powder-bed fusion additive manufacturing. *Vacuum* **2020**, *177*, 109–314. [[CrossRef](#)]
150. Almangour, B.; Yang, J.-M. Improving the surface quality and mechanical properties by shot-peening of 17-4 stainless steel fabricated by additive manufacturing. *Mater. Des.* **2016**, *110*, 914–924. [[CrossRef](#)]
151. Zhuang, W.; Liu, Q.; Djugum, R.; Sharp, P.; Paradowska, A. Deep surface rolling for fatigue life enhancement of laser clad aircraft aluminium alloy. *Appl. Surf. Sci.* **2014**, *320*, 558–562. [[CrossRef](#)]
152. Luo, S.; He, W.; Chen, K.; Nie, X.; Zhou, L.; Li, Y.; Sihai, L.; Weifeng, H.; Kai, C.; Xiangfan, N.; et al. Regain the fatigue strength of laser additive manufactured Ti alloy via laser shock peening. *J. Alloys Compd.* **2018**, *750*, 626–635. [[CrossRef](#)]
153. Clauer, A.; Koucky, J. Laser Shock Processing Increases the Fatigue Life of Metal Parts. *Mater. Process. Rep.* **1991**, *6*, 3–5. [[CrossRef](#)]
154. Sundar, R.; Ganesh, P.; Gupta, R.K.; Ragvendra, G.; Pant, B.K.; Vivekanand, K.; Ranganathan, K.; Kaul, R.; Bindra, K.S. Laser Shock Peening and its Applications: A Review. *Lasers Manuf. Mater. Process.* **2019**, *6*, 424–463. [[CrossRef](#)]
155. Zhang, Y.; You, J.; Lu, J.; Cui, C.; Jiang, Y.; Ren, X. Effects of laser shock processing on stress corrosion cracking susceptibility of AZ31B magnesium alloy. *Surf. Coatings Technol.* **2010**, *204*, 3947–3953. [[CrossRef](#)]
156. Lu, J.; Luo, K.; Zhang, Y.; Sun, G.; Gu, Y.; Zhou, J.; Ren, X.; Zhang, X.; Zhang, L.; Chen, K.; et al. Grain refinement mechanism of multiple laser shock processing impacts on ANSI 304 stainless steel. *Acta Mater.* **2010**, *58*, 5354–5362. [[CrossRef](#)]
157. Altenberger, I.; Stach, E.; Liu, G.; Nalla, R.; Ritchie, R.O. An in situ transmission electron microscope study of the thermal stability of near-surface microstructures induced by deep rolling and laser-shock peening. *Scr. Mater.* **2003**, *48*, 1593–1598. [[CrossRef](#)]
158. Altenberger, I.; Nalla, R.K.; Sano, Y.; Wagner, L.; Ritchie, R.O. On the effect of deep-rolling and laser-peening on the stress-controlled low- and high-cycle fatigue behavior of Ti–6Al–4V at elevated temperatures up to 550 °C. *Int. J. Fatigue* **2012**, *44*, 292–302. [[CrossRef](#)]
159. Dhakal, B.; Swaroop, S. Effect of laser shock peening on mechanical and microstructural aspects of 6061-T6 aluminum alloy. *J. Mater. Process. Technol.* **2020**, *282*, 116640. [[CrossRef](#)]
160. Prevey, P.S.; Hornbach, D.J.; Mason, P.W. Thermal residual stress relaxation and distortion in surface enhanced gas turbine components. In Proceedings of the 17th Heat Treating Society Conference and 1st International Induction Heat Treating Symposium, Indianapolis, IN, USA, 15–18 September 1997.
161. Prevey, P.S. The effect of cold work on the thermal stability of residual compression in surface enhanced IN718. In Proceedings of the 20th ASM Heat Treating Society Conference, St. Louis, MO, USA, 9–12 October 2000.
162. Kattoura, M.; Mannava, S.R.; Qian, D.; Vasudevan, V.K. Effect of laser shock peening on elevated temperature residual stress, microstructure and fatigue behavior of ATI 718Plus alloy. *Int. J. Fatigue* **2017**, *104*, 366–378. [[CrossRef](#)]
163. Kumar, N.N.; Yadav, A.C.; Raja, K.; Naiju, C.; Prabhakaran, S.; Kalainathan, S. Laser Shock Peening on Al-Si10-Mg Produced by DMLS Technique. *Mater. Today Proc.* **2020**, *22*, 2916–2925. [[CrossRef](#)]
164. Kalentics, N.; de Seijas, M.O.V.; Griffiths, S.; Leinenbach, C.; Logé, R.E. 3D laser shock peening—A new method for improving fatigue properties of selective laser melted parts. *Addit. Manuf.* **2020**, *33*. [[CrossRef](#)]
165. Kalentics, N.; Boillat, E.; Peyre, P.; Ćirić-Kostić, S.; Bogojević, N.; Logé, R.E. Tailoring residual stress profile of Selective Laser Melted parts by Laser Shock Peening. *Addit. Manuf.* **2017**, *16*, 90–97. [[CrossRef](#)]

Publisher's Note: MDPI stays neutral with regard to jurisdictional claims in published maps and institutional affiliations.



© 2020 by the authors. Licensee MDPI, Basel, Switzerland. This article is an open access article distributed under the terms and conditions of the Creative Commons Attribution (CC BY) license (<http://creativecommons.org/licenses/by/4.0/>).

Appendix F

Publication 3

Assessment of Laser Shock Peening on Additive Manufactured Inconel 718 for Aerospace Application

Ching Kiat Yong ^{a,c,*}, Darren J Hughes ^a, Elspeth M Keating ^a, Thomas Connolley ^b, Geoff West ^a, Gregory J Gibbons ^a, Chow Cher Wong ^c

a WMG, University of Warwick, Coventry CV4 7AL, United Kingdom

b Diamond Light Source, Harwell Science and Innovation Campus, Didcot, Oxfordshire, UK

c Advanced Remanufacturing and Technology Centre (ARTC), CleanTech Two, Singapore 637143, Singapore

Email: ching-kiat.yong@warwick.ac.uk

* Corresponding author

Abstract

Laser shock peening was introduced onto additive manufactured Inconel 718 in an attempt to replicate current aeroengine manufacturing processes. Deep compressive stresses and no cold work was observed on the surface, tantilising and timely results in the push to adopt additive manufacturing as a step-change in production.

1. Introduction

Additive Manufacturing (AM) has received significant recent attention due to its potential benefit of producing complex component geometries in a shorter time and with reduced waste, compared to conventional machining processes [1, 2]. In particular, AM technology brings a tremendous advantage for superalloys such as Inconel 718 (IN718) as it removes the possibility of work hardening the component [5], facilitating manufacturers to fabricate components with intricate geometries. IN718 is the most commonly used nickel-based alloy in the aerospace industry due to its superior mechanical properties at elevated temperatures and has been widely used in the turbine section of aeroengines [3-5]. AM processes have been used for the production of commercial components but are susceptible to defects including micro-porosity and detrimental tensile stress [6-8]. These defects are particularly problematic in near-surface regions of safety critical components where crack initiation may occur which lead to catastrophic failure. Efforts have been made to limit these defects through the use of heat treatment [6, 9] and hot isostatic pressing (HIP-ing) [10]. However, results have been mixed, and no significant progress has been made on improving the quality of AM IN718.

Laser shock peening (LSP) is a surface treatment that employs a pulsed laser with high power density onto the surface of a component [11]. With a layer of black light-absorbing tape and water applied to the targeted surface, shock waves can be generated due to the laser-matter interaction produced by the treatment. These shock waves create high pressures to deform the surface layer, creating beneficial compressive residual stresses [12]. LSP has been shown to outperform other surface enhancement techniques due to producing remarkably low cold work on the surface [13]. LSP treated material is much more capable of withstanding plastic straining before failure due to its formation of dislocation entanglements and slip bands that create a barrier that hinders the nucleation and propagation of fatigue cracks [14]. In conventionally machined components subjected to LSP treatment, significant benefits have been show due to a deep protective compressive near-surface stress field [15]. A thorough comparison of between LSP wrought and LSP AM IN718 residual stress state were made elsewhere. Interested readers could refer to the paper written by the author [16].

This paper considers the application of LSP as a process to improve the performance of AM IN718 structures for aero-engine applications. In particular, an investigation is made as to whether the benefits of a near-surface compressive residual stress field can be realised in AM components. Depth-wise residual stress determination was performed using a state-of-the-art high intensity synchrotron X-radiation diffraction (SXR) method. The authors believe the findings in this paper provide valuable insight for aero-engine manufacturers to consider LSP as a viable process to enable the use of AM IN718 in high-performance aeroengine components.

2. Experimental procedures and material specifications

2.1. Production of samples

Table 1 Chemical composition in wt % of IN718 alloy

| Ni | Cr | Nb | Mo | Ti | Al | Co | Cu | C | Si | Mn | Fe |
|----|----|------|------|------|------|----|------|------|------|------|-----|
| 50 | 17 | 4.70 | 2.80 | 0.60 | 0.20 | 1 | 0.30 | 0.08 | 0.35 | 0.35 | bal |

AM IN718 samples used in the present study were prepared using Powder Bed Fusion (PBF), built using an EOS M290 (EOS GmbH, Germany) with a 400 W fibre laser. Samples were built vertically along the y-axis (see Figure 1) at 67° to the XZ plane. The chemical composition of the powder (EOS GmbH, Germany) used for manufacture is provided in Table 1 [17]. Specimens were heat treated according to Aerospace Material Specifications (AMS) 5663 [17] and wire cut via electro-discharge machining from the base plate after the heat treatment. The samples were designed to facilitate access to the LSP machine, tensile and fatigue testing, and high spatial resolution SXR measurements. A flat dog-boned geometry was used as illustrated in Figure 1. Its size and geometry conformed to the prescription for test pieces with a continuous radius between gripping ends as specified in BS EN 3987:2009 [18]. Specimens were also prepared from a wrought IN718 alloy of the same chemical composition. Both AM and wrought specimens were ground and polished to 0.2 μm Ra as per EN 3987:2009 standard. LSP was performed with single pulse impact and deionised water flowing onto the targeted area as a transparent confining media. For the selected geometry, applying the LSP process on the opposite sides of the section is recommended to balance the generated force. Two-sided peening is used to avoid harmful effects such as spalling and fracture. A laser power density of 7.1 GW/cm^2 was deemed to be the lowest cost option following a process reported elsewhere [16].

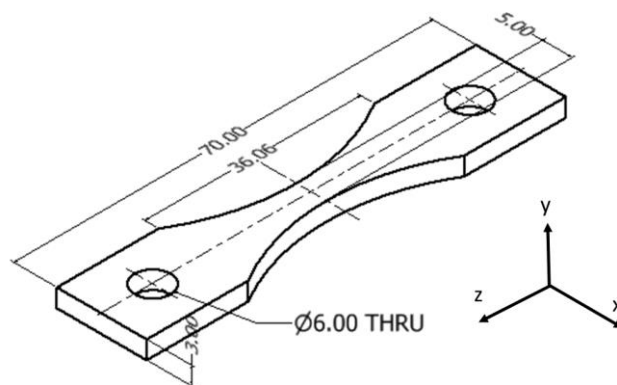


Figure 1 Geometry of the flat dog-boned specimens

2.2. Phase identification using Powder Cell

Phases were confirmed by full-profile analysis using the PowderCell software [19] and the individual phases in the alloys were determined from crystallographic data in the literature [20].

2.3. Residual stress measurement using synchrotron X-ray diffraction

The present work utilised the I12 JEEP beamline at Diamond Light Source (Oxford, UK) [21] for strain analysis, operating with a beam energy around 123 keV, correlating to an X-ray wavelength of approximately 0.1 Å. The incident beam was defined using precise, calibrated slits to be 0.1 mm wide x 0.1 high. The specimens were mounted with the XZ plane (see Figure 1) oriented horizontally. Thus the peened surfaces were oriented parallel to the beam direction. Figure 2a shows the experimental setup at the DIAMOND facility. Figure 2b shows the progression of the specimens through the beam to obtain depth-wise diffraction data.

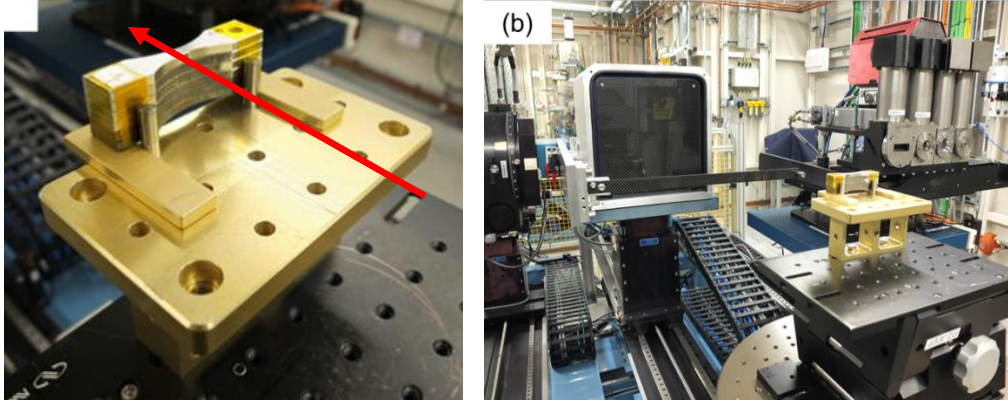


Figure 2 (a) Samples stacked together on the I12 facility with the X-ray beam direction as shown. (b) Samples were scanned vertically through the beam and showing translation of the specimens through the beam.

The effective diffraction volume (gauge volume) was therefore defined by both the incident slits and the full width of the specimens (5 mm). A two-dimensional Pilatus 3 X CdTe 2M detector was employed to collect diffraction images as the specimen was scanned through the beam. A step-size of 10 µm was used for all specimens and a collection time of 10 seconds was deemed appropriate following initial tests.

Reflections from the {311} planes are an appropriate choice to convert lattice strains to macroscopic stress applied in polycrystalline nickel-base superalloys [22]. Lattice strains measured can be converted via standard solid mechanics theory [23];

$$\sigma_x = \frac{E}{(1-\nu)(1-2\nu)} [(1-\nu)\varepsilon_x + \nu(\varepsilon_y + \varepsilon_z)] \quad (1)$$

where σ is the stress state for the corresponding x, y and z directions, elastic modulus $E = 170$ MPa and was gathered from various literature sources [17, 24, 25], and Poisson's ratio $\nu = 0.29$ [24, 25]. The stress component in the through-thickness direction (y-axis) is assumed to be zero and the in-plane stress (x and z-axis) is isotropic [26]. In this case, it is possible to calculate the (usually of most interest) in-plane stress from a single strain data;

$$\sigma = E \frac{(\varepsilon + \nu\varepsilon)}{(1-\nu^2)} \quad (2)$$

3. Results and discussion

3.1. Phase identification

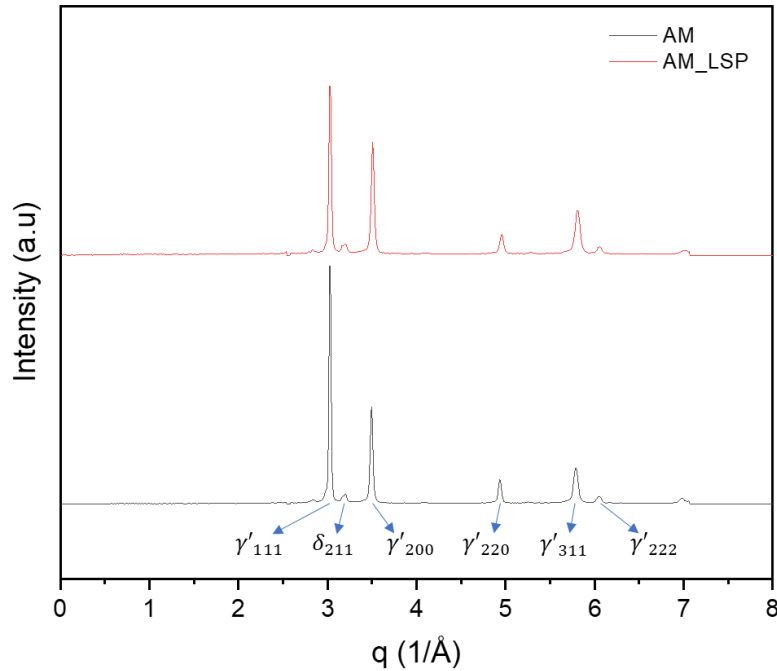


Figure 3 XRD spectra with identified phases for pristine (AM) and laser shock peened (AM_LSP) samples

Figure 3 displays the indexed and fitted AM and AM_LSP diffraction patterns. Literature shows, δ_{211} is more prominent in the AM IN718 specimens than their wrought counterparts [27] and applying LSP treatment does not affect the phase distribution. This is a crucial observation as IN718 is a precipitation-strengthened nickel-based superalloy with γ'' as the main phase contributing to its excellent high-temperature strength [28]. δ precipitates derived from metastable γ'' can be detrimental to the overall mechanical properties of the alloy [29]. The presence of these precipitates can degrade the material performance as it will trigger intergranular cracking [30, 31]. On the other hand, the formation of intragranular δ precipitates was seen to harden the material [29], which is commonly observed in AM IN718. Thus, the ratio between intragranular and intergranular δ precipitates can be a critical parameter in optimising the fatigue properties of AM IN718. Fortunately, the use of LSP do not alter the precipitates and advance microstructural techniques are advised to identify these precipitates' location and morphology in the sample.

3.2. Stress field

The through-thickness stress measurements of AM and AM_LSP are illustrated in Figure 4. As the depth increased, the stresses became less compressive and its effect reached up to 625 μm from the surface. The highest compressive residual stress of AM_LSP is observed at 50 μm from the surface with a value of -471 MPa on one side of the specimen and 100 μm from the surface with a value of -452 MPa on the another side.

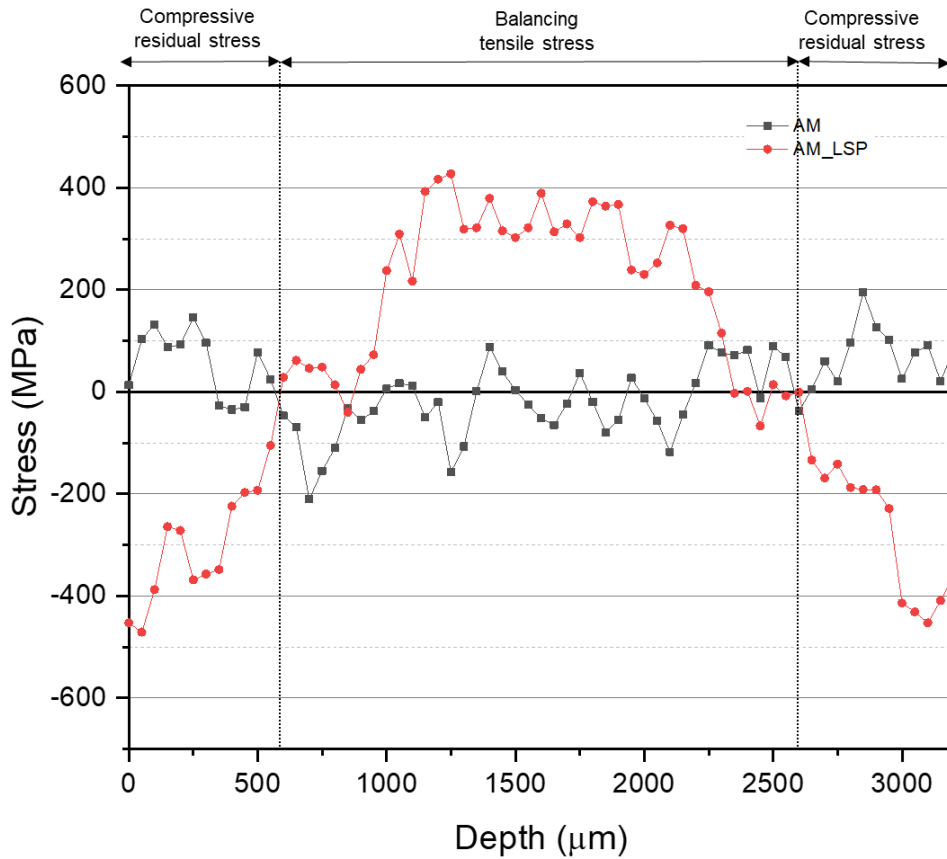


Figure 4 Residual stress profile of pristine (AM) and laser shock peened (AM_LSP) samples

The sum of forces must be equal to zero as no external forces are present in the samples. The balancing tensile stresses are found between the depth region of 625 μm to 2600 μm and goes up to 427 MPa, as seen in Figure 4. The maximum balancing tensile stress must not become large enough to create early internal failures. Wagner [32] reported that high-cycle fatigue cracks often nucleate in the subsurface level of where the balancing tensile stress resides. The detrimental effect can reduce the overall effect of the surface enhancement process, making the enhanced material weaker than its pristine state.

3.3. Full width half maximum profile

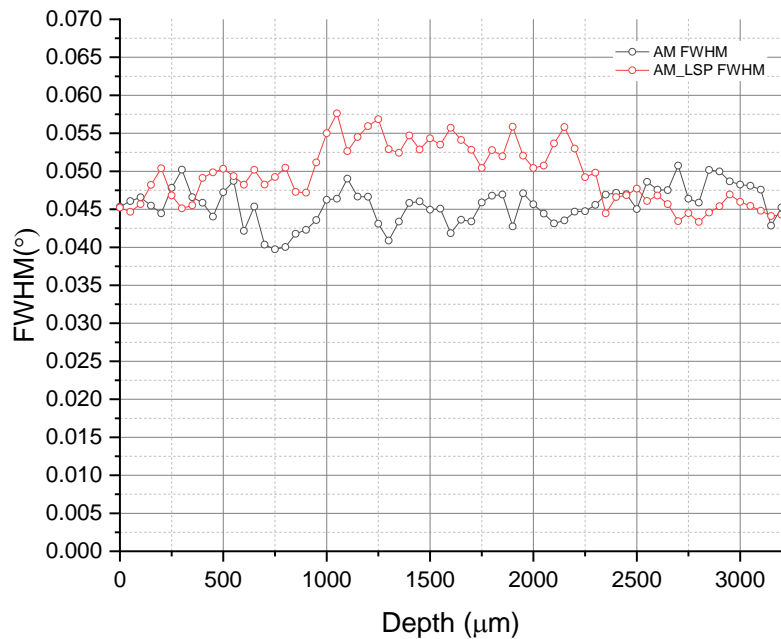


Figure 5 Full width half maximum of pristine (AM) and laser shock peened (AM_LSP) samples

Full width half maximum (FWHM) value was used as a measure of the relative dislocation density or work hardening rate. FWHM measurement of both AM and AM_LSP has a similar profile on the surface and diverges along the depth, as shown in Figure 5. No cold work was found on the surface and it is possible that the dual side peening has encourage the dislocations to move deeper into the material that caused the increase in FWHM in the central region. There are other factors that needs to be considered and requires further investigation.

4. Conclusion

The suitability of LSP on AM IN718 was investigated in this study. Based on the initial analyses, AM IN718 has a higher content of δ_{211} precipitates due to the varying heat influx caused by its layer by layer deposition method. Employing LSP onto AM IN718 do not alter the phase distribution of the specimens. The compressive region of the AM_LSP sample went as deep as 625 μm from the surface and up to -471 MPa. Preliminary analyse of the FWHM data indicates that LSP imparted no cold work onto AM IN718 surface and further benchmarking exercise is needed.

References

1. Wen, Y., S. Xun, M. Haoye, S. Baichuan, C. Peng, L. Xuejian, Z. Kaihong, Y. Xuan, P. Jiang, and L. Shibi, *3D printed porous ceramic scaffolds for bone tissue engineering: a review*. *Biomater Sci*, 2017. **5**(9): p. 1690-1698.
2. Maconachie, T., M. Leary, B. Lozanovski, X. Zhang, M. Qian, O. Faruque, and M. Brandt, *SLM lattice structures: Properties, performance, applications and challenges*. *Materials & Design*, 2019. **183**: p. 108137.
3. Prasad, K., R. Sarkar, P. Ghosal, and V. Kumar, *Simultaneous creep-fatigue damage accumulation of forged turbine disc of IN 718 superalloy*. *Materials Science and Engineering: A*, 2013. **572**: p. 1-7.
4. Reed, R.C., *The Superalloys: Fundamentals and Applications*, ed. C.U. Press. 2006, Cambridge.
5. Sun, J. and H. Yuan, *Life assessment of multiaxial thermomechanical fatigue of a nickel-based superalloy Inconel 718*. *International Journal of Fatigue*, 2019. **120**: p. 228-240.
6. Mostafa, A., I. Picazo Rubio, V. Brailovski, M. Jahazi, and M. Medraj, *Structure, Texture and Phases in 3D Printed IN718 Alloy Subjected to Homogenization and HIP Treatments*. *Metals*, 2017. **7**(6).
7. Sangid, M.D., T.A. Book, D. Naragani, J. Rotella, P. Ravi, A. Finch, P. Kenesei, J.-S. Park, H. Sharma, J. Almer, and X. Xiao, *Role of heat treatment and build orientation in the microstructure sensitive deformation characteristics of IN718 produced via SLM additive manufacturing*. *Additive Manufacturing*, 2018. **22**: p. 479-496.
8. Strößner, J., M. Terock, and U. Glatzel, *Mechanical and Microstructural Investigation of Nickel-Based Superalloy IN718 Manufactured by Selective Laser Melting (SLM)*. *Advanced Engineering Materials*, 2015. **17**(8): p. 1099-1105.
9. Zhang, D., W. Niu, X. Cao, and Z. Liu, *Effect of standard heat treatment on the microstructure and mechanical properties of selective laser melting manufactured Inconel 718 superalloy*. *Materials Science and Engineering: A*, 2015. **644**: p. 32-40.
10. Tillmann, W., C. Schaak, J. Nellesen, M. Schaper, M.E. Aydinöz, and K.P. Hoyer, *Hot isostatic pressing of IN718 components manufactured by selective laser melting*. *Additive Manufacturing*, 2017. **13**: p. 93-102.
11. Peyre and Fabbro, *Laser shock processing : a review of the physics and applications*. *Optical and Quantum Electronics*, 1995. **27**.
12. Ballard, P., J. Fournier, R. Fabbro, and J. Frelat, *Residual Stresses Induced by Laser-Shocks*. *Le Journal de Physique IV*, 1991. **01**(C3): p. C3-487-C3-494.
13. Sundar, Ganesh, R.K. Gupta, Ragvendra, Pant, V. Kain, Ranganathan, R. Kaul, and Bindra, *Laser Shock Peening and its Applications: A Review*. *Lasers in Manufacturing and Materials Processing*, 2019. **6**(4): p. 424-463.
14. Kattoura, M., S.R. Mannava, D. Qian, and V.K. Vasudevan, *Effect of laser shock peening on elevated temperature residual stress, microstructure and fatigue behavior of ATI 718Plus alloy*. *International Journal of Fatigue*, 2017. **104**: p. 366-378.
15. Gill, A.S., Z. Zhou, U. Lienert, J. Almer, D.F. Lahrman, S.R. Mannava, D. Qian, and V.K. Vasudevan, *High spatial resolution, high energy synchrotron x-ray diffraction characterization of residual strains and stresses in laser shock peened Inconel 718SPF alloy*. *Journal of Applied Physics*, 2012. **111**(8).
16. Yong, C.K., G.D. West, G.J. Gibbons, and C.C. Wong. *Influence of Laser Shock Peening (LSP) on the Material Properties of Additive Manufactured IN718*. in *Advanced Surface Enhancement*. 2020. Singapore: Springer Singapore.
17. GmBH, E., *Material Data Sheet : EOS NickelAlloy IN718*. 2014.
18. International, B.S., *BS EN 3987:2009 Aerospace series — Test methods for metallic materials — Constant amplitude force-controlled high cycle fatigue testing*. 2009: UK.
19. Kraus, W. and G. Nolze, *POWDER CELL - A program for the representation and manipulation of crystal structures and calculation of the resulting X-ray powder patterns*. *Journal of Applied Crystallography*, 1996. **29**(3): p. 301-303.
20. Nunes, R.M., D. Pereira, T. Clarke, and T.K. Hirsch, *Delta Phase Characterization in Inconel 718 Alloys Through X-ray Diffraction*. *ISIJ International*, 2015. **55**(11): p. 2450-2454.

21. Drakopoulos, M., T. Connolley, C. Reinhard, R. Atwood, O. Magdysyuk, N. Vo, M. Hart, L. Connor, B. Humphreys, G. Howell, S. Davies, T. Hill, G. Wilkin, U. Pedersen, A. Foster, N. De Maio, M. Basham, F. Yuan, and K. Wanelik, *I12: the Joint Engineering, Environment and Processing (JEEP) beamline at Diamond Light Source*. *Journal of Synchrotron Radiation*, 2015. **22**(3): p. 828-838.
22. Stone, H.J., T.M. Holden, and R.C. Reed, *Determination of the plane specific elastic constants of waspaloy using neutron diffraction*. *Scripta Materialia*, 1999. **40**(3): p. 353-358.
23. *Stress Measurement, in Two-dimensional X-ray Diffraction*. 2018. p. 271-356.
24. Aba-Perea, P.E., T. Pirling, P.J. Withers, J. Kelleher, S. Kabra, and M. Preuss, *Determination of the high temperature elastic properties and diffraction elastic constants of Ni-base superalloys*. *Materials & Design*, 2016. **89**: p. 856-863.
25. Barros, R., F.J.G. Silva, R.M. Gouveia, A. Saboori, G. Marchese, S. Biamino, A. Salmi, and E. Atzeni, *Laser Powder Bed Fusion of Inconel 718: Residual Stress Analysis Before and After Heat Treatment*. *Metals*, 2019. **9**(12): p. 1290.
26. Hughes, D.J. and Z. Chen, *High resolution near-surface stress determination using synchrotron X-rays*. *Nuclear Instruments and Methods in Physics Research Section B: Beam Interactions with Materials and Atoms*, 2005. **238**(1): p. 214-218.
27. Ferreri, N.C., S.C. Vogel, and M. Knezevic, *Determining volume fractions of γ , γ' , γ'' , δ , and MC-carbide phases in Inconel 718 as a function of its processing history using an advanced neutron diffraction procedure*. *Materials Science and Engineering: A*, 2020. **781**: p. 139228.
28. Zhang, Y., L. Yang, T. Chen, W. Zhang, X. Huang, and J. Dai, *Investigation on the optimized heat treatment procedure for laser fabricated IN718 alloy*. *Optics & Laser Technology*, 2017. **97**: p. 172-179.
29. Anderson, M., A.L. Thielin, F. Bridier, P. Bocher, and J. Savoie, *δ Phase precipitation in Inconel 718 and associated mechanical properties*. *Materials Science and Engineering: A*, 2017. **679**: p. 48-55.
30. Mitra, J., S. Banerjee, R. Tewari, and G.K. Dey, *Fracture behavior of Alloy 625 with different precipitate microstructures*. *Materials Science and Engineering: A*, 2013. **574**: p. 86-93.
31. Shankar, V., K. Bhanu Sankara Rao, and S.L. Mannan, *Microstructure and mechanical properties of Inconel 625 superalloy*. *Journal of Nuclear Materials*, 2001. **288**(2): p. 222-232.
32. Wagner, L., *Mechanical surface treatments on titanium, aluminum and magnesium alloys*. *Materials Science and Engineering: A*, 1999. **263**(2): p. 210-216.